



# Study of elastic $\pi^- p$ scattering at COMPASS

Squared four-momentum transfer  $|t|$  and Regge theory

**Master Thesis**

by

Christian Dreisbach

Supervisor: Dr. Florian Haas

Primary Reviewer: Prof. Dr. Stephan Paul

Secondary Reviewer: Prof. Dr. Lothar Oberauer

Garching, 01.12.2014

I hereby declare that this thesis was formulated by myself and that no sources or tools other than those cited were used.

Garching, .....  
Date

.....  
Signature

1. Reviewer: Prof. Dr. Stephan Paul
2. Reviewer: Prof. Dr. Lothar Oberauer

# Contents

<b>I</b>	<b>Introduction</b>	<b>7</b>
<b>1</b>	<b>Physics Motivation</b>	<b>9</b>
<b>2</b>	<b>Production Mechanism</b>	<b>13</b>
2.1	Kinematics of Scattering Processes . . . . .	13
2.2	Mandelstam Variable $t$ . . . . .	14
2.3	Elastic Scattering at COMPASS . . . . .	14
2.4	The Scattering Amplitude . . . . .	17
2.4.1	Fraunhofer Diffraction . . . . .	17
2.4.2	Cross Section . . . . .	20
2.4.3	Scattering Amplitude in the Partial Wave Expansion . . . . .	21
2.5	Regge Theory and Pomeron Exchange . . . . .	22
2.6	Double Pomeron Exchange . . . . .	23
<b>II</b>	<b>Instrumentation</b>	<b>25</b>
<b>3</b>	<b>The COMPASS Experiment at CERN</b>	<b>27</b>
3.1	M2 Beamline . . . . .	27
3.2	Layout of the COMPASS Spectrometer . . . . .	27
3.2.1	Small-Area Tracking Detectors . . . . .	28
3.2.2	The Trigger System at COMPASS . . . . .	29
3.2.3	Data Acquisition and Reconstruction . . . . .	30
<b>4</b>	<b>The Recoil-Proton Detector</b>	<b>31</b>
4.1	Layout of the RPD . . . . .	31
4.2	The RPD as Trigger System . . . . .	32
4.3	Geometric Acceptance . . . . .	33
4.4	Energy Correction . . . . .	34
4.4.1	Present Energy Correction . . . . .	35
4.4.2	Improved Energy Correction . . . . .	35
4.5	Performance . . . . .	37
<b>III</b>	<b>Analysis</b>	<b>39</b>
<b>5</b>	<b>Kinematic Distributions</b>	<b>41</b>
5.1	Event Pre-selection . . . . .	41

5.2	Beam Properties . . . . .	41
5.3	Trigger Conditions and Recoil Particle . . . . .	43
5.4	Target and Primary Vertex Position . . . . .	44
5.5	Momenta and Angles . . . . .	45
5.6	Squared Four-Momentum Transfer $ t $ . . . . .	46
5.7	Overview of Runs and Cuts . . . . .	46
<b>6</b>	<b>Monte Carlo Simulation of COMPASS</b>	<b>49</b>
6.1	Monte Carlo Chain . . . . .	49
6.2	Event Generator for Elastic Scattering . . . . .	49
6.3	Problems in RPD Simulation . . . . .	51
<b>7</b>	<b>Acceptance and Resolution</b>	<b>53</b>
7.1	Acceptances . . . . .	53
7.1.1	Primary Vertex . . . . .	53
7.1.2	Squared Four-Momentum Transfer $ t $ . . . . .	55
7.2	Resolutions . . . . .	56
7.2.1	Primary Vertex . . . . .	56
7.2.2	Momenta of the Scattered Particle . . . . .	57
7.2.3	Squared Four-Momentum Transfer $ t $ . . . . .	59
<b>IV</b>	<b>Results</b>	<b>61</b>
<b>8</b>	<b>Theoretical Interpretation</b>	<b>63</b>
8.1	Exponential Fit Model . . . . .	63
8.1.1	Single Exponential Fit Model . . . . .	63
8.1.2	Double Exponential Fit Model . . . . .	65
8.1.3	Triple Exponential Fit Model . . . . .	67
8.2	Parametrization Based on the Quark Coupling . . . . .	68
8.3	Quadratic Term in Pomeron Trajectory . . . . .	71
8.4	Parametrization Based on Chou-Yang Model . . . . .	73
8.5	Discussion of Results . . . . .	75
<b>9</b>	<b>Summary and Outlook</b>	<b>77</b>
<b>A</b>	<b>Calculations</b>	<b>79</b>
A.1	Analytic Solution for the Beam Energy . . . . .	79
<b>B</b>	<b>Additional RPD Information</b>	<b>81</b>
B.1	Theoretical Prediction for Different Length of RPD Ring B Slabs . . . . .	81
B.2	Light Guide Influence on Squared Four-Momentum Transfer $ t $ . . . . .	82
B.3	Proton Energy Based on Passed Material Thickness . . . . .	83
B.4	Influence of Wrongly Identified Proton Tracks . . . . .	84
<b>C</b>	<b>Additional Analysis Informations</b>	<b>85</b>
C.1	Beam Gradient Projections . . . . .	85
C.2	Primary Vertex Projections . . . . .	85

<b>D Additional Information for the Conclusions</b>	<b>87</b>
D.1 Prediction with Nonacceptance Corrected Data . . . . .	87
<b>Bibliography</b>	<b>93</b>
<b>List of Figures</b>	<b>95</b>
<b>List of Tables</b>	<b>97</b>







## Abstract

The COMPASS experiment located at the SPS at CERN used a secondary negative pion beam in the year 2008 with an energy of 190 GeV/c to obtain a data set for pion-proton scattering. Although the measurement of elastic processes was not the primary objective, the extraction of a data set for elastic reactions with an unprecedented statistical precision was possible. In the first analysis of elastic pion-proton scattering at the fixed-target experiment COMPASS, the measurement of the Mandelstam variable  $t$  is used to compare the measured data with previous experiments and discuss several theoretical models for Pomeron exchange and Regge theory. The geometry of the operated recoil-proton detector, used for the selection of elastic-scattering events, limits the measurable range of  $t$  from 0.1 up to 4.5 GeV<sup>2</sup>/c<sup>2</sup>. Its usability is increased with the development of an improved method for the energy determination of the recoil proton. The presented selection principles lead to a clean data sample for the investigation of elastic scattering. The Monte Carlo simulation of the experiment is used to obtain the acceptance and resolution of the presented vertex and momenta distributions. Based on these studies the compatibility with previous experiments is examined and several theoretical models for the description of the  $t$ -distribution in the statistically significant range of 0.1 up to 3.0 GeV<sup>2</sup>/c<sup>2</sup> are compared.



## Zusammenfassung

Das COMPASS Experiment am CERN verwendete einen sekundären negativen Pionstrahl im Jahr 2008 mit einer Energie von  $190 \text{ GeV}/c$  um einen Datensatz für Pion-Proton-Streuung zu erhalten. Obwohl die Messung von elastischen Prozessen nicht das primäre Ziel war, konnte ein Datensatz für elastische Reaktionen mit einer beispiellosen statistischen Präzision extrahiert werden. In der ersten Analyse der elastischen Pion-Proton-Streuung am fixed-target Experiment COMPASS, wird die Messung der Mandelstamvariable  $t$  verwendet, um die erhaltenen Daten mit vorangegangenen Experimenten zu vergleichen und verschiedene theoretische Modelle für den Pomeron Austausch und die Regge Theorie zu diskutieren. Die Geometrie des verwendeten Rückstoss-Proton-Detektor, der für die Auswahl von elastischen Streueignissen verwendet wird, begrenzt den Messbereich von  $t$  auf  $0.1$  bis  $4.5 \text{ GeV}^2/c^2$ . Der Anwendungsbereich des Protonendetektors wurde mit der Entwicklung eines verbesserten Verfahrens für die Energiebestimmung der Rückstossprotons vergrößert. Die vorgestellten Auswahlkriterien der Ereignisse führen zu einem Datensatz, der zur Untersuchung von elastischer Streuung verwendet werden kann. Mit der Monte Carlo Simulation des Experiments wird die Akzeptanz und Auflösung der gemessenen Vertex- und Impulseverteilung bestimmt. Basierend auf diesen Studien kann die Kompatibilität zu vorangegangenen Messungen überprüft werden und der Vergleich von mehreren theoretischen Modellen zur Beschreibung der  $t$ -Verteilung in dem statistisch signifikanten Bereich von  $0.1$  bis  $3.0 \text{ GeV}^2/c^2$  ist möglich.



**Part I**

**Introduction**



# Chapter 1

## Physics Motivation

In particle physics the observation of scattering processes has always been an important experimental approach. With the measurements of the angular distribution of  $\alpha$ -particles scattering off gold atoms by Geiger and Marsden in 1910 [1], Ernest Rutherford accomplished his theory for the nuclear structure of the atom [2]. His observation supported the atomic model of Niels Bohr, published in 1913 [3], with its heavy positively-charged nucleus surrounded by light negatively-charged electrons. Rutherford's discovery in 1919 of hydrogen-like particles, emitted in collisions of  $\alpha$ -particles with nitrogen atoms, was a cornerstone in particle physics [4] and rose the question concerning the inner structure of the nucleus.

With the discovery of the neutron by James Chadwick in 1932 the mechanisms of nuclear binding and decay became primary problems [5]. Based on Chadwick's result, Enrico Fermi developed a theory for the  $\beta$ -decay in 1934 [6], which explicitly uses the neutrino postulated by Wolfgang Pauli in 1930 [7]. One year later Hideki Yukawa predicted the existing of a "U-field" by combining relativity and quantum theory in order to describe nuclear interactions by the exchange of a new particle between protons and neutrons. This new particle, today known as the pion, was discovered twelve years later in cosmic ray experiments performed by Cecil Powell [8]. It was the beginning of the meson exchange based theory for nuclear forces. With the inventions of particle accelerators in the following decades, more and more particles were discovered.

Due to the enormous variety of particles, also called "particle-zoo", a systematic ordering was necessary. Independently proposed by Gell-Mann and Zweig in 1964 [9, 10], and based on the experimental discoveries at the Stanford Linear Accelerator Center (SLAC) in 1968, the naive quark model allowed a systematic ordering of the growing number of hadrons.

The discoveries of the past century culminated in a theory, the *Standard Model*. It summarizes the quarks, leptons and the interactions. Since the 1970s, the Standard Model is a known concept and based on the set of fundamental particles and predictions for the quantized interactions are accessible via this theory.

With the Quantum Chromodynamic (QCD) as part of the Standard Model, a theory for the description of processes in hadronic interactions based on quarks and gluons as exchange particles was developed. However, QCD was not able to predict hadronic dynamics taking place, if the quark confinement dominates. Up to then, with the so-called

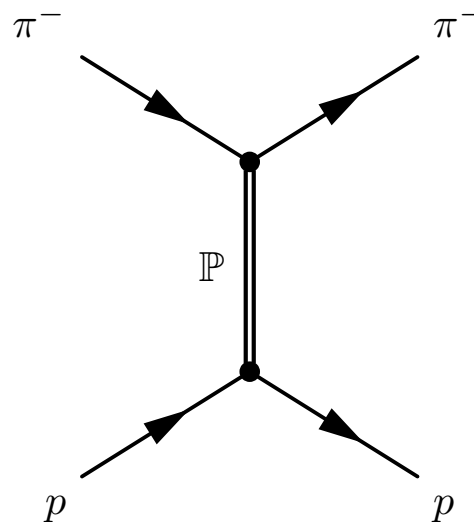


**Figure 1.1:** Single pomeron exchange in the elastic pion-proton scattering shown in the  $t$ -channel.

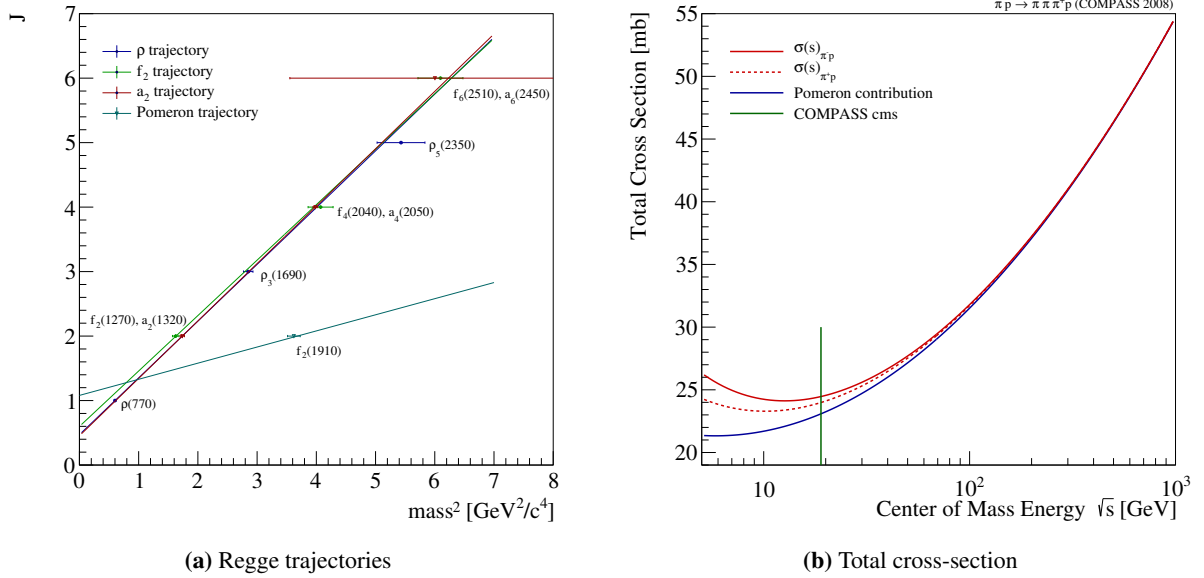


**Figure 1.2:** Different Regge trajectories and a possible Pomeron trajectory is depicted in (a). In (b) the total cross-section for different center-of-mass energies for the  $\pi^-p \rightarrow \pi^-\pi^-\pi^+p$  process is shown with the indicated COMPASS center-of-mass energy [11].

*Reggeons* as exchange particles in this regime by Tullio Regge [13] a non-relativistic description of hadronic scattering was possible. Later the extension to the relativistic case was established independently by Vladimir Gribov and Stanley Mandelstam.

The mathematical framework developed by Regge is based on the exchange of particle families instead of a single exchange particle in the scattering process. These families contain different particles with a respective spin  $J$ . They can be expressed by so-called *Regge trajectories* (Fig. 1.2a).

With Regge's theory an increasing total cross-section in scattering processes with growing center-of-mass energy could not be explained (Fig. 1.2b). The introduction of the so-called *Pomeron trajectory* different from the other Regge trajectories led to the solution of this problem. However, particles that correspond to the pomeron have not yet been discovered, but potential candidates are so-called *glueballs* [14].

The theory of Pomeron exchange is based on measurements of elastic scattering processes. The pion as a simply produced beam hadron is a suitable probe for hadronic interactions. Therefore, elastic pion-proton scattering processes can be used to review theories describing Pomeron interactions (Fig. 1.1).

The last experimental data for this process was taken in the late 1970s. Although description of the underlying physics is possible, an improved measurement of Mandelstam's variable  $t$  in this reaction would allow a review of Regge theory (Fig.1.3).

In 2008, the COMPASS experiment measured an unprecedented

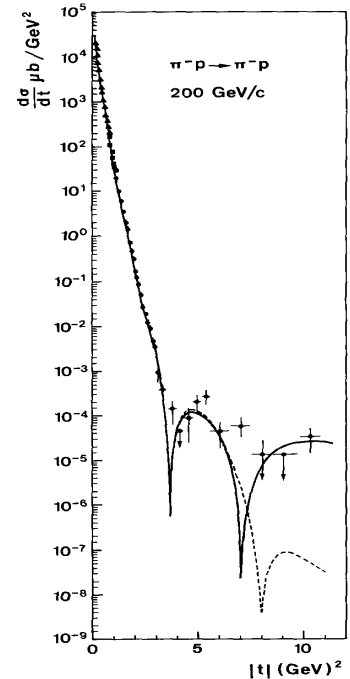


**Figure 1.3:** Elastic  $\pi^-p$  scattering at 200 GeV/c [12].

---

number of pion-proton reactions. Although COMPASS is a multi-purpose fixed-target experiment, which is mainly designed for hadron spectroscopy, also large sample of elastic pion-proton reactions was acquired.

Based on this data set the performance of the COMPASS spectrometer regarding the elastic process can be investigated. An sufficient acceptance and resolution is required to compare the obtained results with previous experimental data and examine the compatibility of different theoretical models for the Pomeron exchange.

Therefore, parametrization like in Donnachie et al. [14] can be revisited and today's theories [15] in Pomeron exchange can be further developed, resulting in a potentially increase of knowledge in Pomeron processes in scattering processes.



# Chapter 2

## Production Mechanism

Hadronic scattering experiments provide access to the underlying process of strong interaction. The simplest scattering reaction is the elastic one. By focusing on Mandelstam variable  $t$ , measured in elastic pion-proton scattering, statements regarding hadronic interactions based on Regge theory with Pomeron exchange are possible.

At first the basic kinematics of a general scattering processes is presented, followed by the discussion of elastic scattering at the fix-target experiment COMPASS. Starting with the measured quantities, the remaining kinematic variables are calculated.

The scattering amplitude for the case of Fraunhofer diffraction is introduced and based on the partial-wave expansion of the amplitude, the Regge theory and the Pomeron exchange are presented according to [14].

### 2.1 Kinematics of Scattering Processes

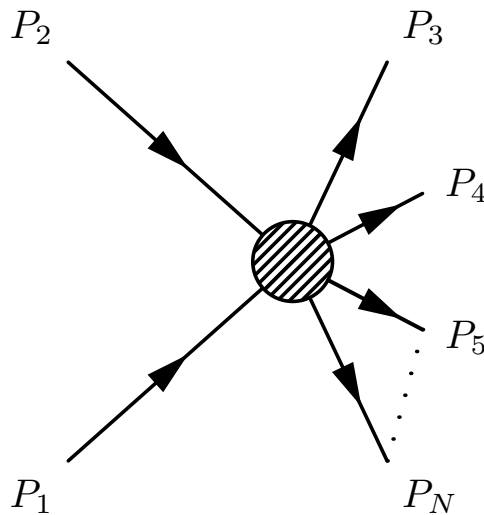


**Figure 2.1:** Example of a scattering process with  $N$  particles and the respective four-momentum vectors ( $P_i$ ).

The general scattering process is shown in Fig. 2.1. For  $N$  involved particles it can be written as

$$1 + 2 \rightarrow 3 + 4 + \dots + N \tag{2.1}$$

In this reaction the four-momenta are conserved, so that

$$P_1 + P_2 = P_3 + P_4 + \dots + P_N \quad \text{with} \quad P_i = (E_i, \vec{p}_i) \quad (2.2)$$

This includes the conservation of three-momenta and energy

The scattering process can be distinguished in at least two different kinds of measurements. A *single-particle inclusive measurement*

$$1 + 2 \rightarrow 3 + X \quad (2.3)$$

whereas  $X$  represents an unmeasured particle system. Or the *two-particle exclusive measurement*, with the measurement of all contributing particles.

$$1 + 2 \rightarrow 3 + 4 \quad (2.4)$$

The special case of

$$1 + 2 \rightarrow 1 + 2 \quad (2.5)$$

where two incoming particles are the same after the reaction, is the so-called *elastic scattering*. This process will be used for the investigation of hadronic interactions and will be discussed in more detail in Sec. 2.3.

## 2.2 Mandelstam Variable $t$

An important quantity in Regge theory and the Pomeron exchange is the Mandelstam variable  $t$ . The description of the processes in hadronic scattering is based on the exchange of particle families. They are parameterized by trajectories depending on  $t$ .

In a two body process  $t$  is defined as

$$t = (P_1 - P_3)^2 = (P_2 - P_4)^2 \quad (2.6)$$

It is also called *squared four-momentum transfer*. With this definition of the four-momentum transfer, it can be written as a function of the scattering angle  $\vartheta_3$ .

$$\begin{aligned} t &= m_1^2 + m_3^2 - 2(E_1 E_3 - \vec{p}_1 \cdot \vec{p}_3) \\ &= m_1^2 + m_3^2 - 2(E_1 E_3 - |\vec{p}_1| |\vec{p}_3| \cos \vartheta_3) \end{aligned} \quad (2.7)$$

## 2.3 Elastic Scattering at COMPASS

The advantage of the elastic scattering process is the complete knowledge of all variables within this reaction. However, in the experiment only the beam gradient, the vertex position and the three-vector of the momentum for the scattered particle is measured. The remaining quantities need to be calculated.

In the elastic process the type of the particles does not change; no resonances or additional particles are created. Compared to Fig. 2.1 the same incoming particles with four-momentum  $P_1$  and  $P_2$  are leaving the process with new four-momenta  $P_3$  and  $P_4$ . With the measurement of  $P_1$  and  $P_3$  or  $P_2$

and  $P_4$  the calculation of the squared four-momentum transfer  $t$  is possible. The best resolution in COMPASS is achieved by measuring the beam particle with  $P_1$  and the scattered particle with  $P_3$ .

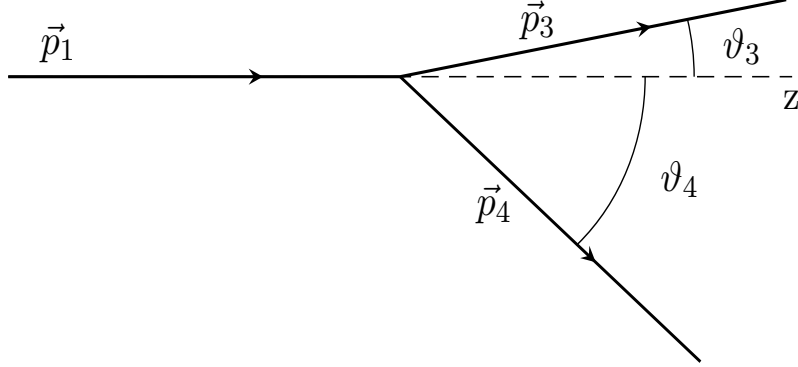


**Figure 2.2:** The three-momenta of the particles contributing to the  $1 + 2 \rightarrow 3 + 4$  scattering process in the fixed-target system.

In Fig. 2.2 the scattering process  $1 + 2 \rightarrow 3 + 4$  in the fixed-target case as it is present at the COMPASS experiment is shown. The three-momentum  $\vec{p}_1$  of the beam particle and the three-momenta  $\vec{p}_3$  and  $\vec{p}_4$  of the scattered and recoil particle are indicated. Their respective scattering angles  $\vartheta_3$  and  $\vartheta_4$  are depicted. The three-momentum  $\vec{p}_2$  of the target particle is equal to zero and therefore not drawn in Fig. 2.2.

The measured beam gradients  $\nabla_{x/y, 1}$  are defined as

$$\nabla_{x,1} = \frac{p_{x,1}}{p_{z,1}} \quad \text{and} \quad \nabla_{y,1} = \frac{p_{y,1}}{p_{z,1}} \quad (2.8)$$

In the elastic case at COMPASS, the masses of the beam and recoiling particle are the same after the scattering

$$m_1 = m_3 = m_\pi \quad \text{and} \quad m_2 = m_4 = m_p \quad (2.9)$$

One can calculate the unmeasured beam energy by rearranging the four-momentum transfer in Eq. (2.6).

$$t = (P_1 - P_3)^2 = (P_4 - P_2)^2 \quad (2.10)$$

$$m_1^2 + m_3^2 - 2(E_1 E_3 - |\vec{p}_1||\vec{p}_3|\cos\vartheta_3) = m_2^2 + m_4^2 - 2E_4 m_2 \quad (2.11)$$

For simplification of Eq. (2.11) the ultra-relativistic limits with  $E_i \approx |\vec{p}_i|$  is used. Additional substitution based on energy conservation is made:

$$E_4 = E_1 - E_3 + m_2 \quad (2.12)$$

A full formula without the ultra-relativistic limit approximation for the beam energy calculation can be found in Sec. A.1. The combination of Eq. (2.11) and (2.12) results is an equation for the beam energy.

$$\begin{aligned}
 E_1 &= \frac{m_4^2 - m_2^2 - m_3^2 - m_1^2 + 2E_3m_2}{-2[E_3(1 - \cos\vartheta_3) - m_2]} \\
 &\stackrel{(2.9)}{=} \frac{m_\pi - 2E_3m_p}{(E_3(1 - \cos\vartheta_3) - m_p)} \tag{2.13}
 \end{aligned}$$

For calculation of the scattering angle  $\vartheta_3$ , the azimuth angle  $\varphi_3$  and the energy  $E_3$  of the scattered particle, the measured momenta of the scattered particle are used.

$$\vartheta_3 = \text{acos}\left(\frac{p_{3,z}}{|p_3|}\right) \quad \varphi_3 = \text{atan}\left(\frac{p_{3,x}}{p_{3,y}}\right) \quad E_3 = \sqrt{m_3^2 + \vec{p}_3^2} \tag{2.14}$$

From Eq. (2.13) one can obtain the magnitude of the beam momentum. The resulting beam momenta in each projection can be obtained with the measured beam gradient.

$$|\vec{p}_1| = \sqrt{E_1^2 - m_1^2} \tag{2.15}$$

$$\vec{p}_1 = \begin{pmatrix} |p_1| \sin\nabla_{1,b} \\ |p_1| \sin\nabla_{1,y} \\ |p_1| - \sqrt{p_{1,x}^2 + p_{1,y}^2} \end{pmatrix} \tag{2.16}$$

With the calculated beam energy and momenta the Lorentz vector for the beam particle is fully described.

For the calculation of the recoil particle energy one first calculates the squared four-momentum transfer  $t$  via Eq. (2.6) with the Lorentz vectors of the beam and the scattered particle. The energy of the recoil particle can then be calculated from

$$t = (P_2 - P_4)^2 \tag{2.17}$$

$$= m_2^2 + m_4^2 - 2E_4m_2 \tag{2.18}$$

$$E_4 = \frac{m_2^2 + m_4^2 - t}{2m_2} \tag{2.19}$$

$$\stackrel{(2.9)}{=} \frac{2m_p^2 - t}{2m_p} \tag{2.20}$$

To calculate the remaining three-momentum vector of the recoiled particle one can use the momentum conservation.

$$\vec{p}_r = \vec{p}_b - \vec{p}_s \tag{2.21}$$

## 2.4 The Scattering Amplitude

In the following section the concept and the properties of the scattering amplitude are described. The amplitude is related to the underlying process and is used for describe of the process.

Starting with an analogy based on optical scattering, the scattering amplitude and the resulting cross section are introduced. With the transition into high-energy physics its importance for the Regge theory and the Pomeron exchange is discussed. The following discussion is based on [14, 16], where also further information can be found.

### 2.4.1 Fraunhofer Diffraction

The treatment of scattering processes originates back to the work of Joseph von Fraunhofer and Augustin-Jean Fresnel, whose names are nowadays used to label the two main regimes of diffraction. Gustav Kirchhoff presented a solution for the reconstruction of the diffraction picture. His theory serves as an introduction to the scattering amplitude. The used setup is shown in Fig. 2.3.

A plane wave with wave number  $k = 2\pi/\lambda$ , is incident on a screen with a hole of radius  $R$  and fulfills the short wavelength condition

$$kR \gg 1 \quad (2.22)$$

It is represented by a plane wave along the  $z$ -direction

$$\varphi(\vec{x}, t) = U(\vec{x}) e^{-i\omega t} \underset{\text{along } z}{=} U_0 e^{-ikz} \quad (2.23)$$

with the phase  $\omega = ck$  and a constant amplitude  $U_0$ , which satisfying Helmholtz equation

$$(\nabla^2 + k^2) U_0 = 0 \quad (2.24)$$

Each point of the plane wave serves as a center for new spherical waves, which sum results in the deflected wave. At a certain point behind the screen the image of this wave is collected, for example by a detector. Each point within the detector plane has a different distance and angle towards the new centers of the deflected wave, which results in constructive and destructive interference of the wave at each point in the plane. The amplitude of the deflected wave at a point  $\vec{x}$  can be mapped by the Fresnel-Kirchhoff formula

$$U(\vec{x}) = -\frac{ik}{4\pi} U_0 \int_{\text{hole}} d^2\vec{b} (1 + \cos\vartheta) \frac{e^{ik|\vec{r}'|}}{|\vec{r}'|} \quad (2.25)$$

where  $\vec{b}$  is the vector lying in the screen plane,  $|\vec{r}'|$  is the distance between the point in the detector plane and the center of a new spherical wave.

The vector  $\vec{r}$  connects the center of the new spherical wave within the hole and the point of wave deflected wave in the detection plane so that  $\vec{r} = \vec{b} + \vec{r}'$ .

The angle  $\vartheta$  between  $\vec{r}$  and the normal to the screen, allows the application of the short wavelength condition in Eq. (2.22). It simplifies the Eq. (2.25) due to the resulting small angle of the diffracted wave, which leads to  $\cos\vartheta \approx 1$  and, therefore,

$$U(\vec{x}) \approx -\frac{ik}{2\pi} U_0 \int_{\text{hole}} d^2\vec{b} \frac{e^{ik|\vec{r}'|}}{|\vec{r}'|} \quad (2.26)$$

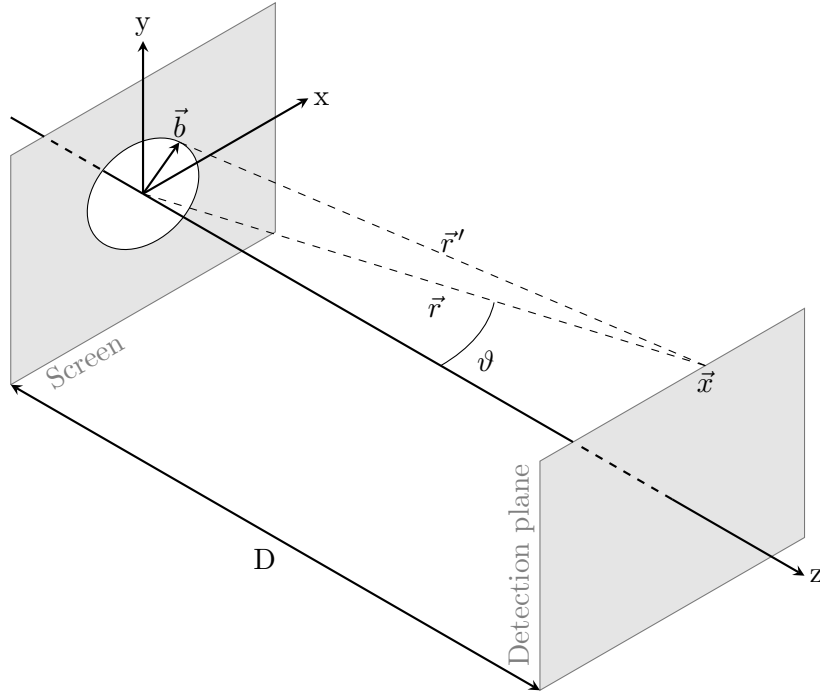


**Figure 2.3:** Diffraction of a plane wave by a hole in a screen mapped to a distant plane.

The integral of the wave amplitude in Eq. (2.26) can be further simplified by considering the large distance condition with respect to the extend  $R$  of the scattering center and the distance  $D$  between the screen and detection plane.

$$R/D \ll 1 \quad (2.27)$$

For high-energy scattering this condition can be assumed, which leads to the regime of Fraunhofer diffraction

$$kR^2/D \ll 1 \quad (2.28)$$

used in the description of hadronic scattering phenomena via optical concepts and allows a power series expansion of  $|\vec{b}'|/|\vec{r}'|$

$$k|\vec{r}'| = k|\vec{r} - \vec{b}| \quad (2.29)$$

$$\approx k|\vec{r}| - k \frac{\vec{r} \cdot \vec{b}}{|\vec{r}|} \quad (2.30)$$

Based on the proton radius of  $R_p \approx 1$  fm, a detector plane in a distance  $D \approx 1$  m and  $k \approx \sqrt{s} \approx 19$  GeV, which correspond the center-of-mass energy of COMPASS, one obtains a values for  $kR \approx 10^2$  and  $D/R \geq 10^{15}$  and therefore  $kR^2 \ll D$ . Thus the small-wavelength condition in Eq. (2.22) and the condition for Fraunhofer diffraction in Eq. (2.28) are fulfilled.

With  $|\vec{r}'| \approx |\vec{r}|$  in the denominator of the integral in Eq. (2.26) and the resulting transverse part of

$k\vec{r}/|\vec{r}|$  selected by the vector  $\vec{b}$ , one obtains

$$\frac{k}{r}\vec{r}_\perp = \left( \frac{kr_x}{r}, \frac{kr_y}{r}, 0 \right) =: \vec{q} \quad (2.31)$$

which simplifies Eq. (2.30)

$$k|\vec{r}| \approx k|\vec{r}| - \vec{q} \cdot \vec{r} \quad (2.32)$$

with the modulus of  $\vec{q}$  in the small angle approximation

$$|\vec{q}| = k \sin\vartheta \underset{\text{small } \vartheta}{\approx} k\vartheta \quad (2.33)$$

$\vec{q}$  describes the momentum transfer in this approximation as

$$\vec{q} \approx \vec{k}' - \vec{k} \quad \text{with} \quad |\vec{k}| = |\vec{k}'| = k \quad (2.34)$$

with  $\vec{k}$  and  $\vec{k}'$  as the respective incoming and outgoing wave vectors. The function for the amplitude of the scattered plane wave at point  $\vec{x}$  can now be written as

$$U(\vec{x}) = -\frac{ik}{2\pi} U_0 \frac{e^{ik|\vec{r}|}}{|\vec{r}|} \int_{\text{hole}} d^2\vec{b} e^{-i\vec{q}\cdot\vec{b}} \quad (2.35)$$

Introducing the so-called *profile function*  $\Gamma(\vec{b})$

$$\Gamma(\vec{b}) = \begin{cases} 1 & \text{in hole} \\ 0 & \text{outside hole} \end{cases} \quad (2.36)$$

allows it to rewrite the integral from Eq. (2.35), in order to integrate over the whole screen area, instead of only the hole.

$$U(\vec{x}) = -\frac{ik}{2\pi} U_0 \frac{e^{ik|\vec{r}|}}{|\vec{r}|} \int_{\text{screen}} d^2\vec{b} \Gamma(\vec{b}) e^{-i\vec{q}\cdot\vec{b}} \quad (2.37)$$

However, in high-energy scattering the diffraction is caused by an opaqueness of hadrons for hadrons. From Babinet's principle this can be described by a diffraction of an opaque disk, which corresponds to the previous hole depicted in Fig. 2.3 and subtracting the diffracted wave in Eq. (2.37) from the incoming plane wave in Eq. (2.23). This result is identical to a modification of the profile function  $\Gamma(\vec{b})$  in Eq. (2.37).

$$S(\vec{b}) = 1 - \Gamma(\vec{b}) \quad (2.38)$$

The newly obtained  $S(\vec{b})$  is the analogue to the so-called *S-matrix* in quantum mechanics, which describes the resulting amplitude by scattering off an obstacle.

$$u(\vec{x}) = -\frac{ik}{2\pi} U_0 \frac{e^{ik|\vec{r}|}}{|\vec{r}|} \int_{\text{screen}} d^2\vec{b} S(\vec{b}) e^{-i\vec{q}\cdot\vec{b}} \quad (2.39)$$

The  $S$ -matrix fulfills the normalization conditions, due to energy conservation, which implies

$$A |U_0|^2 = \int db^2 |u(\vec{x})|^2 \quad (2.40)$$

with  $A$  as the area of opening and leads to the constrain of  $S(\vec{b})$

$$\int db^2 |S(\vec{b})|^2 = A \quad (2.41)$$

Eq. (2.39) can be written as the sum of the incident and scattered wave

$$\begin{aligned} u(\vec{x}) &= u_{\text{inc}} + u_{\text{scatt}} \\ &= U_0 \left( e^{ikz} + f(\vec{q}) \frac{e^{ikr}}{r} \right) \end{aligned} \quad (2.42)$$

which introduces the scattering amplitude  $f(\vec{q})$  given by

$$f(\vec{q}) = \frac{ik}{2\pi} \int d^2\vec{b} \Gamma(\vec{b}) e^{-i\vec{q}\cdot\vec{b}} \quad (2.43)$$

and is simply the Fourier transform of the profile function

$$\Gamma(\vec{b}) = \frac{1}{2\pi ik} \int d^2\vec{q} f(\vec{q}) e^{i\vec{q}\cdot\vec{b}} \quad (2.44)$$

## 2.4.2 Cross Section

An important quantity is the *cross section* of a reaction. It is used to estimate the probability of a process. and can be calculated via the scattering amplitude.

Based on the intensity of the incident  $I_{\text{inc}}$  and scattered wave  $I_{\text{scatt}}$  given as

$$I_{\text{inc}} = |U_{\text{inc}}|^2 = |U_0|^2 \quad (2.45)$$

$$I_{\text{scatt}} = |U_{\text{scatt}}|^2 = |U_0|^2 \frac{|f(\vec{q})|^2}{r^2} \quad (2.46)$$

the differential cross-section  $d\sigma$  is defined as the ratio of the outgoing intensity in the solid angle  $d\Omega$  and the incident intensity

$$d\sigma = \frac{I_{\text{scatt}} r^2 d\Omega}{I_{\text{inc}}} \quad (2.47)$$

Using Eq. (2.45) and (2.46) the differential cross-section can be written as the modulus of the scattering amplitude

$$\frac{d\sigma}{d\Omega} = |f(\vec{q})|^2 \quad (2.48)$$

Therefore, the scattering cross-section is given by the integral over  $d\Omega$

$$\sigma_{\text{scatt}} = \int d\Omega \frac{d\sigma}{d\Omega} = \frac{1}{k^2} \int d^2\vec{q} |f(\vec{q})|^2 \quad (2.49)$$

Applying Parsval's theorem makes a transition from  $\vec{q}$  to  $\vec{b}$  possible. The cross section can now be written in terms of the  $S$ -matrix

$$\sigma_{\text{scatt}} = \int d^2\vec{b} |\Gamma(\vec{b})|^2 = \int d^2\vec{b} |1 - S(\vec{b})|^2 \quad (2.50)$$

Analog the absorption cross section  $\sigma_{\text{abs}}$  is defined as the ratio of the absorbed intensity and the incident intensity

$$\sigma_{\text{abs}} = \int d^2\vec{b} [1 - |S(\vec{b})|^2] = \int d^2\vec{b} [2\text{Re} \Gamma(\vec{b}) - |\Gamma(\vec{b})|^2] \quad (2.51)$$

Finally the total cross-section is obtained as the sum of the absorbed and scattered cross-section

$$\sigma_{\text{tot}} = \sigma_{\text{scatt}} + \sigma_{\text{abs}} = 2 \int d^2\vec{b} [1 - \text{Re} S(\vec{b})] = 2 \int d^2\vec{b} \text{Re} \Gamma(\vec{b}) \quad (2.52)$$

By combining the total cross section in Eq. (2.52) and the scattering amplitude, defined via the profile function  $\Gamma(\vec{b})$ , leads to the so-called *optical theorem*

$$\sigma_{\text{tot}} = \frac{4\pi}{k} \text{Im} f(\vartheta = 0) \quad (2.53)$$

which states that the total cross section is equal to the scattering amplitude in forward direction ( $\vartheta = 0$ ) and follows from the conservation of energy.

### 2.4.3 Scattering Amplitude in the Partial Wave Expansion

Typically scattering processes take place within a spherically symmetric potential and therefore the scattering amplitude does not depend on the azimuth angle  $\varphi$ , however, it depends, according to Eq. (2.33), on  $k$  and  $\vartheta$ . The amplitude can be expanded into a sum of partial waves

$$f(k, \vartheta) = \sum_{l=0}^{\infty} (2l+1) a_l(k) P_l(\cos\vartheta) \quad (2.54)$$

with the Legendre polynomial function  $P_l$  depending on the orbital angular momentum as the quantum number  $l$  and the partial-wave amplitudes  $a_l(k)$  given as

$$a_l(k) = \frac{e^{2i\delta_l(k)} - 1}{2ik} = \frac{S_l(k) - 1}{2ik} \quad (2.55)$$

containing the phase shift  $\delta_l(k)$  of the  $l$ -th wave. This is represented by an element  $S_l(k)$  of the  $S$ -matrix for a state of defined orbital angular momentum  $l$ . The dependence between the squared four-momentum transfer  $t$  and  $\cos\vartheta$  is given in the elastic pion-proton scattering case as

$$\cos\vartheta_t = \frac{t + 2(s - m_\pi^2 - m_p^2)}{\sqrt{t^2 - 4t(m_\pi^2 + m_p^2) + 16m_\pi^2 m_p^2}} \quad (2.56)$$

the scattering amplitude can be rewritten in terms of the Mandelstam variable  $s$  and  $\cos(\vartheta)$  as

$$f(k, \vartheta) \rightarrow A(s, t) = A(s, \cos\vartheta_t) = \sum_{l=0}^{\infty} (2l+1) a_l(t) P_l(\cos\vartheta_t) \quad (2.57)$$

and the properties for increasing center-of-mass energy  $s$  of the Legendre polynomial with Eq. (2.56) results in

$$P_l(\cos\vartheta_t) \underset{s \rightarrow \infty}{\sim} s^l \quad (2.58)$$

Thus the non-physical divergence of the partial-wave amplitude for large values of  $s$  in the scattering amplitude is given as

$$A(s, t) \underset{s \rightarrow \infty}{\sim} \sum_l a_l(t) s^l \quad (2.59)$$

## 2.5 Regge Theory and Pomeron Exchange

The divergence of the partial-wave amplitude in Eq. (2.59) at large values of  $s$  was the starting point for Tullio Regge to find a way of calculating the expansion for high energies. Based on Yukawa's introduction of the pion as exchange particle for the nuclear force, the scattering amplitude of a single meson with angular momentum  $l$  can be written as

$$A_{\text{meson}}(s, t) \sim a_l(t) P_l(\cos\vartheta_t) \quad (2.60)$$

In the elastic scattering case the amplitude of this process reduces to  $a_{\text{el}}(s, t = 0)$  leading to the imaginary part

$$\text{Im } a_{\text{el}}(s, t = 0) \underset{s \rightarrow \infty}{\sim} s^{2(l-1)} \quad (2.61)$$

and according to the optical theorem, the total cross-section is given by

$$\sigma_{\text{tot}} \underset{s \rightarrow \infty}{\sim} s^{2(l-1)} \quad (2.62)$$

and should exhibit the same behavior. This leads to a limitation of the total cross-section in the high-energy regime for mesons with a angular momentum  $l > 1$  and also violates the Froissart-Martin bound

$$\sigma_{\text{tot}} < \frac{\pi}{m_\pi^2} \ln^2(s) \quad \text{with} \quad s \rightarrow \infty \quad (2.63)$$

In the theory of Regge the described problem is solved by introducing bound states, sorted into families with an increasing angular momentum  $l$  for a spherical potential. These bound states are realized as poles of the partial-wave amplitude  $a_l(t)$  for a certain integer value of  $l$ . With the introduction of complex angular momentum, a smooth function  $a(l, t)$  is obtained, following the relation for  $l$

$$l = \alpha(t) \quad (2.64)$$

The function  $\alpha(t)$  is the so-called *Regge trajectory* with its poles named *Regge poles*. The contribution of each pole to the scattering amplitude is given by

$$A(s, t) \underset{s \rightarrow \infty}{\sim} s^{\alpha(t)} \quad (2.65)$$

Regge's concept describes the scattering process as an exchange of a whole family of resonances that belong to the same trajectory. The individual trajectories have a linear dependence on  $t$

$$\alpha(t) = \alpha(0) + \alpha' t \quad (2.66)$$

If  $\alpha(0) < 1$  the Froissart-Martin bound in Eq. (2.63) is respected. Further information about the underlying theory and ideas of Regge can be found in [14] and [16]. For a single Reggeon exchange the scattering amplitude  $A(s, t)$  can now be written within the Regge theory as

$$A(s, t) = \beta(t) \eta_\xi(t) s^{\alpha(t)} \quad (2.67)$$

with  $\beta(t)$  as the sum of residuals, their signature  $\xi$ , corresponding to positive or negative angular momentum  $l$ , which results in a general description for these two types.

$$\eta_\xi(t) = \begin{cases} -\frac{e^{-i\frac{\pi}{2}\alpha(t)}}{\sin\left(\frac{\pi}{2}\alpha(t)\right)}, & \text{for } \xi = +1 \\ -i\frac{e^{-i\frac{\pi}{2}\alpha(t)}}{\cos\left(\frac{\pi}{2}\alpha(t)\right)}, & \text{for } \xi = -1 \end{cases} \quad (2.68)$$

The total cross section for single Reggeon exchange follows from the optical theorem with Eq. (2.67).

$$\sigma_{\text{tot}} \sim \frac{1}{s} \text{Im} A(s, t=0) \sim s^{\alpha(0)-1} \quad (2.69)$$

Examples of trajectories are shown in Fig. 1.2a, where also a Pomeron and several Regge trajectories are depicted. The latter have an intercept at  $\alpha(0) \leq 0.6$ , which would result in a decreasing total cross-section according to Eq. (2.69). However, in experiments an increasing total cross-section is observed, which encourages the introduction of Gribov's new Regge trajectory, the so-called *Pomeron trajectory* with an interception  $\alpha(0) \geq 1$ .

In the theoretical approach in [14], which is based on fits to elastic scattering data, the Pomeron trajectory is parameterized by

$$\alpha(t) = 1 + \epsilon_\rho + \alpha'_\rho t \quad \text{with} \quad \alpha_0 = 1 + \epsilon_\rho \quad (2.70)$$

With  $\alpha'_\rho = 0.25/\text{GeV}^2$  and  $\epsilon_\rho \approx 0.06 - 0.08$  resulting from experimental data, to ensure the increasing total cross-section.

For the COMPASS experiment the overall Pomeron contribution to the scattering processes at the center-of-mass energy of  $\sqrt{s} = 19 \text{ GeV}$  is larger than 95%, which results in an opportunity to study Pomeron processes at COMPASS (Fig. 1.2b).

## 2.6 Double Pomeron Exchange

The general rise of the total cross-section for the elastic scattering processes cannot continue indefinitely. The elastic cross-section is not allowed to be larger than the total cross-section. An explanation for the rise of the cross-section is the exchange of two Pomerons. Also multiple exchanges can occur, if the energy is sufficiently high. The theoretical knowledge of double Pomeron exchange is insufficient and

therefore, a precise calculation is not possible. The expected behavior of the differential cross-section of the double Pomeron exchange are shown in Fig. 2.4. The double Pomeron exchange is shallower for increasing  $t$  compared to single Pomeron exchange, but it has a more rapid increase towards lower values of  $t$ .

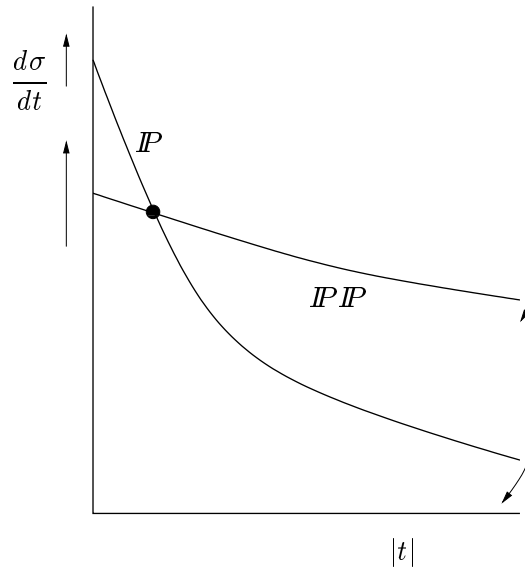


**Figure 2.4:** Single and double-Pomeron contributions to  $d\sigma/dt$ . The arrows indicate the change with increasing energy [17].

Both exchange processes need to be added in the scattering amplitude resulting in interference effects. The flattening of the  $t$ -distribution can also be observed in the measured COMPASS data.

**Part II**

**Instrumentation**



# Chapter 3

## The COMPASS Experiment at CERN

The Common Muon and Proton Apparatus for Structure and Spectroscopy (COMPASS) experiment situated at the Conseil Européen pour la Recherche Nucléaire (CERN) is a multi-purpose fixed-target experiment with a wide physics program. Its goal is a better understanding of the structure and dynamics of hadrons. Using hadron and muon beams with momenta between  $160 \text{ GeV}/c$  and  $200 \text{ GeV}/c$  the domain of non-perturbative QCD is accessible. The large, two-stage magnetic spectrometer serves as a tool for precision spectroscopy of light mesons and baryons. In the years 2008 and 2009 positive and negative hadron beams and different targets were used. With the data taken in 2008, using a pion beam impinging on a liquid-hydrogen target, the investigation of pion-proton processes is possible. Although the study of elastic scattering events was not the primary objective, the extraction of an data set with elastic scattering events was successful.

### 3.1 M2 Beamline

The Super Proton Synchrotron (SPS) provides protons with momenta of  $400 \text{ GeV}/c$ , which are guided to the primary production target T6. A beryllium target is used to generate either secondary hadron beams with an intensity up to  $8 \times 10^6 \text{ s}^{-1}$ , or tertiary electron beams with the additional use of a lead target. For Particle Identification (PID) CEDAR<sup>1</sup> detectors are installed 30 m in front of the COMPASS target and provide a high rate PID for beam particles with momenta up to  $300 \text{ GeV}/c$ . The fractions of particle types at the production target and at the COMPASS target are listed in Tab. 3.1.

**Table 3.1:** Main components of the negative hadron beam provided by the M2 beam line. The fraction of each component changes due to particle decay from the production target T6 to the COMPASS target [18].

Particle	Fraction at T6 target	Fraction at COMPASS target
$\pi^-$	0.947	0.968
$K^-$	0.046	0.024
$\bar{p}$	0.007	0.008

### 3.2 Layout of the COMPASS Spectrometer

The COMPASS experiment is situated on the north area of CERN. A sketch of the COMPASS experiment and its detectors can be found in Fig. 3.1. To access the full range of momenta, the COMPASS

<sup>1</sup> Čerenkov Differential counter with a chromatic Ring focus

experiment is separated into two parts. The magnets (SM1) and (SM2) divide the spectrometer in a section for particles up to 20 GeV/c and a part detecting particles at higher momenta. Each part is equipped with an electromagnetic calorimeter (ECAL) and a hadronic calorimeter (HCAL) for electromagnetic and hadronic particle detection, besides the several types of tracking detectors.

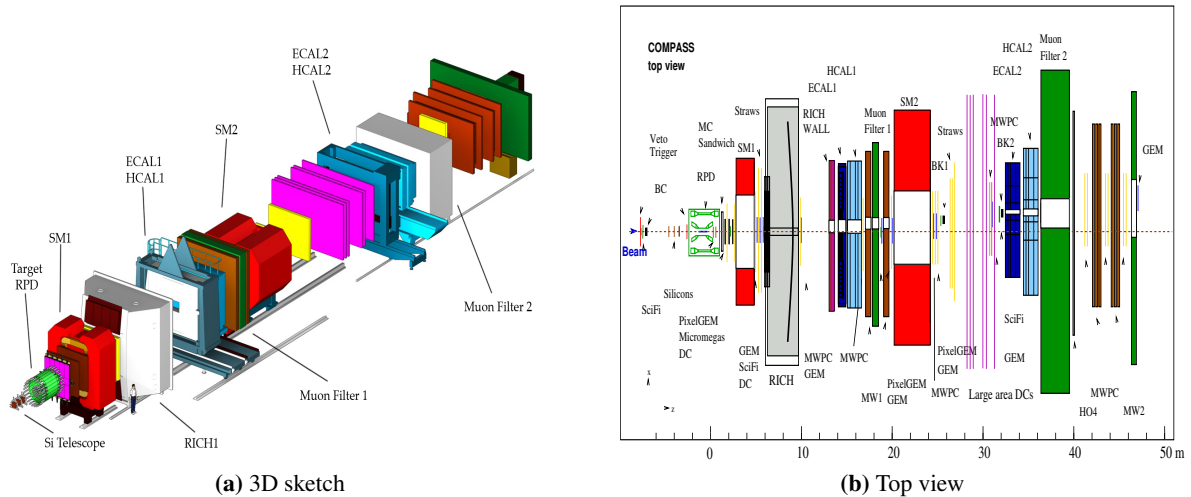


**Figure 3.1:** COMPASS setup of 2008 for measurements with hadronic beams. The beam enters from the left side. The different detector types are indicated in different colors. In (a) the layout of the COMPASS experiment is illustrated and its two-stage spectrometer separated by the two magnets spectrometer magnet 1 (SM1) and SM2 (SM2). In (b) the top-view of the setup is shown. The single detector planes are visible [18].

In front of the target a scintillating fiber detector and silicon detectors are installed for measuring the beam gradient and position. During the 2008 data taking the target was filled with liquid hydrogen. For the detection of the recoiling proton from the target a detector consisting of two scintillating rings surrounding the target is used. This is the so-called *Recoil-Proton Detector (RPD)* and further discussed in the following chapter. A sketch of the target region can be found in Fig. 3.2. In the first stage of the spectrometer a Ring Imaging Čerenkov (RICH) detector is used for PID, which is limited to maximal momenta of 2.5 GeV pions, 9 GeV kaons and 17 GeV protons. In order to measure elastic scattering only the tracking detectors are necessary, especially those, which are responsible for the detection of particles with a small scattering angle.

### 3.2.1 Small-Area Tracking Detectors

In the case of elastic scattering only a small deflection of the scattered beam particle occurs, the track is reconstructed using detectors for detection of particles with small angles. In COMPASS different kinds of tracking detectors with different sizes, resolutions and rate capabilities are used, depending on their position and the resulting requirement.

Close to the beam axis the particle rate is highest. Therefore, Micropattern Gaseous Detectors (MPGD), like MicroMegas and Gas Electron Multiplier (GEM) are used, which are capable of those high requirements in rate and resolution. Directly in the beam region with extreme particle rates around  $10^5 \text{ mm}^{-2} \text{ s}^{-1}$ , scintillating fibers and GEMs with a pixel readout, so-called *PixelGEM* detectors, are installed. Silicon detectors are placed around the target for accurate tracking and vertexing.

In case of elastic scattering the resolution of the kinematic variables is limited by the single outgoing particle track. For the vertex reconstruction two silicon detector stations are situated behind the target.

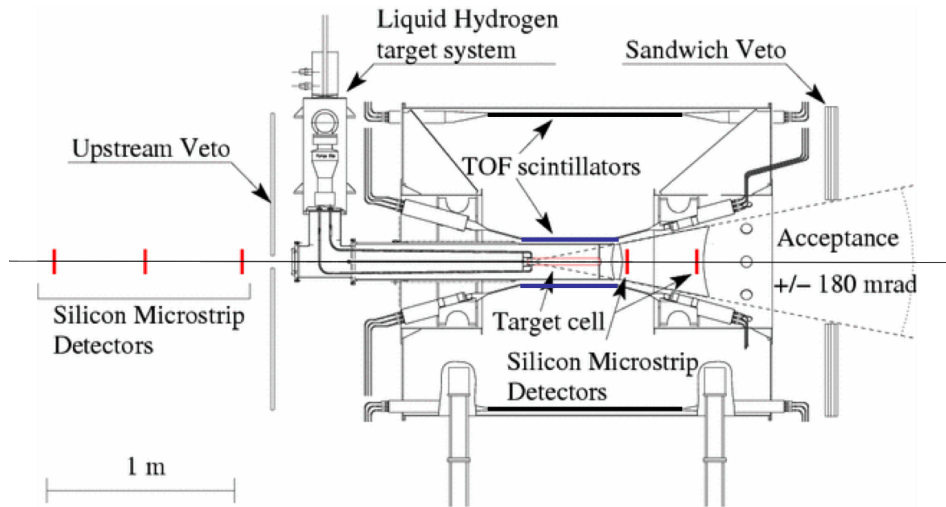


**Figure 3.2:** Side view of the target region of COMPASS for the 2008 layout. The beam enters from the left side and is measured by three silicon microstrip detector stations. A target cell with the liquid-hydrogen target inside is surrounded by Time-Of-Flight (TOF) scintillators, which are part of the RPD. Two silicon microstrip detector stations are used for the vertex detection. A veto system surrounding the target is used to filter events, which do not originate from the reaction within the target cell [18].

Each consisting of four silicon detectors. Since 2008 three PixelGEM detector stations are used as small area tracking detectors. Each consisting of two single PixelGEM detectors. Additionally, twelve MicroMegas in three stations with four detectors each are situated between the target region and the SM1.

### 3.2.2 The Trigger System at COMPASS

The selection of events is performed by a trigger. The main trigger system for the physics program in 2008 is the Diffractive Trigger (DT0). A schematic drawing is shown in Fig. 3.3.

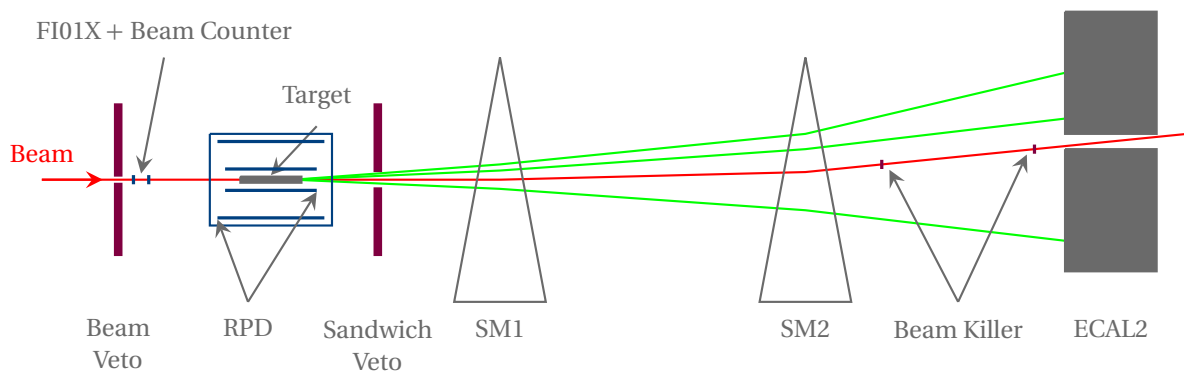


**Figure 3.3:** Sketch of the DT0 system. The beam incident from the left side. It is first detected by a scintillating fiber (FI01X) and a scintillation disk used as a beam counter. A signal in both RPD rings caused by a recoil proton originating from the target region is required. Events outside the spectrometer acceptance are rejected by the sandwich veto after the target. Non-interacting beam particles are supposed to be detected by two beam killer stations down stream of SM2 [11, 18].

The DT0 trigger consists of three parts. The first part of the DT0 requires a coincident signal in the scintillating fiber (FI01X) and the beam counter. The latter is a scintillating disc, tagging single beam particles. The second part requires a signal in both rings of the RPD, which can be assumed to be a proton track, its details are described in Sec. 4.2. Events outside the spectrometer acceptance and non-interacting beam particles are vetoed.

### 3.2.3 Data Acquisition and Reconstruction

The COMPASS experiment requires a Data Acquisition System (DAQ) capable of recording high event rates with up to  $5 \cdot 10^7$  particles per 10 s SPS spill resulting in a trigger rate of 30 kHz.

The reconstruction software is called COMPASS Reconstruction and Analysis (CORAL). It is used for track reconstruction, vertexing and to process detector information. CORAL is also used for Monte Carlo data reconstruction, which is further discussed in Sec. 6. Its output is based on ROOT trees [19] and stored in Mini Data Summary Tree (mDST) files. For event pre-selection the Physics Analysis Software Tools (PHAST) is used.

# Chapter 4

## The Recoil-Proton Detector

One part of the DT0 trigger system as mentioned in Sec. 3.2.2 is the RPD. This apparatus was designed based on the detector for slow proton detection of the GAMS NA12/2 experiment at CERN [20]. The aim of the RPD is the detection of protons recoiling from the liquid-hydrogen target and to create a trigger signal. It is a main part in the selection of elastic scattering events. A scheme of the RPD geometry can be found in Fig. 4.1. It is built up from an inner and an outer ring of scintillating slabs surrounding the target. Photomultiplier Tubes (PMTs) are used to detect the signal from the slabs. The selection principles for a proton track are time-of-flight, measurement of the energy loss in the single slabs via scintillating light output and the requirement of a signal in the inner and geometrically corresponding outer ring slabs. Limited by multiple scattering in the target itself and the surrounding materials, the lowest detectable proton momentum is  $270 \text{ MeV}/c$ , which correspond to a squared four-momentum transfer  $|t|$  of  $0.07 \text{ GeV}^2/c^2$  [18].

A correct energy estimation of the recoil proton can be obtained by taking into account the different energy loss in the materials and is deeper discussed in Sec. 4.4. The upper limit of detectable recoil proton momenta is given by the geometrical acceptance, which is further described in Sec. 4.3. During the data taking campaign in 2008 and most parts of 2009, the RPD was used as the main trigger component.

### 4.1 Layout of the RPD

The RPD as shown in Fig. 4.1 consists of two cylindrical scintillator rings A and B, radially surrounding the liquid-hydrogen target cell at a distance of 20 and 76 cm and have a thickness of 0.5 and 1 cm respectively.

These scintillator rings are angular segmented into single slabs. Ring A consists of 12 slabs, with a length of 50 cm each and the 24 slabs of ring B have a length of  $115 \text{ cm}^1$ . PMTs are used on both ends of each slab. Light guides are used as connecting of the slabs of ring B and the PMTs. They are molded of the same active scintillator material as the ring B slabs. This fact has an influence on the event selection and acceptance correction, which is later discussed in Sec. 5.3.

The signal of each PMT is sent to an analog-to-digital converter (ADC) and a time-to-digital converter (TDC). For data reconstruction it is further detected by constant-friction discriminators (CFDs) and forwarded to the field-programmable gate array (FPGA) based trigger system [18].

---

<sup>1</sup> The length of the slabs of ring B is problematic. In the Monte Carlo simulation it is given as 106 cm. In the publication of the COMPASS collaboration [18] and in different technical drawings the length is 115 cm. An investigation of the real data could result in the assumption of a length of 106 cm, due to the rough visible structure of the light guides. In the further analysis a length of 106 cm is used to be in agreement with the Monte Carlo simulation and the results from the real data. Further discussion can be found in Sec. 6.3.

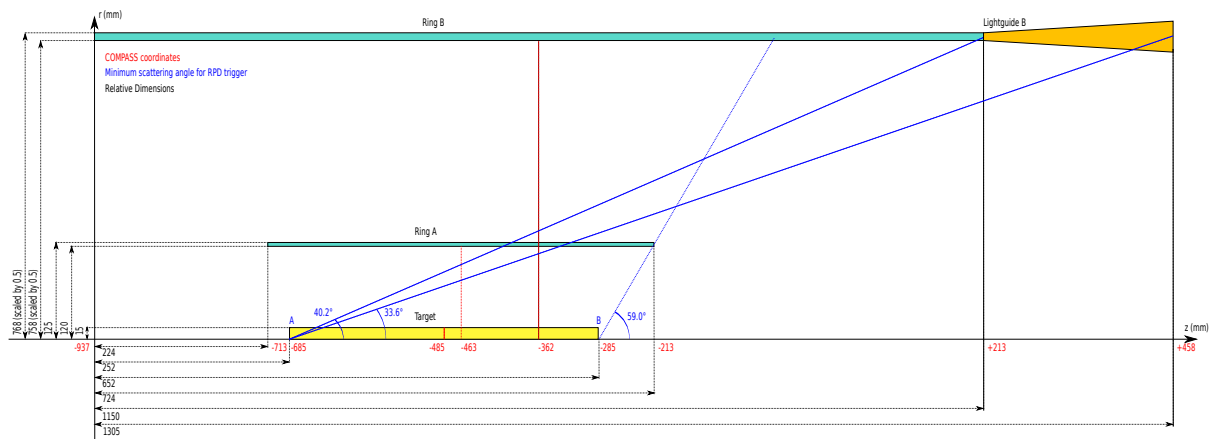


**Figure 4.1:** Radial symmetric RPD sketch with the two cylindrical scintillator rings A and B. Ring A is  $\varphi$ -segmented in 12 parts, ring B is  $\varphi$ -segmented in 24 parts. Both rings surround the liquid-hydrogen target. The scintillators are read out by Photomultiplier Tubes (PMT) at both ends. The light guide for ring B is molded from the same scintillator material as the slab and is active material. Additional to the general dimensions written in black, the COMPASS coordinates in (mm) are given in red. The minimum scattering angles required to trigger an event are drawn in blue. The dimensions are based on the values given in [18].

## 4.2 The RPD as Trigger System

In COMPASS the RPD is used as a trigger system to select recoiling protons from the target. Fig. 4.2 shows the correlation between the energy loss in ring A and ring B in comparison with the prediction.

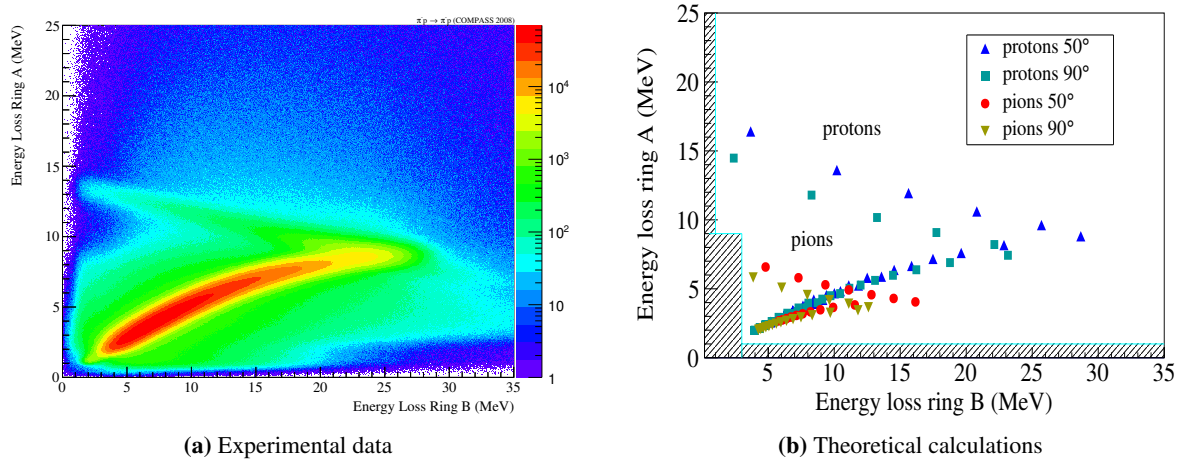


**Figure 4.2:** RPD energy loss correlation between ring A and ring B of the recoiled proton. A theoretical prediction is shown in (a) and the measured data is visible in (b).

The thicker slabs in ring B leading to a higher energy deposition of the recoil proton. As a result a distinction between protons and pions is possible. This energy loss correlation between the inner and outer ring is used for the trigger logic. The shaded area indicates the hardware threshold for the trigger logic. This threshold is not visible in the experimental data as shown in Fig. 4.2a. It could be caused by resolution effects of the converting of the analog PMT signal into digital signals. The trigger system of

the RPD requires a signal in one inner ring slab followed by a signal in one of the three possible outer ring slabs. The trigger scheme is shown in Fig. 4.3a.

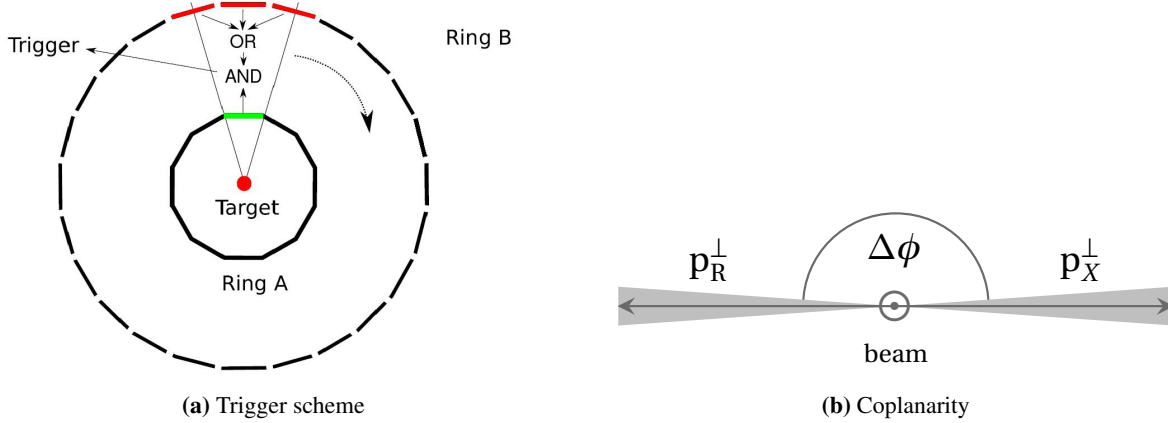


**Figure 4.3:** The RPD trigger scheme with the two cylindrical scintillator rings A and B is shown in (a) [18]. An allowed combination for inner and outer ring slab is shown. One inner ring slab and one of the possible three outer ring slabs must be hit to trigger an event. Additionally the momentum conservation in the Center-of-Mass System (CMS) between the recoiled and scattered particle is required as shown in (b) [11].

In Fig. 4.3b the so-called *coplanarity* requirement between the scattered and recoiled particle is shown. This back-to-back scattering is for event select and further described in Sec. 5.3.

### 4.3 Geometric Acceptance

The single slabs of each ring become distinguishable in the RPD hitmaps shown in Fig. 4.4. These hitmaps are generated from the calculated  $\varphi$ -angle and the predicted hit position of the recoil proton in each ring evaluated from the measurement of the scattered particle by the spectrometer via Eq. (5.1).

The superposition of the boundary layers of each slabs in ring A and B causes slices in the ring B hitmap as shown in Fig. 4.4b. Noticeable are the laser connectors of each slab visible in Fig. 4.4a as a slightly smeared out spot in the middle of each slab. This ineffective areas also cause a dip in the primary vertex  $z$  distribution shown in Fig. 5.5b.

The boundary layers for each of the twelve slabs are ineffective. This is visible in Fig. 4.4a as horizontal lines in the  $\varphi$ -projection, the sliced distribution in the ring B hitmap is caused by the requirement of a hit in both RPD rings. The forward momentum of the recoiling proton causes a hit at larger  $z$ -position in both rings compared to the primary vertex position. The geometrical acceptance of the RPD limits the scattering angle of the recoil proton to a range where both rings can be hit. Furthermore, the required angle depends on the  $z$ -position in the target region.

Based on the geometry of the RPD the minimal scattering angle of the recoiling proton being within the acceptance is calculable and therefore the maximal momentum transfer  $|t|$ , which can be detected by the RPD. The minimum scattering angle, which is required for a hit in ring A or ring B in dependence of the  $z$ -position in the liquid-hydrogen target can be calculated via Eq. (4.1) and Eq. (4.2) respectively.

$$\vartheta_{\text{recoil, min, A}} = \tan^{-1} \left( \frac{r_A}{z_A - z} \right) \quad (4.1)$$

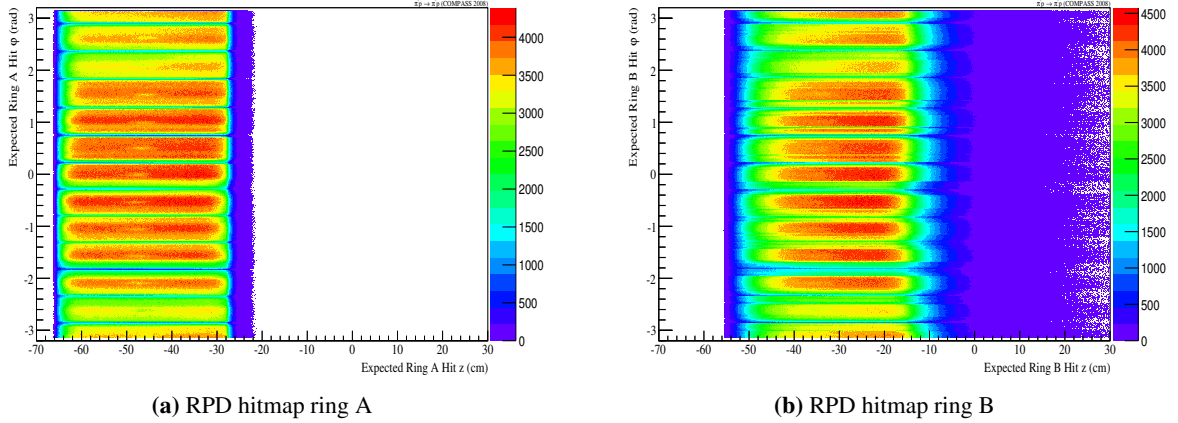


**Figure 4.4:** The calculated hitmaps of the RPD for ring A and ring B are shown. Based on the scattered particle measured by the spectrometer, the expected hit in the RPD  $\varphi$ -projection in dependence of the expected  $z$ -position in the RPD slab is calculated via Eq. (5.1).

$$\vartheta_{\text{recoil,min, B}} = \tan^{-1} \left( \frac{r_B}{z_B - z} \right) \quad (4.2)$$

With  $r_{A,B}$  as the radius of either ring A or ring B,  $z_{A,B}$  as the most downstream sensitive  $z$ -position of the RPD slabs and  $z$  as the position in the target. The theoretical values for the minimal scattering angle of the recoiling proton and therefore the maximal momentum-transfer  $|t|$  accepted by the RPD can be found in Fig. 4.5a. The calculation is based on the dimensions given in Fig. 4.1 except for the length of the slabs of ring B, which is assumed as 106 cm, as it is set in the Monte Carlo simulation and also in agreement with the measured data. Further information about the length of the ring B slabs can be found in Sec. 6.3. A prediction for the geometrical acceptance of the RPD with a ring B slab length of 115 cm is shown in Fig. B.1.

The blue and the red band indicate the minimal scattering angle and the maximal  $|t|$ -value to trigger an event. The width of the bands correspond to the radial extend of the liquid-hydrogen target. The theoretical prediction is in agreement with the data shown in Fig. 4.5b. A cut to remove events triggered by a recoil proton in the light guides for the slabs of ring B is required, because an evaluation of those RPD signals is unreliable. This influence and further information about the active light guides can be found in Sec. B.2.

The detector geometry of the RPD limits the maximal measurable momentum transfer  $|t|$  up to  $|t| < 4.5 \text{ GeV}^2/c^2$ , which also can only be measured in the most upstream position of the target, thus leads to a limitation in number of events for high recoil momenta.

## 4.4 Energy Correction

The RPD allows to measure the velocity of the recoil proton by time-of-flight and the traveled distance between ring A and ring B from the proton scattering angle. While traversing materials along its path, the proton loses energy. To estimate the initial value of the energy of the proton a correction of the energy is necessary. The reconstructed path of the recoil proton allows to calculate the energy loss in the traversed materials. Currently an energy correction based on tabulated values of the energy loss with

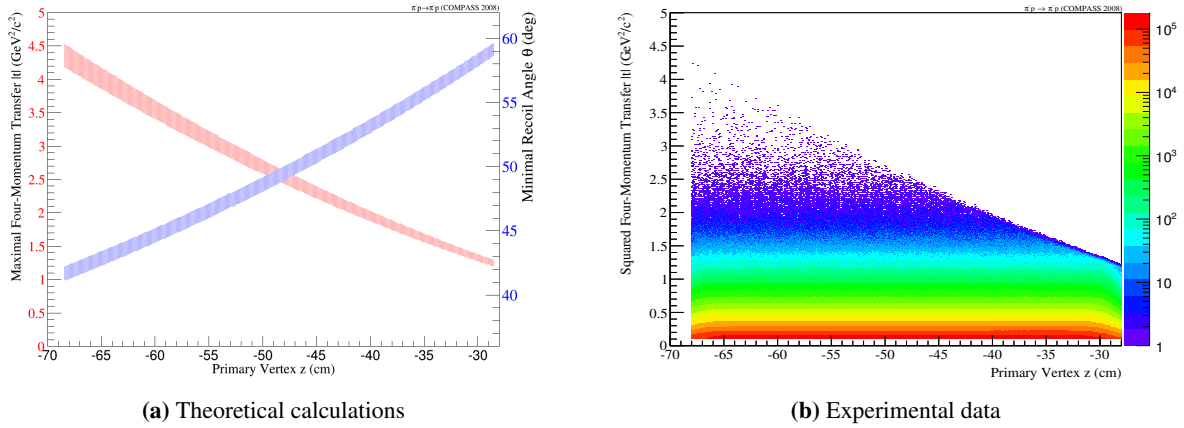


**Figure 4.5:** The theoretical values for the acceptance limit of the RPD based on the geometry of the RPD are shown in (a). The blue band indicates the minimal scattering angle of the recoiled proton to trigger an event in dependence of the primary vertex  $z$ -position with its width corresponding to the radial extend of the liquid-hydrogen target. In red the calculated four-momentum transfer  $|t|$  is shown. The theoretical hypothesis is in agreement with the real data shown in (b).

an interpolation between those values is used in the RPD reconstruction, this method causes problems in the energy correction. An improved correction for the proton energy is presented.

#### 4.4.1 Present Energy Correction

For the RPD an energy correction, based on tabulated values between a kinetic energy from 4 up to 600 MeV of the recoil proton. A quadratic interpolation between those values is used. This leads to artifacts in the corrected energy. A comparison between the directly measured RPD energy of the recoil proton and the present correction is shown in Fig. 4.6a.

In the present correction bumps are visible, which are caused by the quadratic interpolation. A bump at an energy of 1.11 GeV is caused by missing values for the energy loss in the materials for kinetic energies of the recoil proton higher than 0.6 GeV. This effect is also visible in Fig. 4.7a as a hard cut off in the effect of the energy correction.

#### 4.4.2 Improved Energy Correction

In Fig. 4.8 the range of protons in the materials used in the RPD are shown [21]. The values are obtained from the National Institute of Standards and Technology (NIST). Based on values of the NIST the range of protons in the used materials of the RPD can be calculated.

The energy correction is based on a spline<sup>2</sup> fit of the range values. This spline fit is evaluated to estimate the proton path. This results in a function describing the range in the materials based in the kinetic energy. The inverse is used for the calculation of the energy loss based on the passed material thickness. It is shown in Fig. B.3. A comparison between the uncorrected RPD energy and the improved correction can be found in Fig. 4.6b. The energy loss increases with lower proton momentum and therefore the effect of the correction is larger compared to higher proton momenta. It is nearly constant

<sup>2</sup> “A spline is any smooth function that is piecewise polynomial but also smooth where the polynomial pieces connect.” [22]

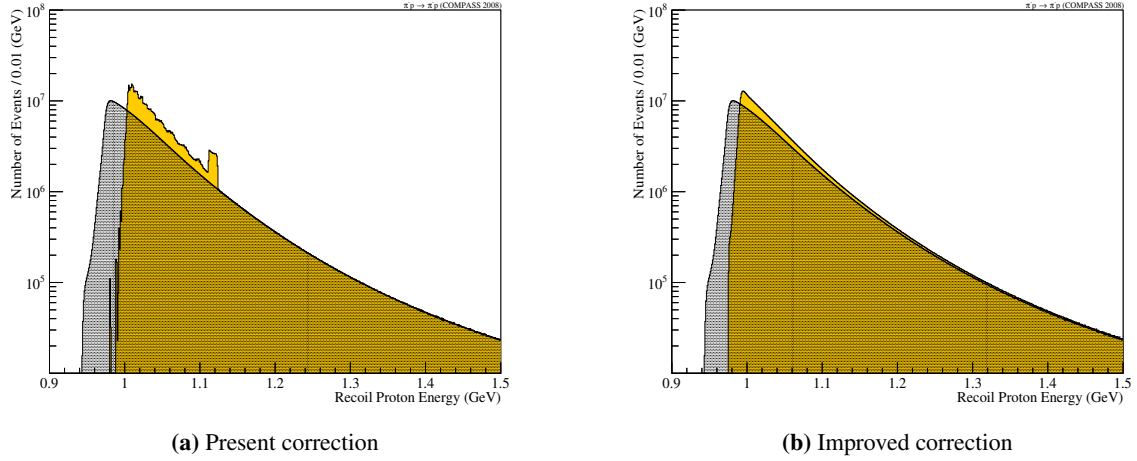


**Figure 4.6:** Comparison between the uncorrected RPD energy of the recoil proton measured by the RPD, drawn as shaded region, and the different types of energy correction in yellow. In (a) the comparison between the uncorrected and the present energy correction is shown. The comparison between the improved energy correction and the directly measured energy by the RPD is shown in (b).

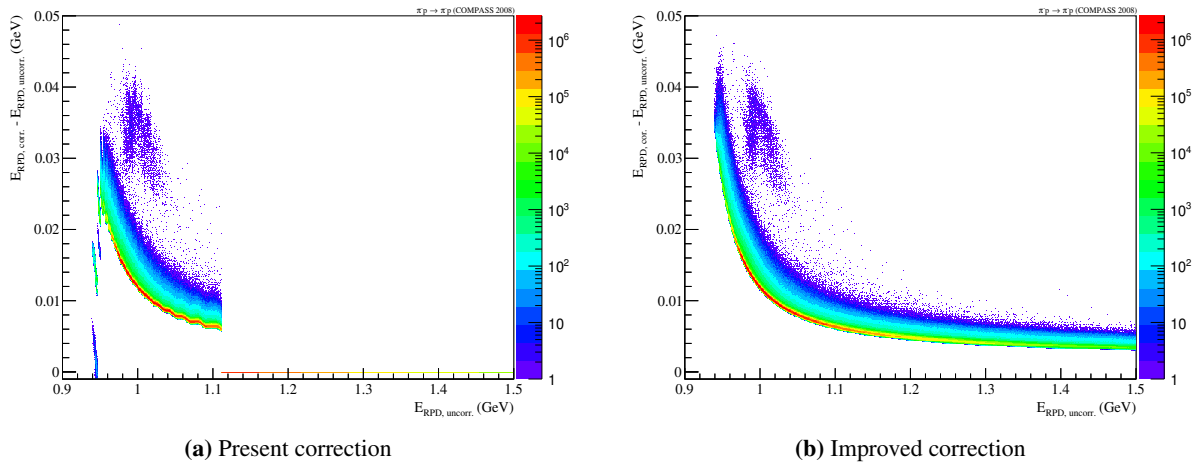


**Figure 4.7:** The effect of the present energy correction in dependence of the uncorrected proton energy measured by the RPD is shown in (a). Artifacts like bumps due to the quadratic interpolation and the end of the correction which is caused by the end of the tabulated values for the correction are visible. For lower kinetic energies some strange correction behaviors occur. For the improved energy correction in (b) none of the previous artifacts are visible. The separated region above the main slope of the correction is caused by wrongly identified tracks by the corresponding reconstruction software.

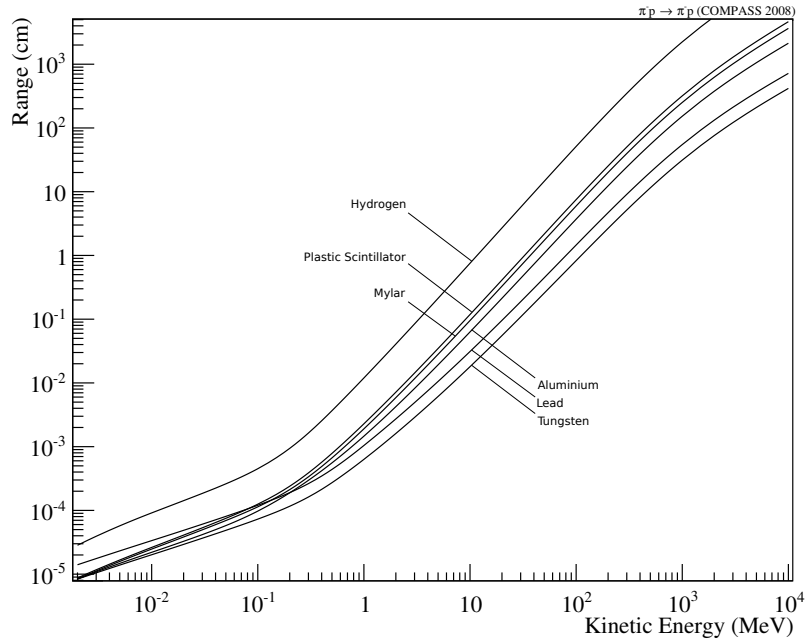


**Figure 4.8:** Proton range distribution for the used materials in the RPD. The values are based on the NIST tables [21]. For the energy correction a spline<sup>2</sup> fit is used to evaluate the energy loss or the range of protons in each material.

for proton momenta larger than 1.1 GeV. In Fig. 4.7b the effect of the improved correction is shown. The separated region above the main region is caused by wrongly identified tracks of the RPD software. A comparison with and without a cut on the number of recoil tracks present can be found in Fig. B.4 and Fig. B.5. The fraction of events in the separate region is strongly reduced by this cut.

## 4.5 Performance

The corrected energy of the RPD recoil proton is in rough agreement with the calculated energy of the recoil proton calculated via the measured kinematics by the spectrometer. The relative resolution of the recoil proton energy measured by the RPD is shown in Fig. 4.9a. It is decreasing with larger proton energy. This dependence is also visible in Fig. 4.10. The difference of the calculated proton energy based on the measured kinematics by the spectrometer increases as a function of the recoil proton energy.

Additionally, an offset between both energies is noticeable. The linear increasing mean value of the energy resolution for the RPD shown in Fig. 4.9b indicates a wrong calibration of the RPD. This limits the field of application of the RPD regarding energy measurements.

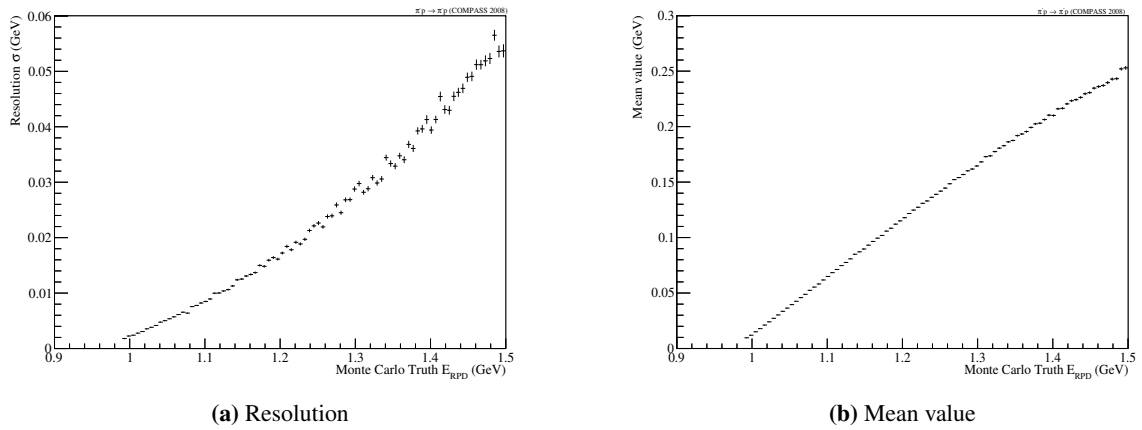


**Figure 4.9:** Performance of the measurement for the recoil proton energy. In (a) the relative resolution of the recoil proton energy measured by the RPD is shown. The mean value of the RPD energy is shown in (b).

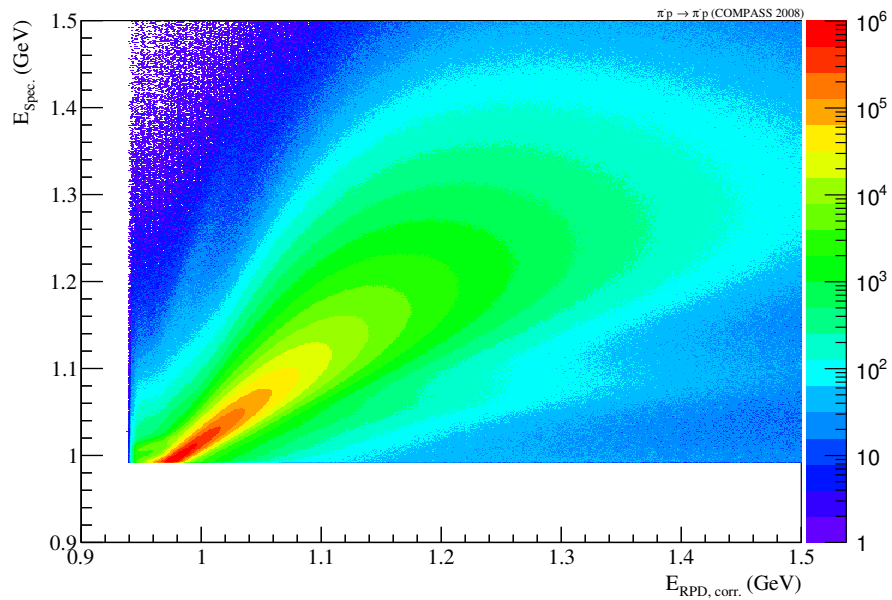


**Figure 4.10:** Comparison between the calculated energy of the recoil proton based on the measured kinematics by the spectrometer.

**Part III**

**Analysis**



# Chapter 5

## Kinematic Distributions

In this chapter the event selection of the required data set for the elastic scattering process is discussed. A large amount of pion-proton reactions was recorded in 2008. The obtained data set by extraction of elastic scattering events serves as a good basis for an accurate investigations of the elastic process. It is studied with respect to the squared four-momentum transfer  $|t|$  to obtain a  $|t|$ -distribution, which can be used to compare the results with previous experiments. Additionally, an access to the underlying exchange process described by Regge theory is possible. As first work based on the elastic scattering process at COMPASS a brief discussion of the basic kinematic variables is done.

Starting with the description of the pre-selection for the required events, an in-depth discussion of the applied cuts required to select a clean data sample with the required properties for a sound investigation follows. Additionally, the kinematic properties of the selected events are presented.

### 5.1 Event Pre-selection

The first basic selection of events takes place at PHAST level. For elastic scattering only events with one primary vertex are selected to ensure a single reaction.

This primary vertex should be located in a wide range from  $z = -2$  m to  $z = 2$  m around the target to avoid reactions outside the target and secondary interactions. The track of the outgoing particle needs to pass at least one magnet to measure momentum and charge. Additionally, its charge should correspond to the charge of the beam. The effect of each cut is displayed in Fig. 5.1. The pre-selection cuts reduce the 7 billion recorded events in 2008 to 500 million resulting in a sound starting sample. All additional selections are performed in further analysis steps and are discussed in the following.

### 5.2 Beam Properties

For the COMPASS experiment a so-called *debunched beam* is used, so that ideally there should only be a single beam particle for an event. To avoid pile-up events, the difference between the time stamp of this particle and the global event time is used. In Fig. 5.2a this so-called *beam time* is shown. The used cut for the beam time of  $-2 \text{ ns} \leq t_b \leq 2 \text{ ns}$  is indicated. It is well center around zero. The pile-up events causing bumps around the main peak are neglected.

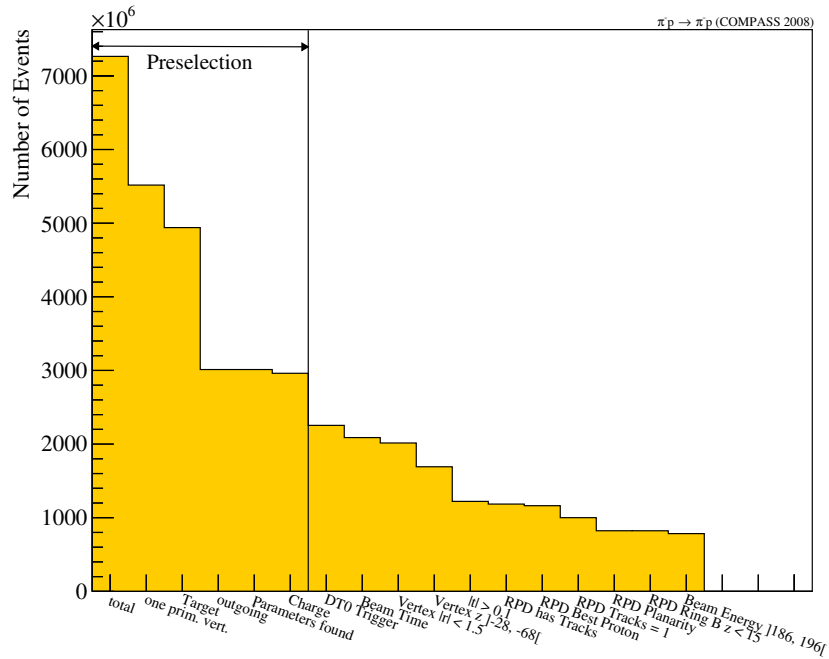
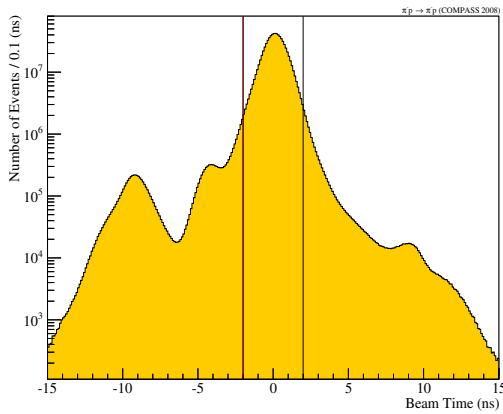
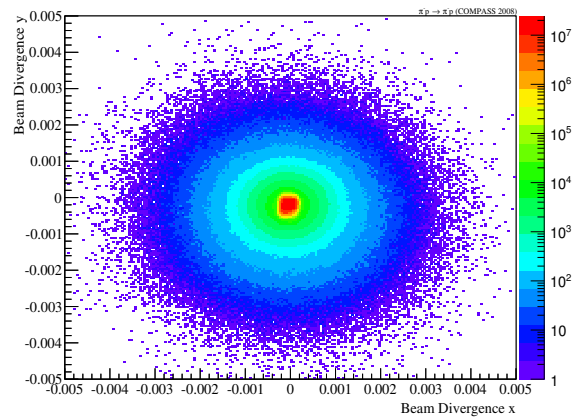


**Figure 5.1:** Overview of the used cuts to obtain a clean data sample of the elastic scattering events. The preselection cuts on PHAST level are situated on the left side of the black line. In the further analysis more refined cuts are applied and are listed on the right side of the black line.



(a) Beam time



(b) Beam divergency

**Figure 5.2:** The beam time is shown in (a). The applied cut on the beam time is indicated by black lines. In (b) the beam divergency is depicted. The beam is well focused after all cuts applied. The projections in  $x$ - and  $y$ -directions can be found in Fig. C.1.

The beam divergency after all applied cuts is shown in Fig. 5.2b. The beam is well focused. In Fig. C.1 the individual  $x$ - and  $y$ -projections are shown. In the experiment the beam energy cannot be directly measured. Only the beam gradient in  $x$ - and  $y$ -projection is measured by the beam telescope. To calculate the beam energy via the kinematics of the scattered particle Eq. (2.13) is used. The background

in the calculated beam energy, mainly caused by radiative energy losses of the charged beam particle, is primarily reduced by the RPD coplanarity cut. It is further discussed in the following section. For cleaning the data sample a cut on the beam energy to be between  $186 \text{ GeV}/c \leq E_b \leq 196 \text{ GeV}/c$  is used. This cut is indicated in Fig. 5.3b.

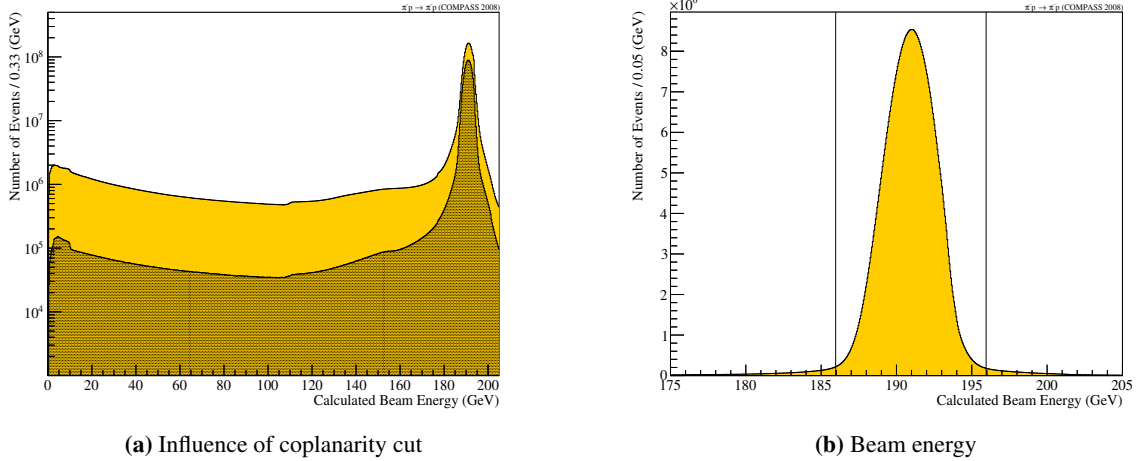


**Figure 5.3:** In (a) the influence of the RPD coplanarity cut on the calculated beam energy is shown. The region indicated in yellow is the data only with preselection cuts. Mainly influenced by the applied RPD coplanarity cut the data sample drawn as shaded region becomes more clear. In (b) the calculated beam energy with all cuts except the exclusivity cut is shown. The vertical lines indicate the used exclusivity cut on the beam energy.

### 5.3 Trigger Conditions and Recoil Particle

To select a clean data sample it is important to ensure the events originate from the liquid-hydrogen target and a recoil proton is present. During the data taking the DT0 trigger (Sec. 3.2.2) is used for this purpose. The information of the RPD is used during the selection in the DT0 trigger. A valid signal by the RPD has to fulfill several requirements.

First the RPD reconstruction should find the track of a recoil proton. This track should have meaningful values for the three-momentum vector of the proton and should originate from the target region. For elastic scattering events only one recoil proton from the target is allowed. An important quantity is the azimuthal angle  $\varphi$  between the scattered pion and the recoil proton. Due to momentum conservation, this angle should be  $180^\circ$ . This fact is called *coplanarity* and illustrated in Fig. 4.3b. The geometric angular resolution, caused by the individual RPD slabs influences the coplanarity. If one of the inner slabs  $A_n$  is hit, the hit in the outer ring has to be in slabs  $B_{2n-1}$ ,  $B_{2n}$ , or  $B_{2n+1}$ . For a hit in the middle slab the resolution attains a value  $7.5^\circ$  [11]. In the other two cases the resolution can be better. The resolution is taken into account when considering the angular difference between the proton direction measured by the RPD and the predicted proton three-vector, based on the kinematics of the pion [23].

$$\vec{p}_{pp} = \vec{p}_{beam} - \vec{p}_{scat} \quad (5.1)$$

After the requirement of the coplanarity, the efficiency of the different regions become visible in the RPD hitmaps shown in Fig. 4.4.

The events with a large enough squared four-momentum transfer  $|t|$ , corresponding to a sufficiently

large scattering angle  $\vartheta$  of the recoil proton, end up in the active light guides of ring B of the RPD. The bent form and varying thickness of the scintillator material used for the light guide results in a complex description compared to the otherwise flat scintillator slabs. The acceptance correction as described in Sec. 7 is challenging due to an insufficient description of the light guide within the Monte Carlo simulation. Therefore, events are removed if the extrapolated track of the recoil proton hits the ring B light guide at a  $z$ -position  $z_{\text{RPD}} \geq 15$  cm. This cut is indicated in Fig. 5.4.

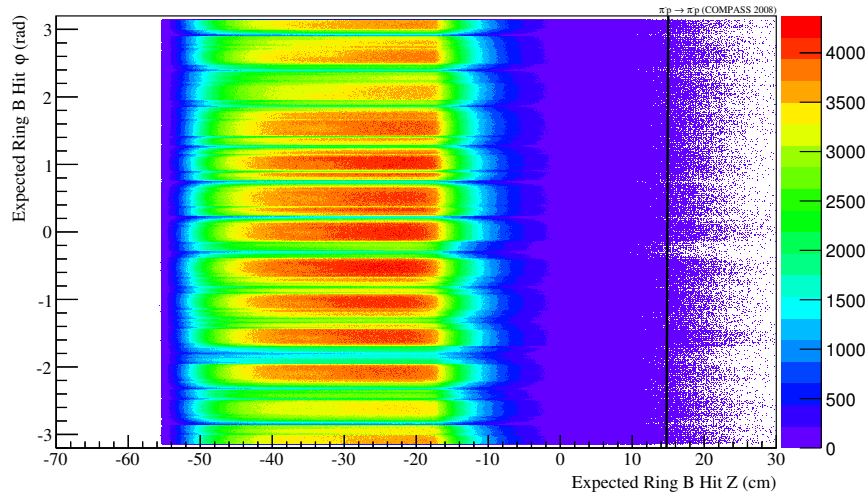


**Figure 5.4:** Calculated hit map of ring B of the RPD with the expected hits. The cut used to avoid the problematic zone of the light guide for  $z \geq 15$  cm for the ring B slabs consisting of active scintillator material is indicated as black line.

## 5.4 Target and Primary Vertex Position

The liquid-hydrogen target is situated in a  $z$ -range between  $z = -68$  cm and  $z = -28$  cm. Elastic scattering events have to originate from this area. In Fig. 5.5b the primary vertex distribution along the  $z$ -axis is depicted with indicated cuts. Noticeable are the two different slopes in the vertex distribution, which are caused by the superposition of the acceptance for the vertex reconstruction by the spectrometer and the RPD as trigger. Due to the laser connectors used for the RPD scintillator calibration visible in Fig. 4.4a in the middle of each slab, a dip is generated by the acceptance of the RPD. In the radial vertex distribution the fill level of the liquid-hydrogen target is visible at the upper side of the distribution, as well as the holding structures for the target cell.

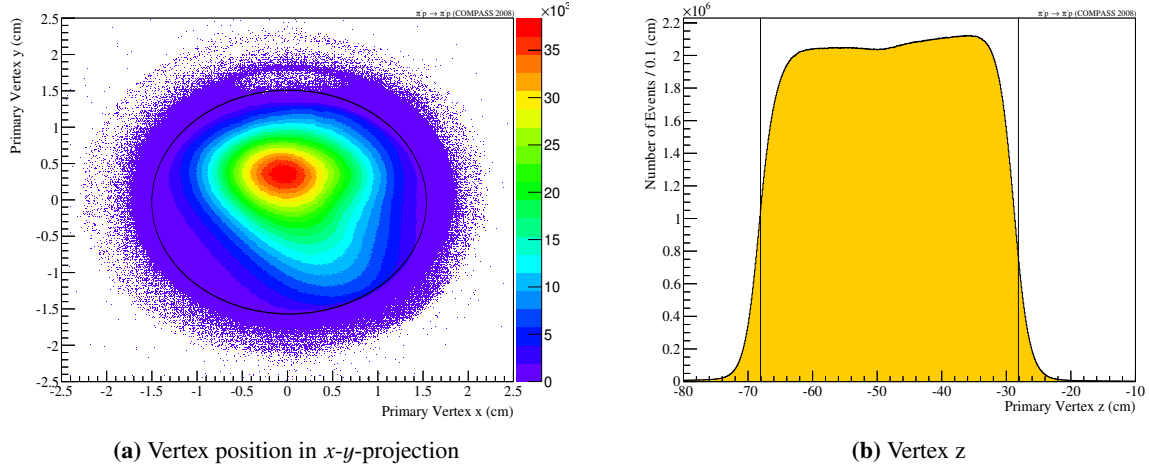


**Figure 5.5:** The vertex projection in  $x$ - $y$ -projection and  $z$ -direction with all cuts applied, except the ones indicated.

## 5.5 Momenta and Angles

In the presentation of the momenta and angles of the scattered pion the respective kinematic variables are discussed within the laboratory system. The momentum of the scattered pion is measured by the spectrometer. The influence of the RPD trigger requirement described in Sec. 4.2 is visible as segmented parts in the  $x$ - $y$ -projection of the scattered pion momentum. As the  $x$ - and  $y$ -components are small, the difference between the  $z$ -component of the scattered pion momentum and the beam momentum is also small.

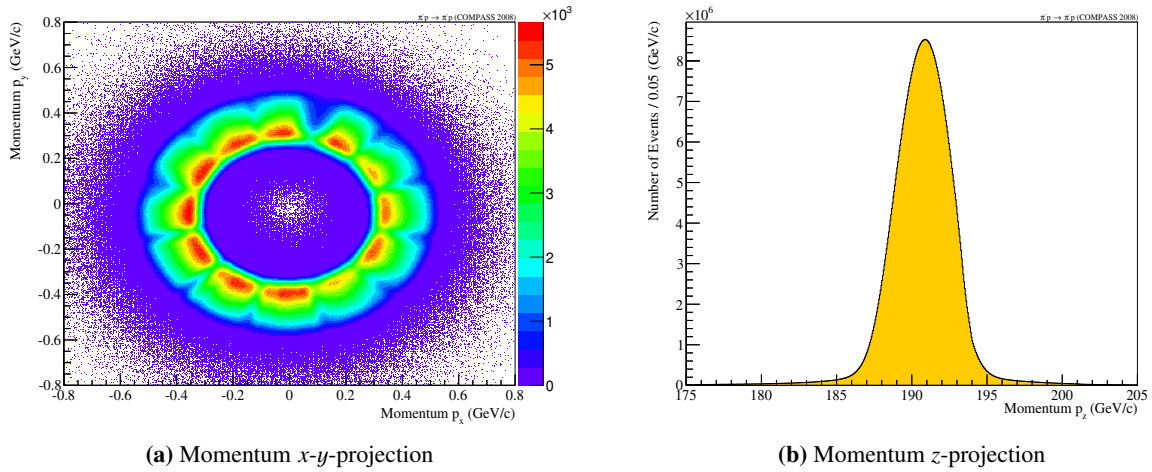


**Figure 5.6:** Momenta of the scattered pion for  $x$ - $y$ - and  $z$ -projection of the momenta in the laboratory system. In (a) the influence of the RPD trigger requirement is visible. The  $z$ -momentum of the scattered pion is only slightly decrease compared to the incoming beam momentum in  $z$ -direction (b).

Based on the measured momenta of the scattered pion, the scattering angle  $\theta$  and the azimuthal angle  $\varphi$  can be calculated via Eqs. (2.14). These scattering angles are shown in Fig. 5.7.

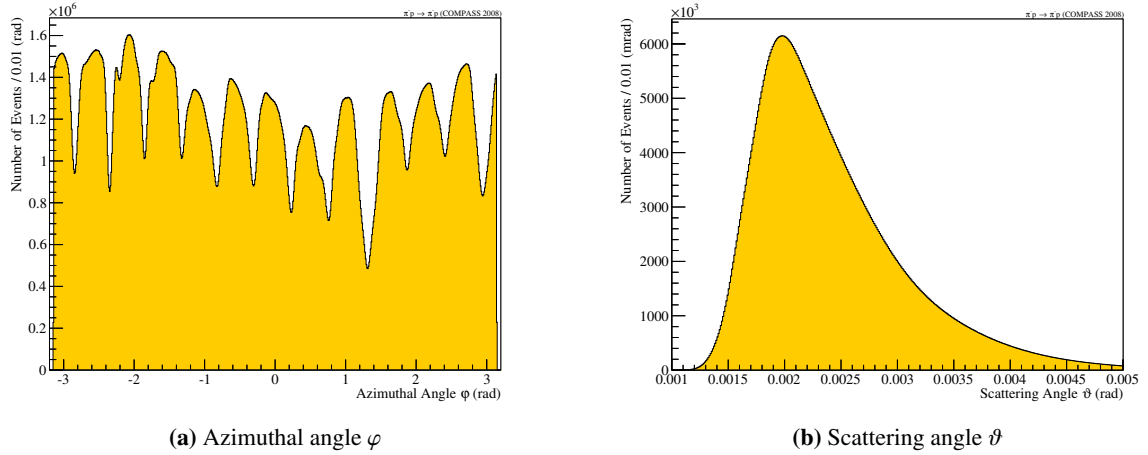


**Figure 5.7:** Scattering angles  $\varphi$  and  $\vartheta$  of the pion in laboratory system

As mentioned already in for the  $x$ - $y$ -projection of the scattered pion momentum, the influence of the RPD trigger requirement is visible in the  $\varphi$ -angle distribution. Twelve main peaks, each with three notches, are visible, which are varying in intensity for the different main peaks. The overall sinusoidal form of the distribution is due to the non-zero gradient of the incoming beam particle, which then results in a preferred direction of the scattered pion.

The in general small momentum transfer  $|t|$  in the elastic scattering process results in even a small deflection of the scattered pion. The average scattering angle is about  $\vartheta_s \approx 2$  mrad and limits the number of available tracking detector systems along the spectrometer described in Sec. 3.2.1.

## 5.6 Squared Four-Momentum Transfer $|t|$

The main focus within this thesis is the squared four-momentum transfer  $|t|$ . It is used for a comparison with previous experiments and serves an access to the underlying theory of high-energy scattering processes.

In Fig. 5.8 the spectrum of the momentum transfer  $|t|$  measured by the spectrometer is shown. Visible is the exponential behavior of the  $|t|$ -distribution. Due to the large amount of data recorded for this process well-founded statements based on this kinematic variable are possible. Unfortunately the geometrical acceptance of the RPD limits the accessible range to  $|t| \leq 4.5 \text{ GeV}^2/c^2$  as discussed in Sec. 4.3.

## 5.7 Overview of Runs and Cuts

The discussed data was taken in the year 2008 period. During the data taking of the so-called periods W33, W35 and W37, a total number of about 7 billion events was recorded. After the pre-selection cuts (Sec. 5.1) about 3 billion events remain.

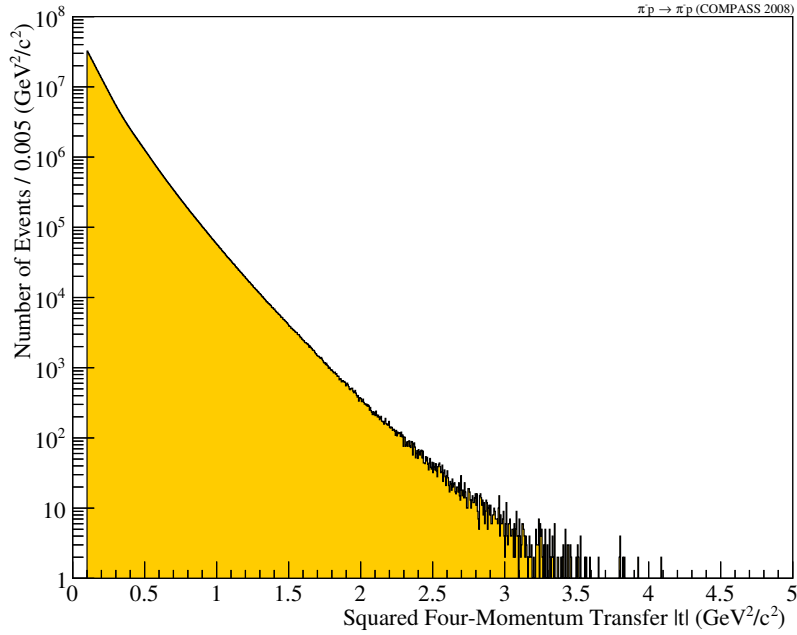
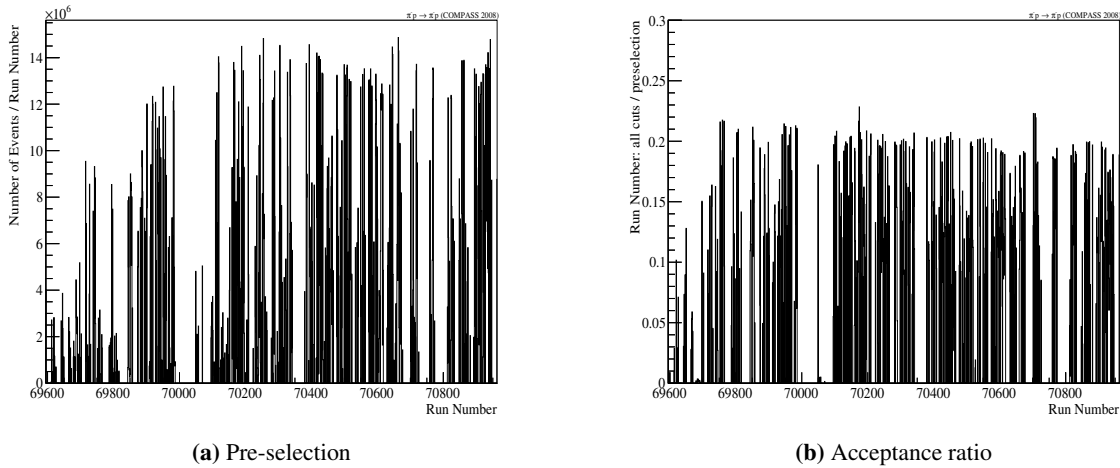


**Figure 5.8:** Squared four-momentum transfer  $|t|$  measured by the spectrometer.



(a) Pre-selection

(b) Acceptance ratio

**Figure 5.9:** Overview of used run numbers and number of events contained with pre-selection cuts in (a). In (b) the ratio between the number of accepted events after all cuts and the initial events after the preselection is shown.

In Fig. 5.9 the total number of events after the application of the described pre-selection cuts for each used run number taken within the data taken periods is shown. Additionally, the ratio between the accepted events after all applied cuts and the initial events is given. The overall acceptance of events is stable and about 20%, which results in a total number of useful events in the elastic scattering process of about 500 million.



## Chapter 6

# Monte Carlo Simulation of COMPASS

Besides the measurements of real physic events the comparison with simulated data is important. Due to the full knowledge of the experimental setup, the used materials and detector locations within the simulation, effects caused by these are much easier to investigate and the resulting influences on the measured real data can be studied.

### 6.1 Monte Carlo Chain

The used Monte Carlo simulation is divided into several steps. At first realistic events comparable to the real data are generated depending on the required physics process. For the elastic scattering process they consist of a beam particle, a primary vertex position, a recoil proton and a scattered pion. This event generation is further discussed in the following section (Sec. 6.2). Within the framework of the Geometry and Tracking (GEANT)[24] software, the COMPASS experiment is simulated in COMGEANT. It is used to propagate the particles from the generator, but also all secondary particles, through the spectrometer. Various interactions within the spectrometer material, like multiple scattering, hadronic and electromagnetic showers, are taken into account. Also in-flight decays, as well as pile-up events are considered.

The reconstruction of the events is performed by CORAL, which has been introduced in Sec. 3.2.3. CORAL uses the ROOT geometry package to cover the influences of materials along the reconstructed track. The whole reconstruction of the events is identical to the real-data reconstruction. The simulation of the detector response, also taking detector efficiencies, misalignment and resolution into account, is done in CORAL. The further analysis with PHAST and ROOT of the Monte Carlo data is identical to the real data analysis described in Sec. 3.2.3.

### 6.2 Event Generator for Elastic Scattering

For COMGEANT an event generator is required to generate an input event, which is then propagated through the simulated spectrometer. To generate events close to reality a so-called *beamfile* is used. It contains information about the vertex  $x_0$ - and  $y_0$ -position at  $z_0=0$  cm, as well as the calculated beam momenta from the data. This has the advantage of including the dependence between the scattered momenta and the primary vertex position. A Gaussian smearing is applied to the information from the beamfile within the 5-dimensional space of vertex position and beam momentum [25].

Due to the attenuation of the beam inside the liquid-hydrogen target the primary vertex  $z$ -position needs to be modified for the Monte Carlo simulation. Based on the density  $\rho_{\text{LH}_2}$  and the nuclear interaction length  $\lambda_{\text{LH}_2}$  of liquid hydrogen [26], the mean free path inside the target is calculated via Eq. (6.3).

$$\rho_{\text{LH}_2} = 0.071 \frac{\text{g}}{\text{cm}^3} \quad (6.1)$$

$$\lambda_{\text{I,LH}_2} = 52.0 \frac{\text{g}}{\text{cm}^2} \quad (6.2)$$

$$\lambda_p = \frac{\lambda_{\text{I,LH}_2}}{\rho_{\text{LH}_2}} = 732.4 \text{ cm} \quad (6.3)$$

The exponential attenuation of the beam intensity is used to generate the primary vertex  $z_0$ -position. The  $x_0$ - and  $y_0$ - position received from the beamfile is extrapolated to the calculated  $z_0$ -position via Eqs. (6.4, 6.5).

$$x_1 = x_0 + (z_1 - z_0) \cdot \nabla_{x,b} \quad (6.4)$$

$$y_1 = y_0 + (z_1 - z_0) \cdot \nabla_{y,b} \quad (6.5)$$

With  $x_1, y_1$  as the new extrapolated vertex position,  $x_0, y_0$  as the initial vertex position based on the real data at  $z_0 = 0$  cm, the attenuated  $z_1$ -position and the beam gradient along  $z$ -direction  $\nabla_{x/y,b}$ .

Starting with a known beam particle the kinematics of the scattered pion and the recoil proton are defined by the azimuthal angle  $\varphi$ , which is simply generated flat between  $\varphi = 0$  and  $\varphi = 2\pi$ , and one additional variable. Here the squared four-momentum transfer  $|t|$  has been chosen.

Two different approaches are used,  $|t|$  is either distributed according to an exponential distribution based on real-data values or as a flat distribution. The latter is used for acceptance corrections at large values of  $|t|$ , which could expose possible limitations of the spectrometer, such as the geometrical limitation of the RPD as one example (Sec. 4.3).

From the kinematics in the elastic scattering process discussed in Sec. 2.3 the recoil proton vector and the scattered pion vector are calculated. Based on the randomly generated momentum transfer  $|t|$  the energy of the recoil proton is calculated via Eq. (2.20). With the absolute momentum of the recoil proton calculated via the general energy-momentum relation the  $z$ -component of the recoil proton momentum is calculated via Eq. (6.6).

$$p_{4,z} = \frac{m_3^2 - m_1^2 - m_2^2 - m_4^2 - 2(m_2 E_1 + E_1 E_4 + m_2 E_4)}{|\vec{p}_1|} \quad (6.6)$$

$$\stackrel{\text{el. scat.}}{=} \frac{-2(m_p^2 + m_p E_1 - E_1 E_4 - m_p E_4)}{|\vec{p}_1|}$$

The scattering angle of the recoil proton  $\vartheta_{s, \text{rec}}$  is given by

$$\vartheta_{s, \text{rec}} = \text{acos} \left( \frac{p_{4,z}}{|\vec{p}_4|} \right) \quad (6.7)$$

The three-vector of the recoil proton momentum is given by

$$\vec{p}_4 = \begin{pmatrix} |\vec{p}_4| \cdot \sin(\vartheta_{s, \text{rec}}) \cdot \cos(\varphi) \\ |\vec{p}_4| \cdot \sin(\vartheta_{s, \text{rec}}) \cdot \sin(\varphi) \\ |\vec{p}_4| \cdot \cos(\vartheta_{s, \text{rec}}) \end{pmatrix} \quad (6.8)$$

Due to the inclination of the beam it is necessary to rotate the calculated recoil proton from the lab system onto the beam axis.

The scattered pion is then calculated by the difference of the Lorentz vectors as defined in Eq. (2.2).

### 6.3 Problems in RPD Simulation

The generated flat squared four-momentum transfer  $|t|$  distribution results in a wide illumination of the whole spectrometer. This reveals problems, especially in edge regions of detector planes and errors in the Monte Carlo Simulation. Two problems within the simulation of the RPD were found.

One problem is caused by the construction of the scintillator slabs of ring B with the active light guide. In the simulation this is constructed as a combination of multiple volumes, resulting in a contact surface of two segmented active materials. In the simulation of the RPD, particles, which pass both distinct active segments generate two different hits, assigned to two different tracks. If one requires only one track found in the RPD, these events are rejected. This results in a band with no events visible in Fig. 6.1b situated at the  $z$ -position  $z \approx 15$  cm of the contact surface of the two segments. This effect is not visible in the real data.

The length of the ring B slabs is the second problem. The triangular shapes in Fig. 6.1 are caused by the light guides, and can be used to estimate the end of the slabs of ring B, which allows an assumption for the total length. In the simulation and the real data both lengths seem to be in agreement. In the Monte Carlo simulation it is set to a length of 106 cm. For the real RPD the length is assumed as 115 cm in [18], but this is in contract to the measured data. On the assumption, that the central position of the RPD at  $z_{\text{RPD}} = -36$  cm is correct in the experiment setup and the simulation and the ring B slabs are centered at this position, the end position of the slabs should be at  $z = 15$  cm or  $z = 21$  cm, if the length is either 106 cm or 115 cm. Within this thesis the length of the slab is assumed to be 106 cm, which seems to be in agreement with the real data.

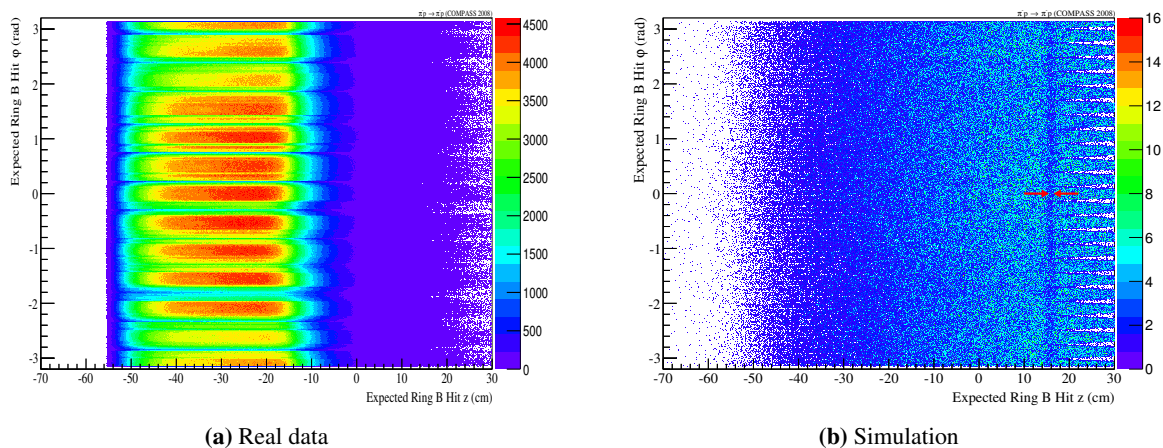


**Figure 6.1:** Comparison between the RPD hitmaps for real data and Monte Carlo simulation. For visualization of the length for the ring B slabs and the double hit treatment within the Monte Carlo simulation only the cut on the number of RPD tracks is applied for the simulation. For the real-data picture more cuts are applied to obtain the visible shapes of the slabs and the rough shadow of the light guides.



# Chapter 7

## Acceptance and Resolution

For a well-founded understanding of the measured data, the unavoidable imperfections of the spectrometer need to be taken into account. Therefore, a realistic Monte Carlo simulation of the whole setup is essential. Resulting from the spectrometer simulation are the resolutions of the measured kinematic quantities, as well as the acceptance estimation of the spectrometer itself.

The two important quantities within the simulation are on the one hand the generated Monte Carlo events, the so-called *Monte Carlo truth*, which are not influenced by any reconstruction, and on the other hand the reconstructed Monte Carlo events, which are passed through the simulation. They are reconstructed and influenced by the applied cuts.

Acceptance effects caused by the different detector components result in a different weighting within the kinematic variables. With the knowing of the acceptance for each variable, these effects can be removed from the measured real data.

### 7.1 Acceptances

In general the acceptance is defined as the ratio of the reconstructed and accepted Monte Carlo events and the generated events. To avoid bin migration, caused by the finite resolution of the spectrometer, the discussed variable is handled without their respective cut. Dividing the measured data distribution by the obtain acceptance of the respective variable, results in an acceptance corrected distribution without the influences of the spectrometer.

Thus Monte Carlo generated events are passed through the simulation of the spectrometer and reconstructed with the identical software used for the real-data production.

In the following sections the acceptance of the vertex in  $x$ -,  $y$ - and  $z$ -projection and of the squared four-momentum transfer  $|t|$  are discussed. From the generated events based on the flat squared transfer  $|t|$ -distribution for the Monte Carlo simulation in the range from 0 to  $10 \text{ GeV}^2/c^2$  are only about 25% accepted by the spectrometer. Therefore, the overall acceptance of the primary vertex and momentum is reduced.

#### 7.1.1 Primary Vertex

In Fig. 7.1 and Fig. 7.2 the acceptance and comparison between the uncorrected and the acceptance corrected distribution of the primary vertex  $x$ - and  $y$ -projection is shown. The acceptance is nearly flat within the radial extend of the target.

The applied acceptance correction of the primary vertex distribution in  $x$ - and  $y$ -projection has only a small influence on the measured data, due to the uniform acceptance. The events at the edge regions are caused by bin migration and resolution effects.

The geometrical acceptance of the RPD (Sec. 4.3) depends on the primary vertex  $z$ -position and the value of the momentum transfer  $|t|$ . The dependence for the RPD is shown in Fig. 4.5. This influence is

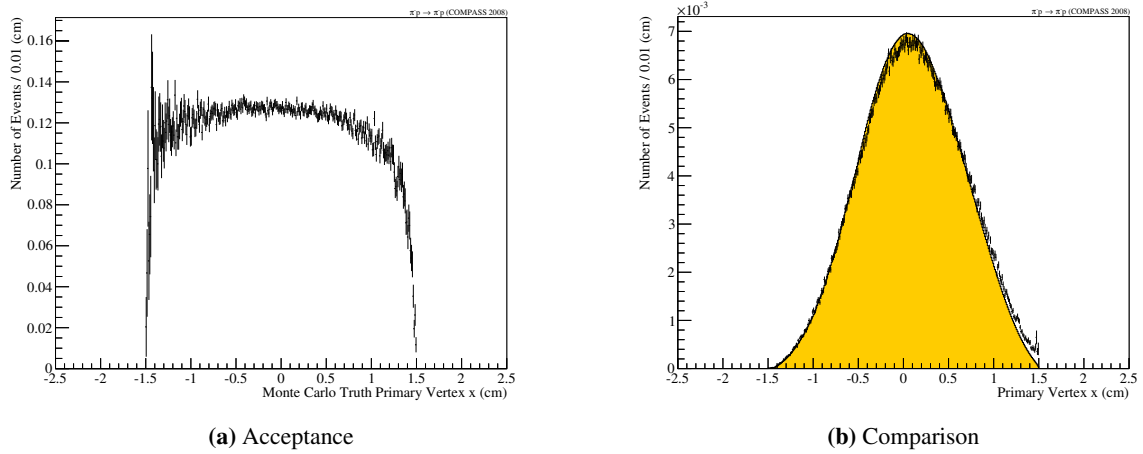


**Figure 7.1:** The acceptance of the primary vertex position in  $x$ -direction is shown in (a) and the comparison between the uncorrected and acceptance corrected primary vertex distribution in  $x$ -direction is shown in (b).

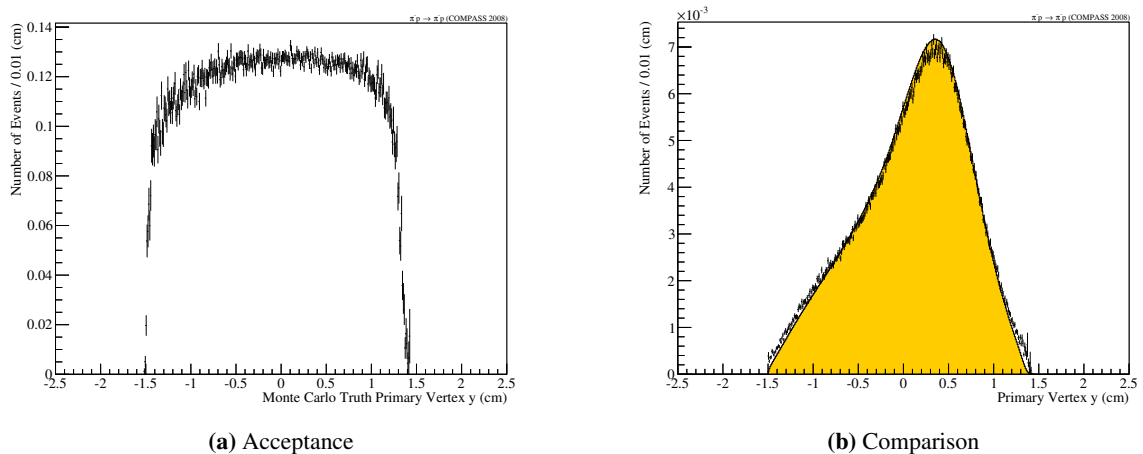


**Figure 7.2:** The acceptance of the primary vertex position in  $y$ -direction is shown in Fig. (a) and the comparison between the uncorrected and acceptance corrected primary vertex distribution in  $y$ -direction is shown in Fig. (b).

also visible in the primary vertex  $z$ -acceptance as shown in Fig. 7.3.

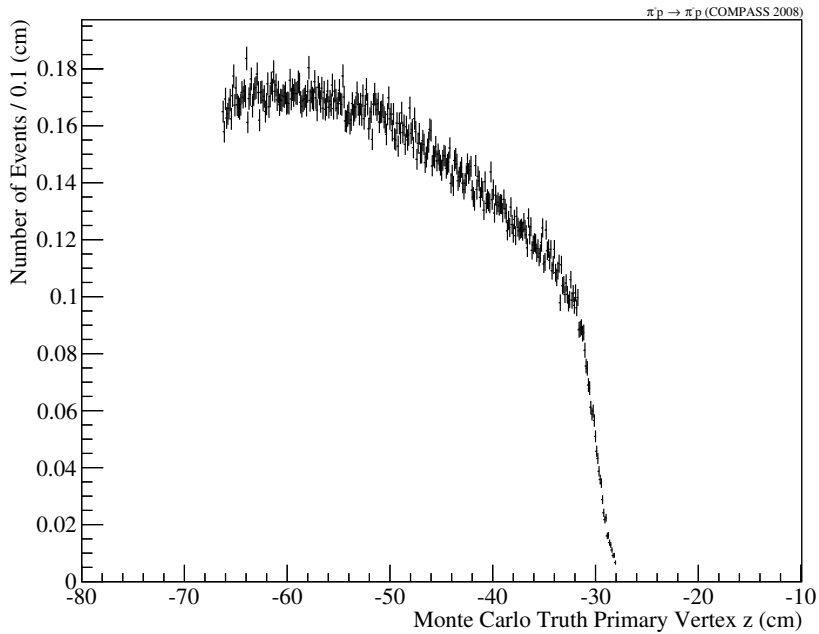


**Figure 7.3:** Primary vertex  $z$  acceptance based on a flat momentum  $|t|$ -distribution used for the Monte Carlo simulation.

Comparable to this geometrical acceptance of the RPD, the acceptance for the primary vertex  $z$ -distribution also depends on the  $z$  position itself. Therefore, the acceptance for the generated flat momentum  $|t|$ -distribution behaves like expected as it is decreasing with larger  $z$ -position. This dependence makes an acceptance correction of the real data, which follows an exponential distribution, meaningless and is therefore not applied.

### 7.1.2 Squared Four-Momentum Transfer $|t|$

To investigate Regge theory the squared four-momentum transfer  $|t|$  distribution is important. Especially at large squared four-momentum  $|t|$  a good statistic and acceptance is required for a comprehensive analysis. The acceptance of the momentum transfer  $|t|$  is shown in Fig. 7.4a. In the region  $|t| < 1 \text{ GeV}^2/c^2$  the acceptance is nearly flat. For larger  $|t|$  the acceptance decreases, ending up at the geometrical limit  $|t| \approx 4.5 \text{ GeV}^2/c^2$  caused by the RPD.

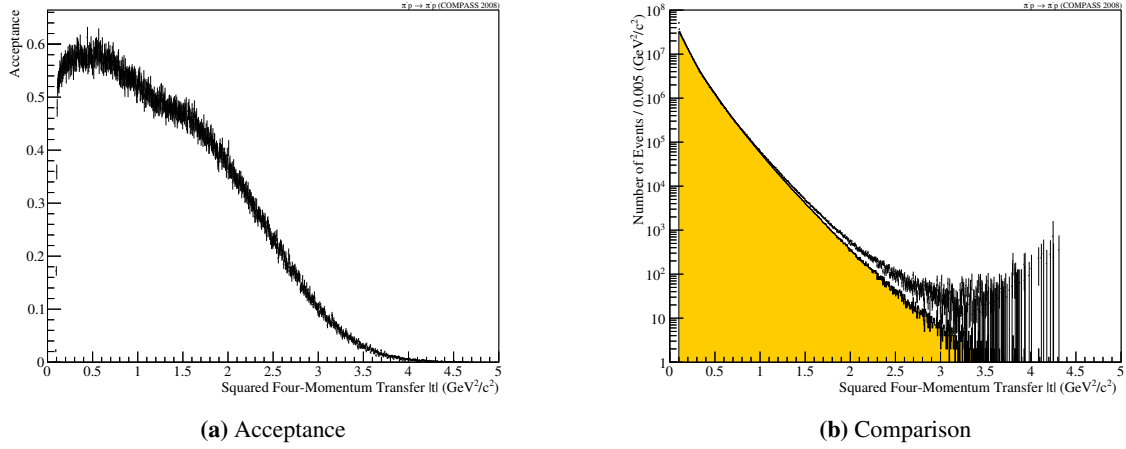


**Figure 7.4:** In (a) the acceptance for the squared four-momentum transfer  $|t|$  is shown. A comparison between the acceptance corrected and the uncorrected distribution is depicted in (b).

In Fig. 7.4b the comparison between the directly measured and acceptance corrected squared four-momentum transfer  $|t|$  spectrum is shown. For  $|t| > 3 \text{ GeV}^2/c^2$  the error due to the lack of statistic causes an increasing error. Due to the decreasing acceptance at  $|t| > 1 \text{ GeV}^2/c^2$  the spectrum is slightly bent upward. This result is important for the theory, because it has a major influence on the slope and form of the squared four-momentum  $|t|$  spectrum. Nevertheless the huge statistical errors in the region for  $|t| > 3 \text{ GeV}^2/c^2$  limit the possibility of precise prediction within this region. An in-depth discussion of the used theories can be found in Sec. 8.

## 7.2 Resolutions

The resolution of a kinematic variable depends on the reaction taking place. It is obtained via the Monte Carlo simulation and defined as the Gaussian  $\sigma$  of the spectrum of the difference between the generated Monte Carlo truth and the reconstructed value. For an easier comparison of the resolution it is divided by the respective quantity itself to obtain the relative resolution for each value.

In the following sections the relative resolutions of the primary vertex in  $x$ -,  $y$ - and  $z$ -direction, the scattered pion momenta and as well the relative resolution of the squared four-momentum  $|t|$  is presented.

### 7.2.1 Primary Vertex

The primary vertex resolution is limited for the elastic scattering case due to the single outgoing track. Mainly contributing are the small area detectors (Sec. 3.2.1), especially the silicon detectors with a resolution of about  $\sigma_{\text{Si}} = 10 \mu\text{m}$ . Nevertheless the resolution for the vertex in  $x$ - and  $y$ -projection is stable over the target region and shown in Fig. 7.5. The resolution in the  $x$ -projection is  $\sigma_x = 40 \mu\text{m}$  and in the  $y$ -projection is  $\sigma_y = 34 \mu\text{m}$ .

The difference in the resolution in the  $x$ - and  $y$ -projection could be caused by the influence of the spectrometer magnets, which bend the track into the  $y$ -direction and therefore the reconstruction error is reduced due to a larger lever arm of the reconstructed track.

In Fig. 7.6 the resolution of the primary vertex  $z$ -projection is shown. The average resolution in  $z$  is  $\sigma_z = 1 \text{ cm}$ . The main contributors in vertexing are the silicon detectors downstream of the target. The

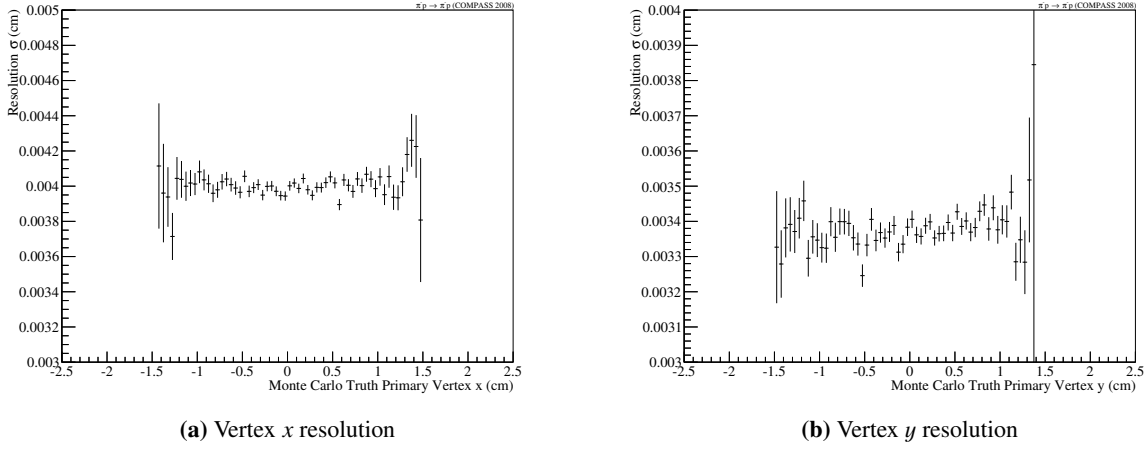


**Figure 7.5:** Resolutions of the primary vertex in  $x$ - and  $y$ -direction.

increased lever arm along the longitudinal distance between the primary vertex and the silicon stations result in a much better resolution for primary vertices situated more upstream in the target, then vertices situated closer to the silicon detectors.

### 7.2.2 Momenta of the Scattered Particle

The resolution in the kinematic variables of the scattered pion is important and has a great influence of the resolution of the squared four-momentum transfer  $|t|$ , which is calculated via this kinematics. Both resolutions for the  $x$ - and  $y$ -projection of the momentum of the scattered particle have a decreasing resolution with larger value in the respective direction and are shown in Fig. 7.7. The resolution in  $y$ -direction is increased compared to the  $x$ -direction, which is caused by to the spectrometer magnet. It fans out the momenta in  $y$ -direction, which results in an enhance track reconstruction. Furthermore, the resolution in  $x$ -direction is more spread compared to the  $y$ -direction.

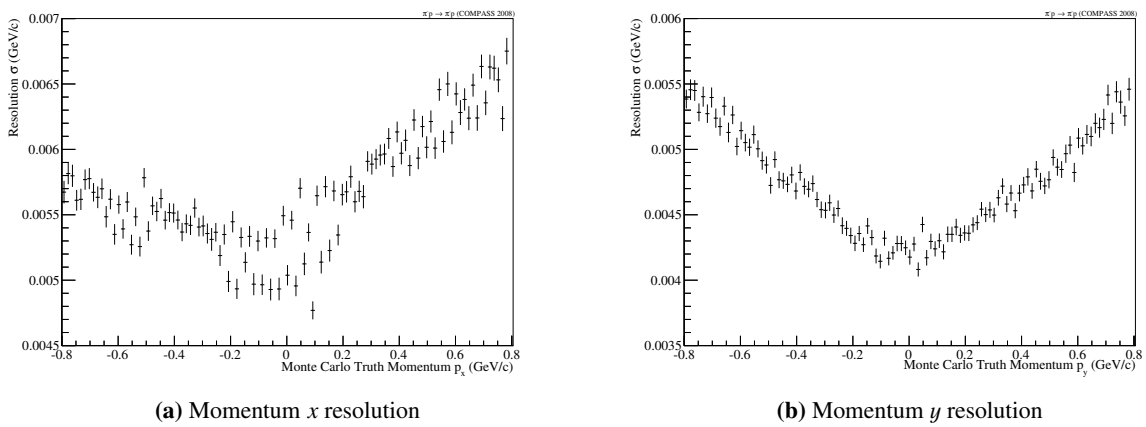


**Figure 7.7:** Resolutions of the scattered momenta in  $x$ - and  $y$ -direction.

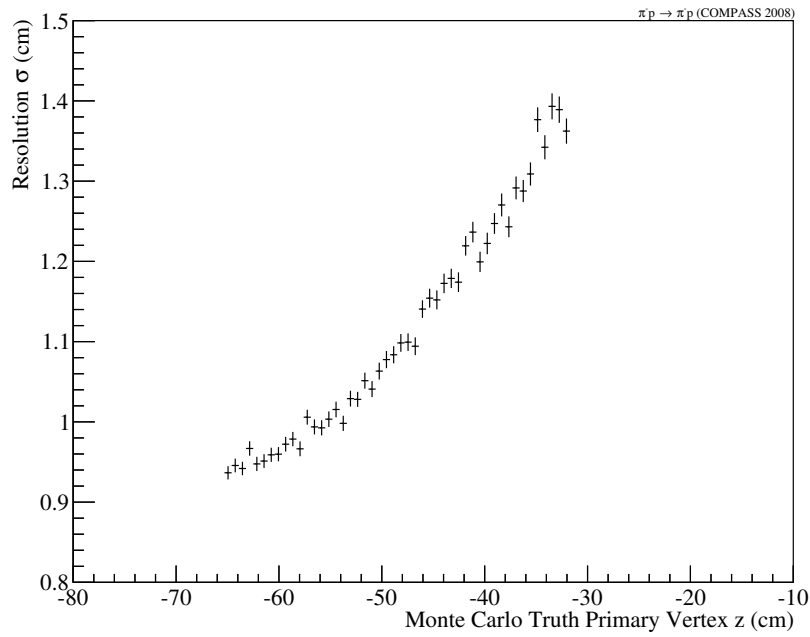


**Figure 7.6:** Resolution of the primary vertex in  $z$ -direction.

The resolution of  $z$ -component of the scattered pion is shown in Fig. 7.8. It is nearly flat over the range  $187 \text{ GeV}/c \leq p_z \leq 193 \text{ GeV}/c$ . This section covers the main part of the scattered momentum in  $z$ -direction (Fig. 5.6b).

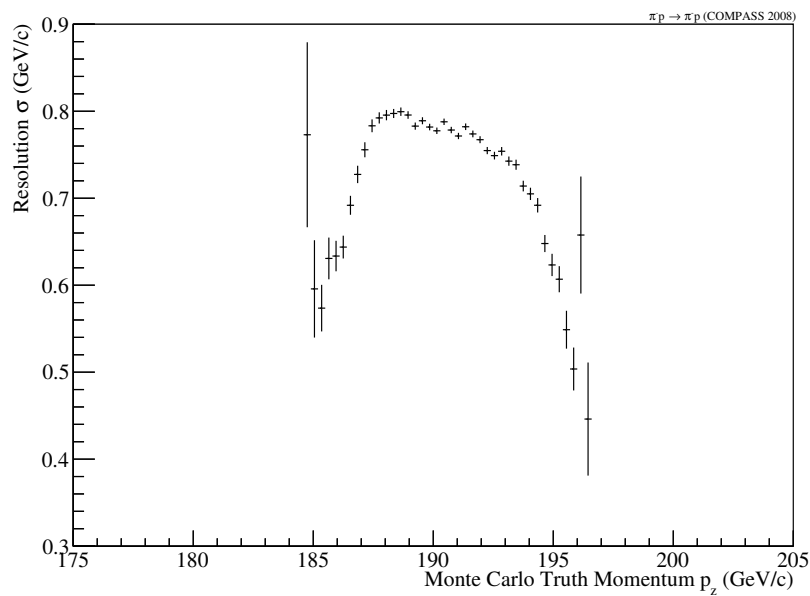


**Figure 7.8:** Resolution of the scattered momentum in  $z$ -direction.

### 7.2.3 Squared Four-Momentum Transfer $|t|$

The relative resolution of the momentum transfer  $|t|$  is shown in Fig. 7.9. Visible is a improvement of the relative resolution with increasing  $|t|$ . It flattens out at  $|t| > 1 \text{ GeV}^2/c^2$ . This could be caused by the larger scattering angle of the scattered pion, which is then nearly unchanged with respected to the beam for small values of  $|t|$ . Additional the small scattering angle of the pion limits the contributing detector planes. For increasing  $|t|$  values the scattering angle increases and also the number of contributing detector planes increases, as well as the scattering angle itself, which results in an improved measurement of the scattering angle with smaller errors.

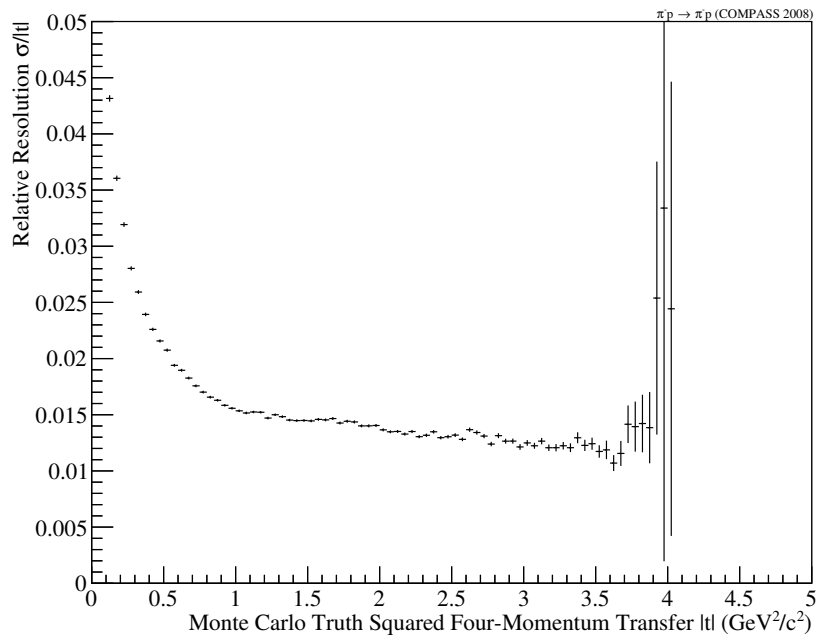


**Figure 7.9:** Relative resolution of the squared four-momentum transfer  $|t|$ .



# **Part IV**

# **Results**



# Chapter 8

## Theoretical Interpretation

As discussed in Sec. 2.5, the regime of Regge and Pomeron exchange is not fully understood. Many different theoretical approaches try to describe the elastic scattering process. In the following sections, a selection of models is discussed and compared with the measured distribution of the squared four-momentum transfer  $|t|$  for elastic pion-proton scattering measured at COMPASS in the range of  $0.1 \text{ GeV}^2/c^2 \leq |t| \leq 3 \text{ GeV}^2/c^2$ . For the comparison of different experiments the parametrization of their data can be used. Although the maximal measurable  $|t|$ -value is  $4.5 \text{ GeV}^2/c^2$  and restricted by the geometrical limitations of the RPD, the small number of reconstructed events limits the discussion to a maximal  $|t|$  of  $3 \text{ GeV}^2/c^2$ .

At first a simple approach for a parametrization of the measured  $|t|$ -distribution based on a sum with a different number of exponential functions is used. Then the description based on the model of Donnachie et al. is presented [14]. Another parametrization established by Mathieu [27] as a different approach to the Pomeron exchange is discussed in the following. Furthermore a model based on the Chou-Yang relation is presented.

### 8.1 Exponential Fit Model

A general way for the parametrization of the  $|t|$ -spectrum is the usage of a simple sum of exponential function.

Due to the exponential dependence of the scattering amplitude and a comparable behavior observed in experimental data, a sum of exponential functions is used as a simple parametrization of the data without any direct physical meaning.

$$f(t) = \sum_{i=1} e^{A_i + B_i t} \quad (8.1)$$

#### 8.1.1 Single Exponential Fit Model

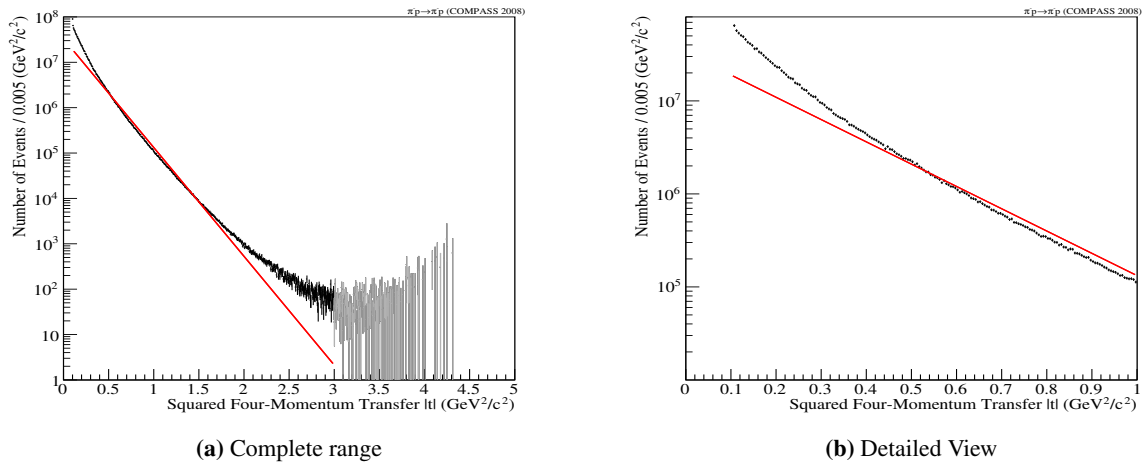
For the single exponential fit model Eq. 8.1 reduces to

$$f(t) = e^{A + Bt} \quad (8.2)$$

The fit of this model is shown in Fig. 8.1 with the resulting values given in Tab. 8.1.

**Table 8.1:** Fit results for on a single exponential description of the  $|t|$ -spectrum (Fig. 8.1).

Parameter	Estimate	Standard Error
$A$	17.31	0.01
$B$ ( $c^2/\text{GeV}^2$ )	-5.52	0.01
$\chi^2/\text{ndf}$	23123/578	


**Figure 8.1:** Single exponential description for the experimental data.

Not surprisingly, with the function given in Eq. 8.2 the description of the data is not possible. The reduced  $\chi^2$  value of 40 indicates the strong difference between the single exponential parametrization and the measured distribution. Therefore, the single exponential model seems to be too simplistic.

The general behavior of the slope parameter in dependence of  $|t|$  for a single exponential function is shown in Fig. 8.2. In a step width of  $|t| = 0.29 \text{ GeV}^2/c^2$  the single exponential function is fitted to the  $|t|$ -distribution.

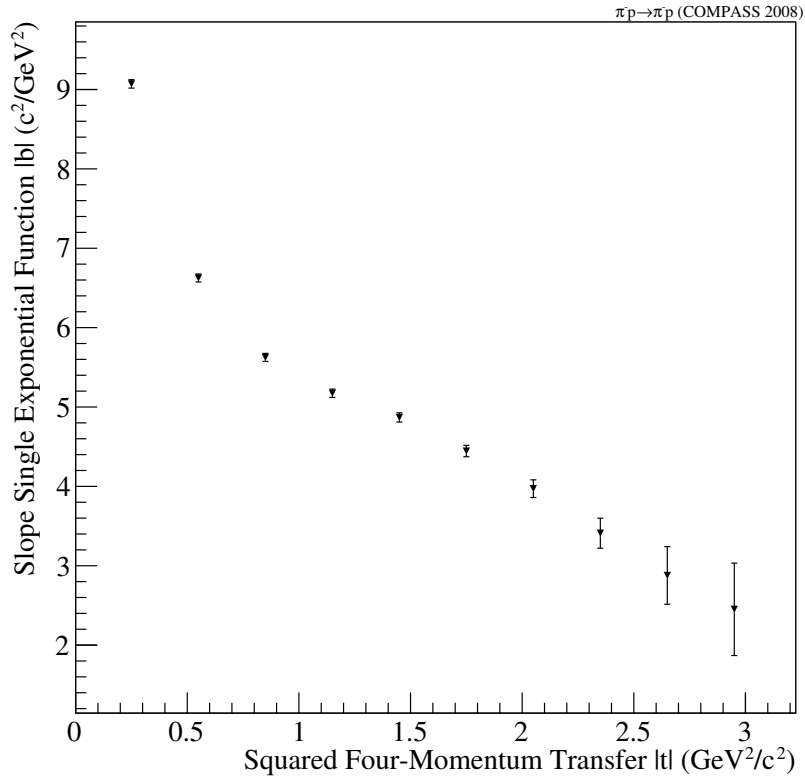


**Figure 8.2:** Slope behavior of a single exponential function in  $0.29 \text{ GeV}^2/c^2$  steps for the measured distribution in Fig. 8.1.

Visible are two different regions. In the first region from  $0.1$  to  $0.6 \text{ GeV}^2/c^2$  the slope decreases fast with  $|t|$ . In the range from  $0.6$  to  $3 \text{ GeV}^2/c^2$  the slope decrease is shallower. The indicated errors result from the fit.

### 8.1.2 Double Exponential Fit Model

As a more complex model compared to the previous single exponential function, the sum of two exponential function is used as given in Eq. 8.3.

$$f(t) = e^{A_1+B_1t} + e^{A_2+B_2t} \quad (8.3)$$

The resulting values for the fit shown in Fig. 8.3 are listed in Tab. 8.2.

**Table 8.2:** Fit results based on a double exponential description of the squared four-momentum transfer  $|t|$ -spectrum (Fig. 8.3).

Parameter	Estimate	Standard Error
$A_1$	18.53	0.01
$A_2$	15.88	0.03
$B_2$ ( $c^2/\text{GeV}^2$ )	-4.51	0.02
$B_1$ ( $c^2/\text{GeV}^2$ )	-8.70	0.05
$\chi^2/\text{ndf}$	2238/576	

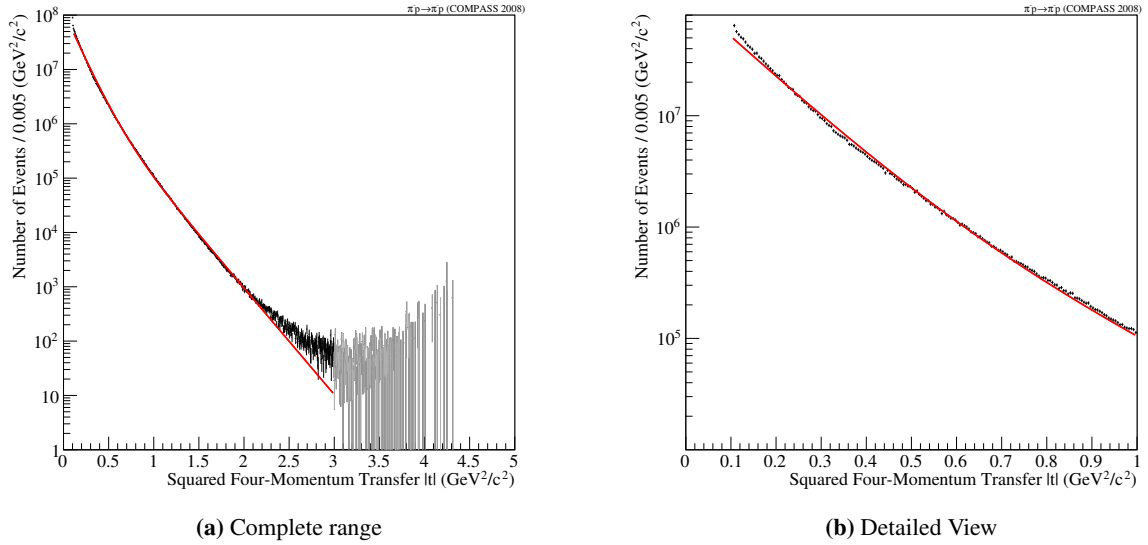


**Figure 8.3:** Double exponential description for the experimental.

The parametrization in Eq. 8.3 describes the data over a  $|t|$ -range from 0.2 to  $2 \text{ GeV}^2/c^2$ . The main differences between the fit function and the spectrum is the undershoot for low  $|t| < 0.2 \text{ GeV}^2/c^2$  and for larger values of  $|t| > 2 \text{ GeV}^2/c^2$ . An additional oscillation of the function around the data points is visible. This reflects itself in a comparatively low value of the reduced  $\chi^2$  of about 4. The obtained fit values are comparable to previous results as shown in Fig. 8.4 for the inelastic scattering channel  $\pi^- p \rightarrow \pi^- \pi^- \pi^+ p$ , fitted in a smaller fit range of  $0.1 \leq |t| \leq 1 \text{ GeV}^2/c^2$

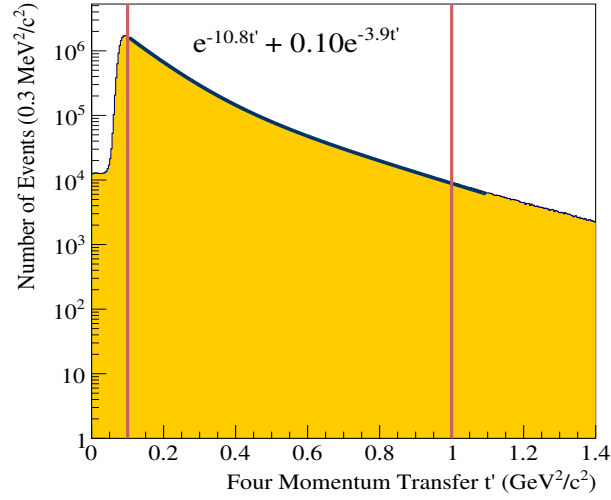


**Figure 8.4:** Double exponential fit result for inelastic pion-proton scattering in the channel  $\pi^- p \rightarrow \pi^- \pi^- \pi^+ p$  [11].

### 8.1.3 Triple Exponential Fit Model

Another parametrization was performed using the sum three exponential functions as given in Eq. 8.4.

$$f(t) = e^{A_1+B_1t} + e^{A_2+B_2t} + e^{A_3+B_3t} \quad (8.4)$$

In Fig. 8.5 the fit is depicted and the resulting fit values are given in Tab. 8.3.

**Table 8.3:** Fit results based on a triple exponential description of the squared four-momentum transfer  $|t|$ -spectrum (Fig. 8.5).

Parameter	Estimate	Standard Error
$A_2$	18.86	0.02
$A_3$	17.07	0.04
$A_1$	11.81	0.24
$B_1$ ( $c^2/GeV^2$ )	-2.73	0.09
$B_3$ ( $c^2/GeV^2$ )	-5.53	0.05
$B_2$ ( $c^2/GeV^2$ )	-11.58	0.18
$\chi^2/ndf$	452/574	

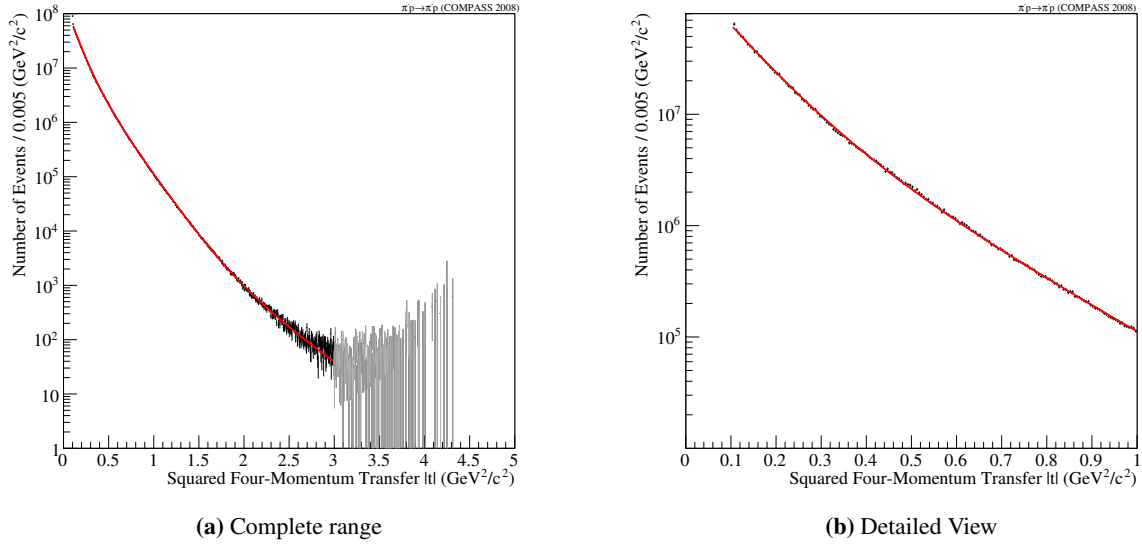


**Figure 8.5:** Triple exponential description for the experimental data.

With the function given in Eq. 8.4 the description of the data is possible over the whole range of  $|t|$  from 0.1 to 3  $\text{GeV}^2/c^2$ . The result of the reduced  $\chi^2$  of 0.8 indicates a good parametrization of the measured data.

## 8.2 Parametrization Based on the Quark Coupling

Donnachie et al. discuss in [14] the elastic scattering process. Based on the additive quark rule which implies that the Pomeron couples to the valence quarks in a hadron and not directly to the hadron itself, the model of Donnachie et al. is already in good agreement with the experimental data used in [14]. The quark coupling  $\gamma^\mu$  contributes to the quark-quark scattering ( $q_1 q_2 \rightarrow q_3 q_4$ ) and results in a scattering amplitude that is comparable to Eq. (2.67) given by

$$A(s, t) = \beta_{\mathcal{P}} (\bar{u}_3 \gamma^\mu u_1) (\bar{u}_4 \gamma_\mu u_2) e^{\frac{-i\pi}{2} \alpha_{\mathcal{P}}} \left( \frac{s}{s_0} \right)^{\alpha_{\mathcal{P}}(t)-1} \quad (8.5)$$

with  $\beta_{\mathcal{P}}$  as a constant real factor and  $e^{\frac{-i\pi}{2} \alpha_{\mathcal{P}}}$  containing the phase related to the signature in Eq. (2.68). With the optical theorem in Eq. (2.53), the total cross-section for unpolarized quark-quark scattering via the amplitude can be calculated in order to justify the exponent of  $s$  implying the Regge trajectory  $\alpha_{\mathcal{P}}(t)$ .

$$\sigma_{qq} = \frac{\beta_{\mathcal{P}}^2}{s} \left[ \frac{1}{2} \text{tr}(\gamma p_1 + m_q) \gamma^\mu \right] \left[ \frac{1}{2} \text{tr}(\gamma p_2 + m_q) \gamma_\mu \right] \cos \left( \frac{1}{2} \pi (\alpha_{\mathcal{P}}(0) - 1) \right) \left( \frac{s}{s_0} \right)^{\alpha_{\mathcal{P}}(0)-1} \quad (8.6)$$

The proportionality of the total cross-section is given by

$$\sigma_{qq} \sim 2\beta_{\mathcal{P}}^2 \cos \left( \frac{\pi}{2} (\alpha_{\mathcal{P}}(0) - 1) \right) \left( \frac{s}{s_0} \right)^{\alpha_{\mathcal{P}}(0)-1} \quad (8.7)$$

which is in agreement with the general  $s$ -dependence for the total cross-section for Reggeon exchange given in Eq. (2.69). In pion-proton scattering the wave functions of each contributing hadron needs to

be taken into account and therefore the proton and pion form factors  $F_p(t)$  and  $F_\pi(t)$  are required.

$$F_p(t) = \frac{4m_p^2 - 2.79t}{4m_p^2 - t} \frac{1}{\left(1 - \frac{t}{0.71 \text{ GeV}^2}\right)^2} \quad \text{and} \quad F_\pi(t) = \frac{1}{\left(1 - \frac{t}{0.5 \text{ GeV}^2}\right)^2} \quad (8.8)$$

Both form factors are shown in Fig. 8.6. The parametrization of the pion form factor is based on a fit to experimental data from [28, 29].

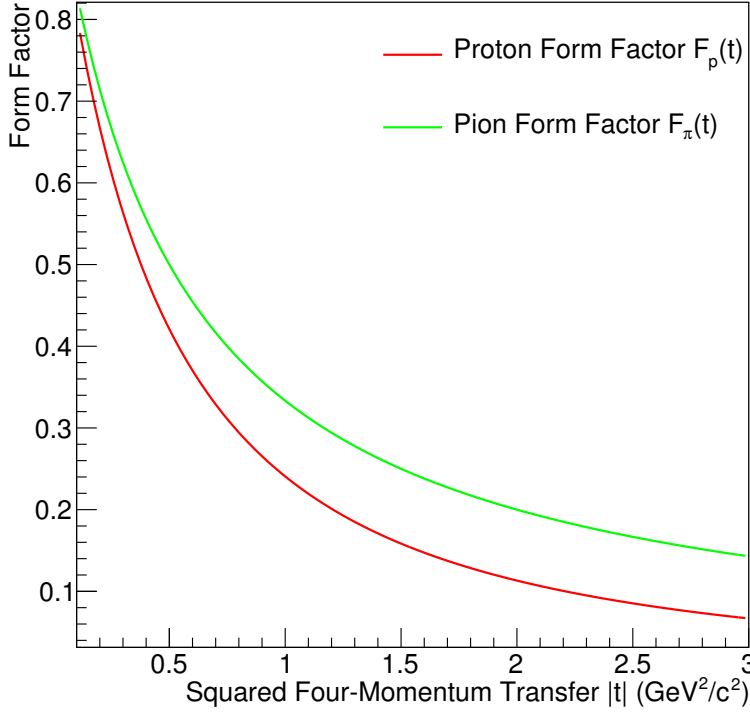


**Figure 8.6:** Form factors of the pion (green) and the proton (red) used for the description of Pomeron exchange in elastic pion-proton scattering. The parametrization is taken from [14] and is based on experimental data from [28, 29].

From Eq. (8.5) the differential cross-section can be derived:

$$\frac{d\sigma}{dt} = \frac{(2\beta_\pi F_\pi(t))^2 (3\beta_p F_p(t))^2}{4\pi} \left(\frac{s}{s_0}\right)^{2\alpha_\varphi(t)-2} \quad (8.9)$$

This includes the contributing form factors and the number of the valence quarks, two for the pion and three for the proton. The used Regge trajectory  $\alpha_\varphi(t)$  is

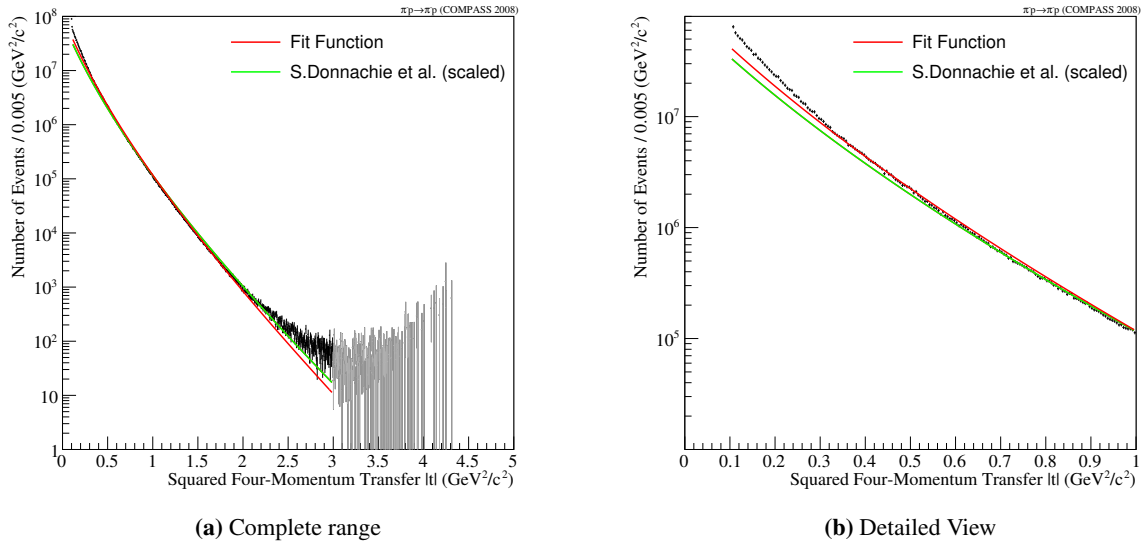
$$\alpha_\varphi(t) = 1 + \epsilon_\varphi + \alpha_\varphi t \quad (8.10)$$

The function in Eq. 8.9 is used to describe the  $|t|$ -distribution in the elastic pion-proton process in a range from 0.1 to 3 GeV<sup>2</sup>/c<sup>2</sup> at a center-of-mass energy of  $\sqrt{s} = 19$  GeV. The resulting fit is shown in Fig. 8.7

**Table 8.4:** Fit results for the Donnachie et al. description (Fig. 8.7).

Parameter	Estimate	Statistical Error	Estimate [14]	Statistical Estimate
$\beta_{\mathcal{P}}$ (a.u.) ( $10^5$ )	7.32	0.24		
$\epsilon_{\mathcal{P}}$	0.21	0.02	0.08	
$\alpha_{\mathcal{P}}$ ( $\text{GeV}^{-2}$ )	0.27	0.01	0.25	
scaling (a.u.) ( $10^6$ )			2.67	0.05
$\chi^2/\text{ndf}$	4082/577		7325/579	

with the fit values given in Tab. 8.4.


**Figure 8.7:** Squared four-momentum transfer distribution with the theoretical description based on Donnachie et al. [14].

The resulting  $\epsilon_{\mathcal{P}}$  value from the fit is larger compared to [14], but the fact that  $\epsilon_{\mathcal{P}} > 0$  is in agreement with the requirement of Pomeron trajectories to have an intercept of  $\alpha(0) > 1$ . The value for  $\alpha_{\mathcal{P}}$  is comparable to the one in [14]. The factor, which includes the luminosity to normalize the measured “Number of Events” to the differential cross-section is unknown. Therefore the fit constant  $\beta_{\mathcal{P}}$  differs from the fits using the differential cross-section as in [14].

The fit function based on [14] is in a good agreement with their given results. However, the description deviates from the measured data. The rather large reduced  $\chi^2 \approx 7$  results from the undershoots in the low- $|t|$  region of  $|t| \leq 0.3 \text{ GeV}^2/c^2$  and in the high  $|t|$  region beyond  $|t| \geq 2 \text{ GeV}^2/c^2$ . However, in the range between  $0.3$  to  $2 \text{ GeV}^2/c^2$  the model is able to follow the data.

In comparison (Fig. 8.7) with the model from Donnachie et al. and the parameter values from [14] the undershoot of the fit function is smaller for the  $|t|$ -region below  $0.3 \text{ GeV}^2/c^2$ . For the  $|t|$  region above  $2 \text{ GeV}^2/c^2$  the parameters of Donnachie et al. produce a smaller undershoot of the model compared to

the fit. With a reduced  $\chi^2 \approx 12$  the model with the parameters from Donnachie et al. is not as good in describing the data as the function with the fitted parameters.

### 8.3 Quadratic Term in Pomeron Trajectory

Based on elastic pion-nucleon data from [30] at different energies, a parametrization developed by Mathieu is applied that assume only single Pomeron exchange and a quadratic term in the Pomeron trajectory (Fig. 8.8). This fit is later used with a normalization to the measured momentum transfer  $|t|$  at COMPASS. As mentioned in the previous section a transition to differential cross-section is not yet possible due to missing normalization.

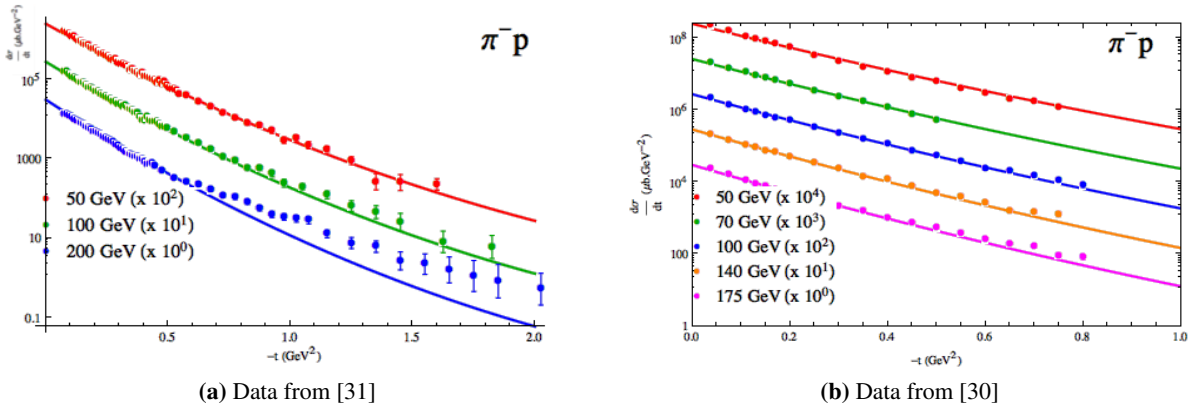


**Figure 8.8:** Experimental data from [30] and [31]. The differential cross-section for elastic pion-proton scattering for different energies is shown, as well as the fit function from [27].

The quadratic term in the Pomeron trajectory reads

$$\alpha(t) = 1.08 + \alpha'_{\mathcal{P}}t + \alpha''_{\mathcal{P}}t^2 \quad (8.11)$$

The amplitude is given by

$$A(s, t) = \beta_{\mathcal{P}} e^{b_{\mathcal{P}}t} \Gamma(1 - \alpha(t)) \left(1 + e^{-i\pi\alpha(t)}\right) s^{\alpha(t)} \quad (8.12)$$

resulting in the differential cross-section with a normalization

$$\frac{d\sigma}{dt} = \frac{|A(s, t)|^2}{64\pi m_p^2 p_{\text{lab}}^2} \quad (8.13)$$

The normalization contains the flux factor  $m_p p_{\text{lab}} = q \sqrt{s}$  with the breakup momentum  $q$ . The obtained values from the fit in Eq. (8.13) applied by Mathieu for the measured data as shown in Fig. 8.8b a prediction for the COMPASS data is possible. The result of the prediction is shown in Fig. 8.9 and the parameter values are listed in Tab. 8.5.

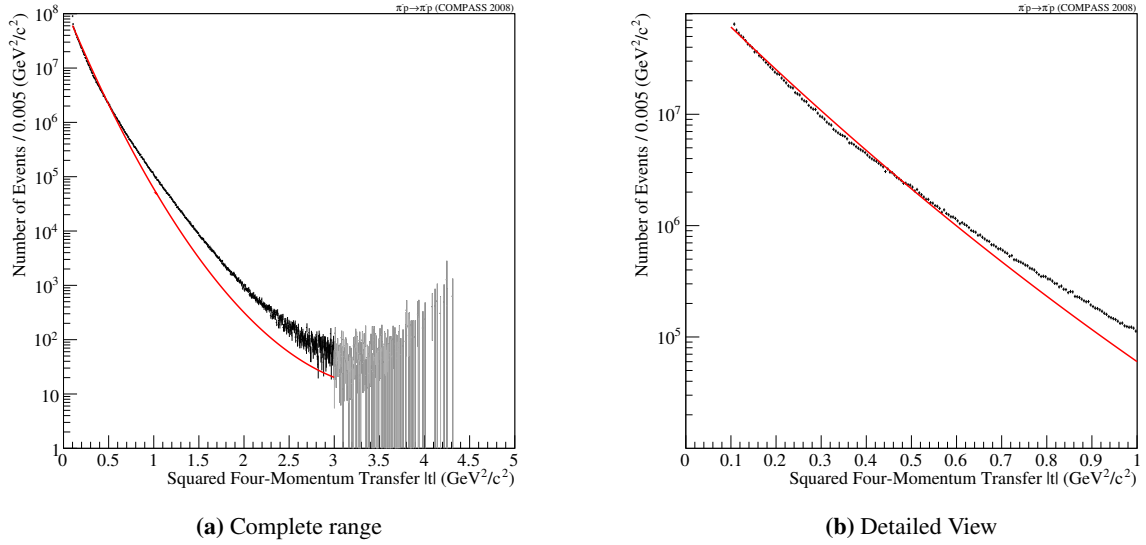


**Figure 8.9:** Model based on a squared term in Pomeron trajectory [27] for the measured COMPASS data. It is based on a fit of experimental data for different energy from [30].

**Table 8.5:** Fit results [27] based on data for different energy ranges shown in Fig. 8.8b.

Parameter	Estimate [27]	Statistical Error [27]
$\beta\varphi$	12.26	0.03
$b\varphi$	2.27	0.04
$\alpha'_{\varphi}$	0.41	0.01
$\alpha''_{\varphi}$	0.23	0.01
scaling (a.u.)	4992	11.83

The model is in good agreement with the measured data for  $|t| < 0.5 \text{ GeV}^2/c^2$ . For larger  $|t|$ -values the slope of the measured data is not as steep as the description and a difference can be observed. This results in a constant offset between the data and parametrization for  $|t| > 1.5 \text{ GeV}^2/c^2$ . However, the tendency of the model with increasing values of  $|t|$  is comparable to the data. It seems to flatten out for  $|t| > 2 \text{ GeV}^2/c^2$ , but the parametrization tends in the right direction. Although, the flattening of the data could be caused by the strong acceptance correction of the data in this region.

The effect of the flattening of the  $|t|$ -distribution with increasing  $|t|$  and the difference between the prediction which is based on single Pomeron exchange, could also indicate possible double Pomeron exchange (Sec. 2.6). In Fig. 8.8a a comparable behavior of the  $|t|$ -distribution to the measured COMPASS data is noticeable.

## 8.4 Parametrization Based on Chou-Yang Model

In [12] the Chou-Yang relation [32] was used to develop a parametrization for elastic pion-proton scattering processes. Based on a data set measured at Fermilab [33–35] with a  $\pi^-$  beam momentum of 200 GeV/c (Fig. 1.3).

The center-of-mass energy is not included in the model. This is justifiable if the change in the total cross-section is small with the center-of-mass energy. The description based on the Chou-Yang model takes the individual form factors  $F_\pi(t)$  and  $F_p(t)$  (Fig. 8.6) of the pion and the proton into account. The amplitude in the Chou-Yang relation reads Eq. (8.14)

$$A(t) = i \int_0^\infty db b J_0(b\sqrt{|t|}) \left[ 1 - \exp \left( -C \int_0^\infty d\sqrt{|t|} F_\pi(t) F_p(t) \sqrt{|t|} J_0(b\sqrt{|t|}) \right) \right] \quad (8.14)$$

with  $C$  as a normalization constant. In [12] this relation is simplified to

$$A(t) = \alpha_1 e^{-\beta_1 \sqrt{|t|+\gamma_1}} + \alpha_2 \frac{J_1(\gamma_2 \sqrt{|t|})}{\sqrt{|t|}} e^{-\beta_2 |t|} \quad (8.15)$$

The parametrization should be valid for momentum transfers up to  $4 \text{ GeV}^2/c^2$  [12] and therefore should provide a suitable description for the COMPASS data. Additionally the fit is able to describe a possible diffractive dip caused by the vanishing imaginary part of the scattering amplitude. It is visible in Fig. 1.3, but not in the COMPASS data. The fit used for the measured elastic pion-proton scattering at COMPASS is depicted in Fig. 8.10.

The used fit function from [12] based on the approach via the Chou-Yang model is with the fitted amplitude in Eq. (8.15) is given as

$$\frac{d\sigma}{ds} = |A(s)|^2 \quad (8.16)$$

The resulting fit parameters are given in Tab. 8.6.

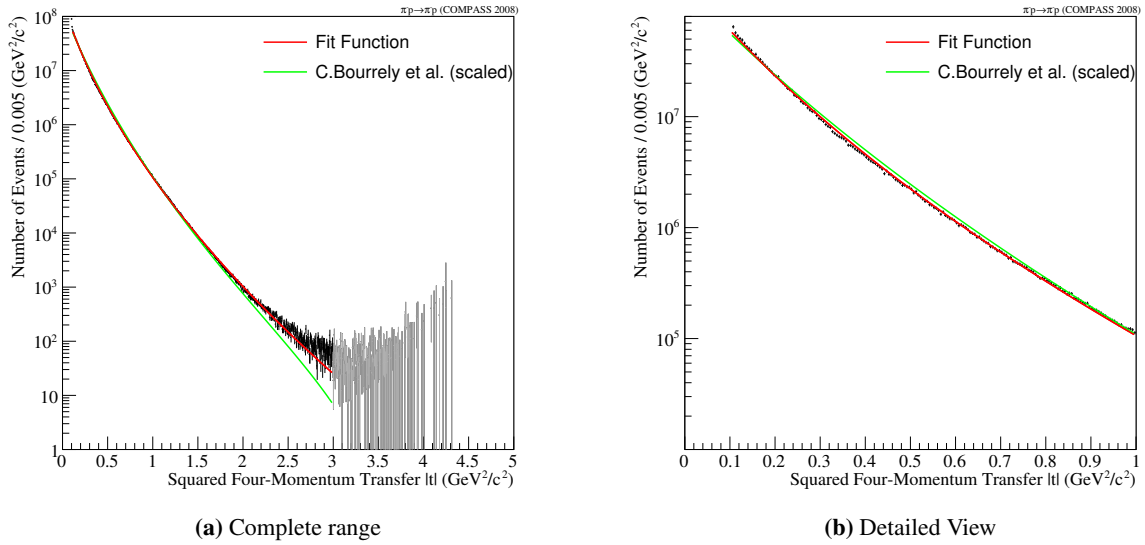


**Figure 8.10:** Parametrization based on the Chou-Yang relation.

**Table 8.6:** Fit results based on Chou-Yang model assumption (Fig. 8.10).

Parameter	Estimate (Fit)	Statistical Error (Fit)	Estimate [12]	Statistical Error [12]
$\alpha_1$ (GeV <sup>-2</sup> )	$3.34 \cdot 10^5$	0.14	705.67	0.98
$\beta_1$ (GeV <sup>-1</sup> )	6.16	0.03	6.98	$10^{-3}$
$\gamma_1$ (GeV <sup>-2</sup> )	2.74	0.01	0.51	$0.4 \cdot 10^{-3}$
$\alpha_2$ (GeV <sup>-1</sup> )	1.76	0.03	$3.86 \cdot 10^{-3}$	$0.26 \cdot 10^{-3}$
$\beta_2$ (GeV <sup>-2</sup> )	1.73	0.02	0.08	0.02
$\gamma_2$ (GeV <sup>-1</sup> )	4.54	0.09	2.62	0.04
scaling (a.u.) ( $10^6$ )			5.87	0.02
$\chi^2/\text{ndf}$	919/574		4879/579	

The description based on the Chou-Yang model is in good agreement with the data already with the given parameter values in [12] and the scaling of the mode with these parameter values results in a reduced  $\chi^2 \approx 8$ . With a reduced  $\chi^2 \approx 1.6$  the fit of this model is an outstanding description compared to the other parametrization presented in this chapter. For  $|t|$  values larger  $2 \text{ GeV}^2/c^2$  the fit is able to follow the data better compared to the parametrization in [12]. It is able to follow the measured squared four-momentum transfer  $|t|$ -distribution over the whole range between 0.1 and  $3 \text{ GeV}^2/c^2$ . The fit values are comparable to the ones given in [12], except the required scaling factors included in  $\alpha_1$  and  $\alpha_2$ . The resulting slope parameter  $\beta_1$  is in agreement with previous result in [12]. Also the obtained factor  $\gamma_1$  is roughly similar to the value of  $\gamma_1$  in [12], as well as the resulting fit value for  $\gamma_2$ . The value for  $\beta_2$  is larger compared to the value given in [12].

## 8.5 Discussion of Results

The described models for a parametrization of the data in the  $|t|$ -range from 0.1 to 3  $\text{GeV}^2/c^2$  vary in levels of agreement.

The data can be simply parameterized by a sum of exponential functions. Not surprisingly, a single exponential function is not able to describe the  $|t|$ -distribution. As visible in Fig. 8.2 the  $|t|$ -spectrum requires at least two different slopes for description. The sum of two exponential functions is in agreement with the data over the  $|t|$ -range from 0.2 to 2  $\text{GeV}^2/c^2$ . For  $|t|$ -values below 0.2  $\text{GeV}^2/c^2$  and above 2  $\text{GeV}^2/c^2$  an undershoot of the parametrization is present. This results in a reduced  $\chi^2$  of 4. Adding an additional exponential function leads to good description of the data. This parametrization has the best  $\chi^2$  of 0.8 compared to the discussed exponential ones.

In contrast to the exponential models, the presented parametrization of Donnachie, Mathieu and Chou-Yang have a sound physical motivation.

With the parametrization of Donnachie et al. [14] a description of the data is possible and has a comparable precision as the double exponential function. It shows the same problematic undershoots in the  $|t|$ -region below 0.3  $\text{GeV}^2/c^2$  and above 2  $\text{GeV}^2/c^2$ . The usage of the parameter values from [14] results in reduced  $\chi^2$  of 12. Directly fitting the parametrization to the data leads to a better  $\chi^2$  of 7.

A modification of the Regge trajectory with a quadratic term was performed by Mathieu [27]. In contrast to Donnachie et al., this description is able to follow the data for a  $|t|$  below 0.5  $\text{GeV}^2/c^2$ . However, an offset evolves between 0.5 and 1.5  $\text{GeV}^2/c^2$ , but with further increasing  $|t|$  the function has a comparable shape as the data.

The model of Chou-Yang from [12] leads to the best description of the data compared to the previous approaches. With the given parameters in [12] the parametrization is already able to describe the  $|t|$ -spectrum up to 2  $\text{GeV}^2/c^2$  with a reduced  $\chi^2$  of 8, which is comparable to Donnachie et al. Using the Chou-Yang parametrization as a fit function results in a reduced  $\chi^2$  of 1.6 and is therefore the best model for the data of all compared models besides the triple exponential parametrization.

In general the flatten of the  $|t|$ -spectrum could be cause by the strong acceptance correction in this region. The models of Donnachie et al. and Mathieu assume a single Pomeron exchange and both parametrizations are unable to follow the flatten of the data with increasing  $|t|$ . This could also be an indicator for a possible double Pomeron exchange (Sec. 2.6).



## Chapter 9

### Summary and Outlook

The large data set acquired by COMPASS in the year 2008 leads to an unprecedented statistical precision for the elastic pion-proton scattering process and is an opportunity to investigate the underlying interaction by measuring the squared four-momentum transfer  $|t|$ . Since the measurement of elastic processes was not the primary objective of COMPASS, the study of elastic scattering events reveals problematic kinematic regions of the spectrometer for this reaction.

A geometric limitation is caused by the RPD, which is used for the selection of the elastic events. It restricts the measurable range of  $|t|$  from 0.1 to 4.5  $\text{GeV}^2/c^2$  by its trigger condition.

A further investigation of the recoil proton and its kinetic energy shows problems in the energy estimation by the RPD software. The present energy correction produced artifacts in the resulting proton energy. An improved energy correction for the recoil proton was developed. Using a parametrization of tabulated values provided by NIST, the energy loss in the materials along the proton path is obtained and therefore the usability of the RPD enhanced.

Since this is the first work on elastic pion-proton scattering at COMPASS the general properties of the kinematic variables were investigated. The Monte Carlo simulation of the experiment is used to obtain the acceptance and resolution of the primary vertex and momenta distributions. With the removal of unavoidable imperfections of the spectrometer the acceptance corrected  $|t|$ -spectrum is obtained.

Using the parametrizations of different measured the  $|t|$ -distribution allows the comparison with previous experiments. At first a simple model consisting of exponential functions is used. Due to the feature of different exponential slopes within the  $|t|$ -spectrum a sum of at least two exponentials is necessary to describe the data. However, the remaining undershoots of this model for the region below 0.2  $\text{GeV}^2/c^2$  and above 2  $\text{GeV}^2/c^2$  are solved by adding an additional exponential. This sum of three exponential functions is able to follow the data over to whole range from 0.1 to 3  $\text{GeV}^2/c^2$  and has the best reduced  $\chi^2$  of 0.8 of the discussed exponential models.

Approaches with a sound physical motivation for the elastic pion-proton scattering are developed by Donnachie et al., Mathieu and Chou-Yang. The measured  $|t|$ -spectrum is in agreement with the parametrization from Donnachie et. al. The description is able to follow the data in the range from 0.3 to 2  $\text{GeV}^2/c^2$ . Undershoots occur outside of this region. The model by Mathieu describes the  $|t|$ -region below 0.5  $\text{GeV}^2/c^2$ , but generates an offset with increasing  $|t|$ , resulting in a constant difference between the parametrization and the data. However, the shape of the measured  $|t|$ -distribution can be reproduced and is comparable with previous measurements. The best description of the data is based on the Chou-Yang relation. It is able to follow the measured data over the whole range and achieves a reduced  $\chi^2$  of 1.6. Already the given parameter values from [12] lead to a good description of the data, comparable to the triple exponential parametrization.

The measured momentum transfer  $|t|$  at COMPASS shows a comparable behavior as observed in previous experiments. The data can be parameterized by almost equal parameters for the discussed physical models.

Based the reworked energy correction, a further software based improvement of the RPD energy resolution could be achieved. With an enhanced energy resolution a possible missing-mass measurement would be possible. This could be used as an additional requirement for the event selection.

An improvement of the Monte Carlo simulation for the RPD, especially in the problematic light-guide region, should be considered. Also an implementation of the efficiencies for the RPD slabs, would allow systematic studies. Therefore, a deeper investigation of the RPD acceptance should be considered.

The study of the  $|t|$ -acceptance, especially for  $|t|$  value larger then  $3 \text{ GeV}^2/c^2$ , could result in an improvement of the acceptance corrected  $|t|$ -spectrum and would allow further investigations of the distribution from theoretical side.

Based on the elastic scattering data an estimation of the luminosity for different reactions could be established. This could be used for a normalization from “number of events” into a differential cross-section.

Different elastic scattering processes could be investigated based on the knowledge obtained within this analysis. For example the elastic  $\pi^+ p$  or  $pp$ -scattering. The latter reaction could also be used for an investigation of the diffractive dip, which should be situated at a  $|t|$  around  $1.4 \text{ GeV}^2/c^2$  [36] and is not observed in the  $\pi^- p$  scattering due to the limited acceptance.

# Appendix A

## Calculations

### A.1 Analytic Solution for the Beam Energy

Full analytic calculation of the beam energy without approximation within the ultra-relativistic limit which is used in Eq (2.13).

$$\begin{aligned}
p_1 - p_3 &= p_2 + p_4 \\
(p_1 - p_3)^2 &= (p_2 + p_4)^2 \\
p_1^2 + p_3^2 - 2p_1p_3 &= p_2^2 + p_4^2 - 2p_2p_4 \\
m_1^2 + m_3^2 - 2(E_1E_3 - \vec{p}_1 \cdot \vec{p}_4) &= m_2^2 + m_4^2 - 2E_4m_2 \\
m_1^2 + m_3^2 - 2(E_1E_3 - |p_1||p_3|\cos\vartheta_3) &= m_2^2 + m_4^2 - 2E_4m_2 \\
m_1^2 + m_3^2 - 2(E_1E_3 - \sqrt{E_1^2 - m_1^2}|p_3|\cos\vartheta_3) &= m_2^2 + m_4^2 - 2(E_1 + m_2 - E_3)m_2 \\
E_1(E_3 - m_2) - \sqrt{E_1^2 - m_1^2}|p_3|\cos\vartheta_3 &= m_2(m_2 - E_3) - \frac{1}{2}(m_2^2 + m_4^2 - m_1^2 - m_3^2) \quad (\text{A.1})
\end{aligned}$$

The valid solution of this quadratic equation ends up in a sophisticated function for the beam energy.

$$E_1 = \frac{A + \sqrt{(C + D) \cdot (A^2 + 2B)^2}}{B} \quad (\text{A.2})$$

$$\begin{aligned}
A &= 4 \left[ E_3 (m_1^2 + m_4^2 + E_3 m_2 - m_3^2 - 3m_2^2) + m_2 (m_1^2 + m_2^2 + m_3^2 - m_4^2) \right] \\
B &= -8(E_3^2 - 2E_3m_2 + m_2^2 - p_3^2 \cdot \cos^2\vartheta_3) \\
C &= 4E_3 (m_1^2 m_2 + m_3^2 m_2 m_4^2 m_2) + 2 (m_1^2 m_4^2 + m_3^2 m_4^2 - m_1^2 m_3^2) \\
D &= 2m_2^2 [m_4^2 - m_1^2 - m_3^2 + 2E_3 m_2 - 2E_3^2] - 4m_1^2 p_3^2 \cos^2\vartheta_3
\end{aligned}$$



## Appendix B

### Additional RPD Information

#### B.1 Theoretical Prediction for Different Length of RPD Ring B Slabs

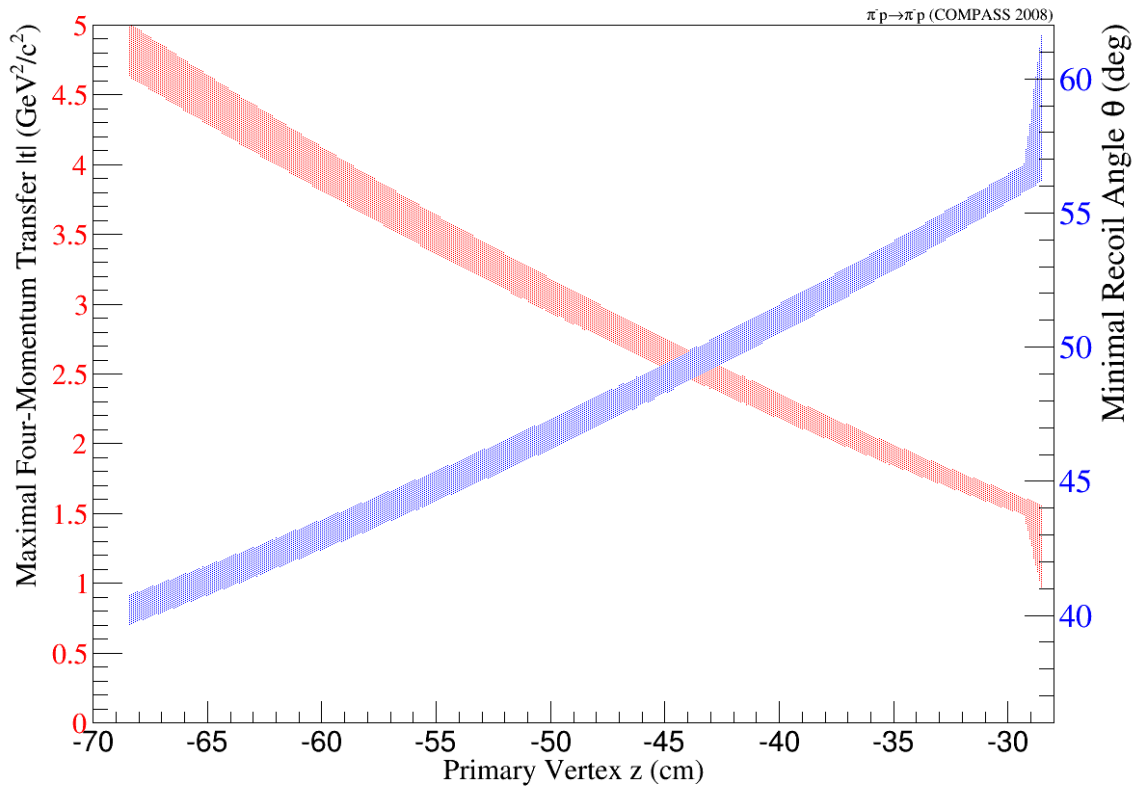


**Figure B.1:** Theoretical geometrical acceptance of the RPD. The length of the ring B slabs are assumed as 115 cm, which results in bend of the acceptance at  $z = -29$  cm due to the insufficient length of the ring A slabs. To fulfill the trigger requirement shown in Fig. 4.3a the length of ring A dominates the length of ring B at the end of the target region. This effect is superimposed by the resolution of the primary vertex  $z$ -position and therefore not visible in the real data.

## B.2 Light Guide Influence on Squared Four-Momentum Transfer $|t|$

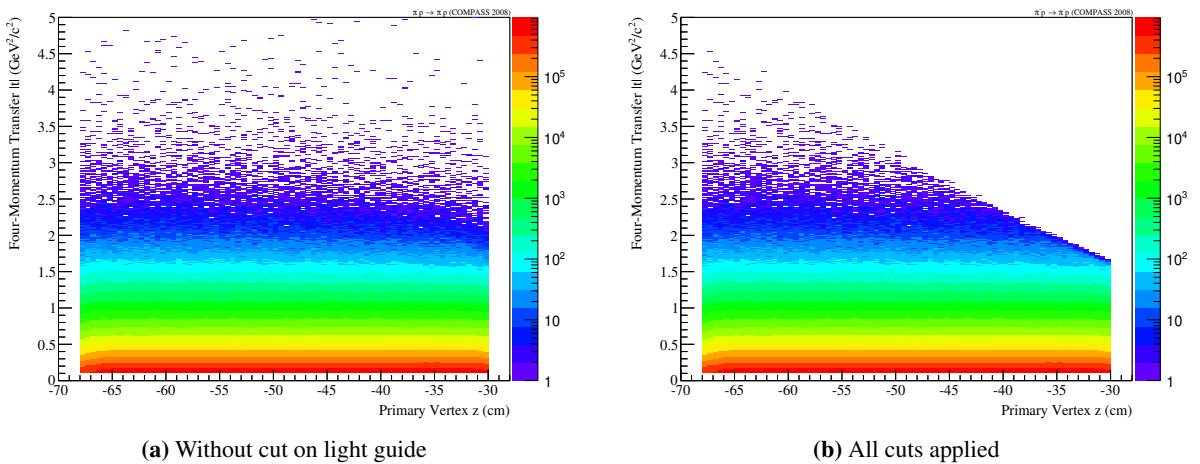


**Figure B.2:** In Figure B.2a the accepted events of the RPD without a cut on events situated in the area of the light guide based on the primary vertex  $z$  position and the squared four-momentum transfer  $|t|$  is shown. Due to the RPD light guide from each slab to the PMT of ring B which is molded from the same scintillating material as the slab, it has an influence on RPD trigger. Hits in this sector are also used as a trigger signal. An acceptance correction in this edge area is challenging. For simplicity reasons a cut is required which removes events with a hit in this region. This cut results in a sharp form of the accepted events by the RPD visible in Figure B.2b.

### B.3 Proton Energy Based on Passed Material Thickness

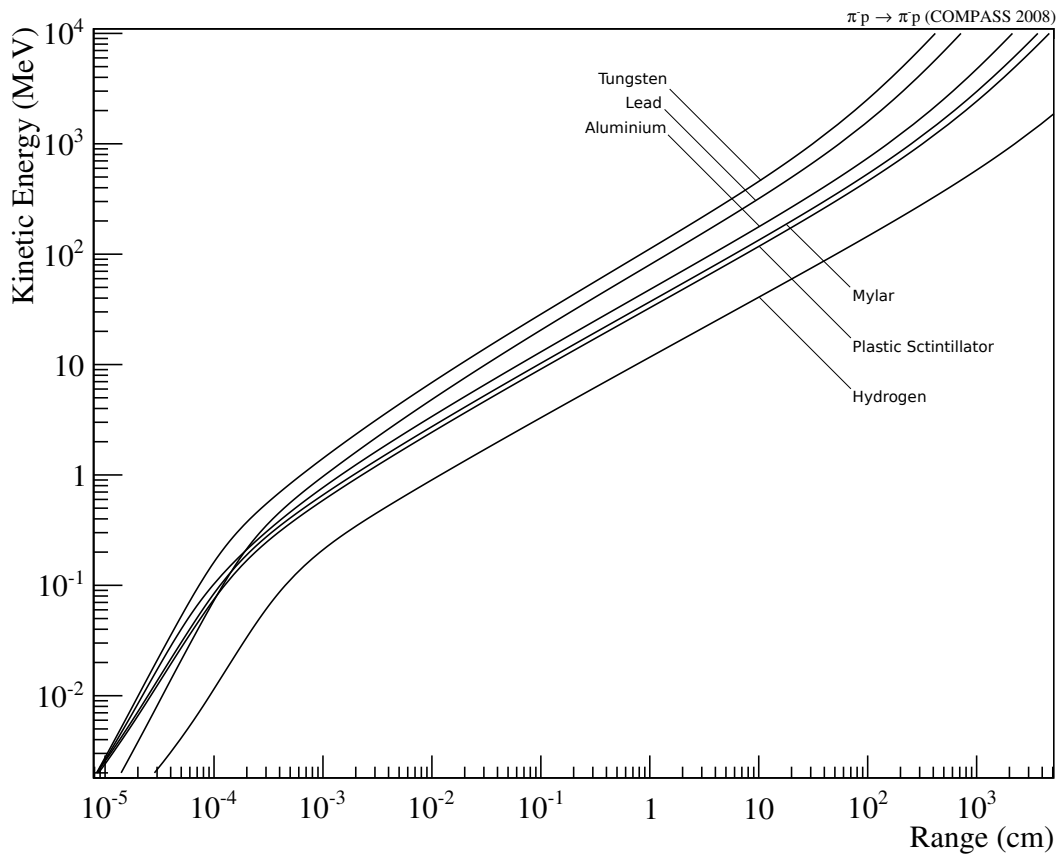


**Figure B.3:** Proton range distribution for the used materials in the RPD. The values are based on the NIST tabular [21]. For the energy correction a spline<sup>2</sup> fit is used to evaluate the energy loss or the range of protons in each material.

## B.4 Influence of Wrongly Identified Proton Tracks

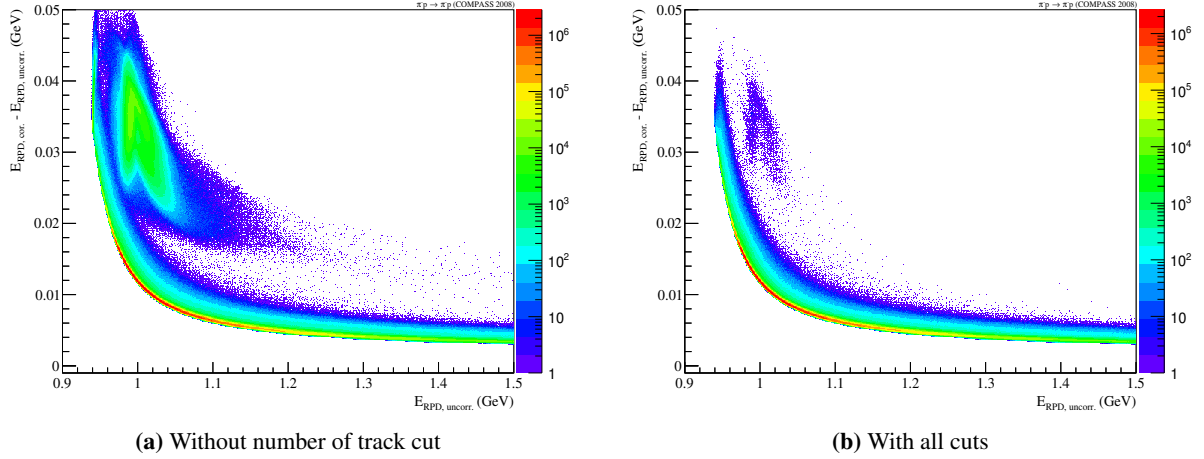


**Figure B.4:** The artifact which is situated in the region above the main slope is caused by wrong identified proton tracks by the RPD. Due to comparison between Figure B.4a which shows the effect of the improved energy correction without a cut on the number of proton tracks and Figure B.4b which shows the effect of the improved energy correction with all cuts, a clearer structure is visible. The origin of this structure is not clear at the moment.

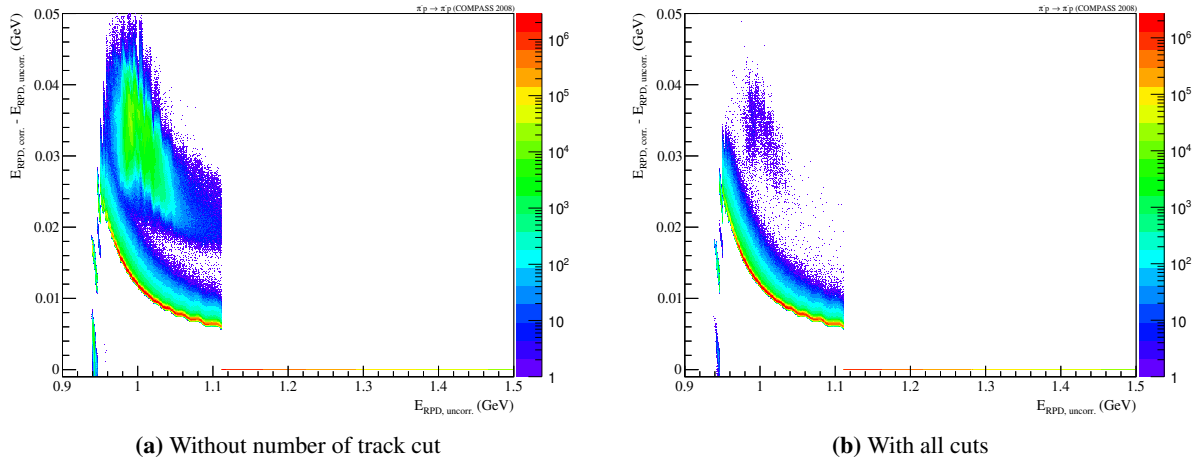


**Figure B.5:** The artifact which is situated in the region above the main slope is caused by wrong identified proton tracks by the RPD. Due to comparison between Figure B.5a which shows the effect of the improved energy correction without a cut on the number of proton tracks and Figure B.5b which shows the effect of the improved energy correction with all cuts, a clearer structure is visible. The origin of this structure is not clear at the moment.

# Appendix C

## Additional Analysis Informations

Additional figures and information about the kinematic distributions discussed in the analysis section of this thesis.

### C.1 Beam Gradient Projections

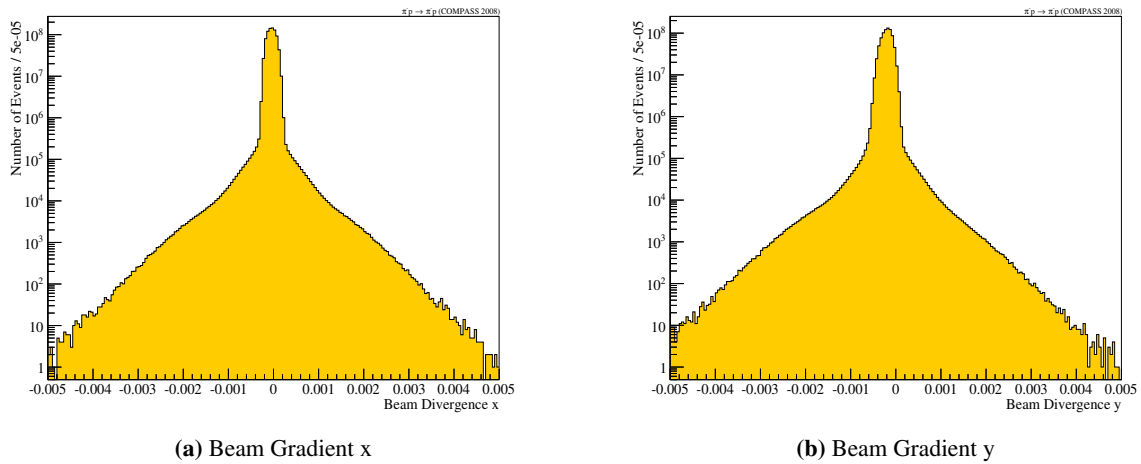


**Figure C.1:** Beam gradient in x and y projection after all cuts applied. The beam is well focused, but slightly tilted in y direction.

### C.2 Primary Vertex Projections

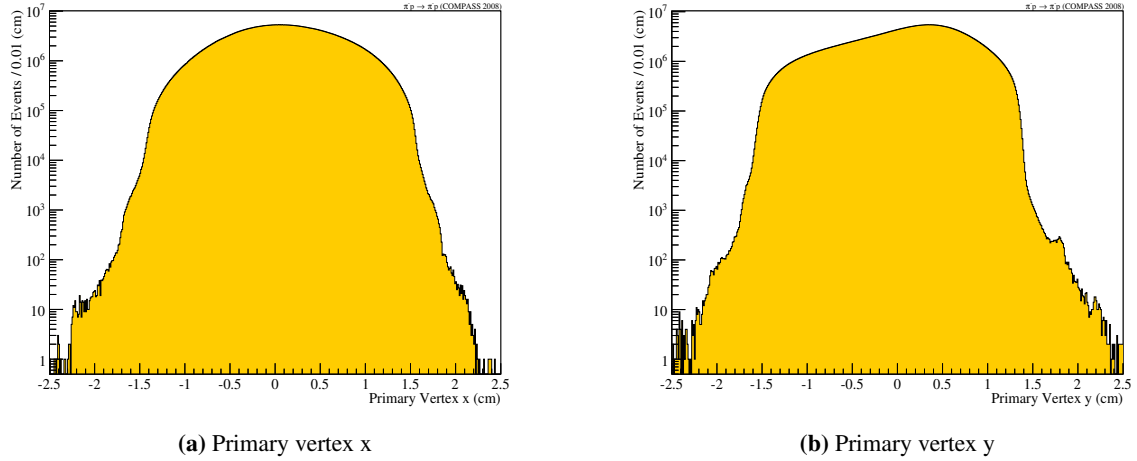


**Figure C.2:** Projection of the primary vertex  $x$ - and  $y$ -positions. The irregular form of the primary vertex  $y$ -position is in dependence with the shifted beam gradient in  $y$ -direction shown in Fig. C.1b.

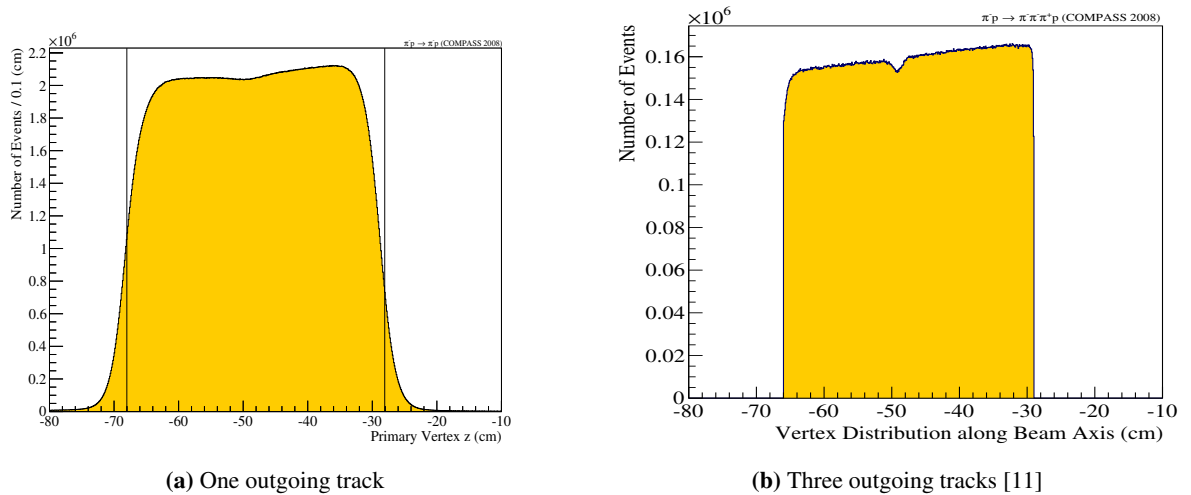


**Figure C.3:** Resolution effect due to the number of outgoing tracks on in the primary vertex  $z$ -distribution. The dip caused by the RPD laser connectors inside the slabs becomes much sharper.

# Appendix D

## Additional Information for the Conclusions

### D.1 Prediction with Nonacceptance Corrected Data

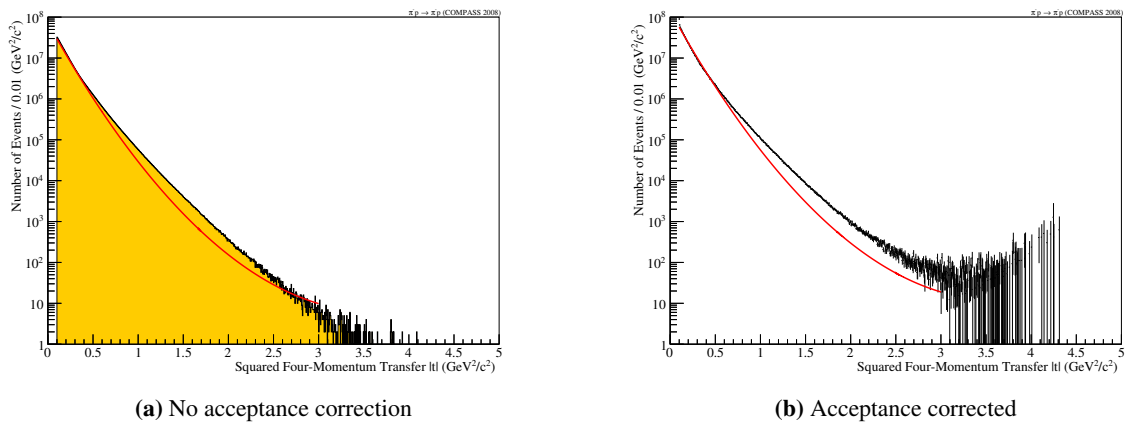


Figure D.1



# Own Contribution

This thesis was created at the chair of Prof. Stefan Paul at the Technische Universität München within the framework of the COMPASS experiment at CERN.

I started my thesis in November 2013 and was already familiar with the COMPASS experiment and especially the GEM detectors at this time, due to my previous bachelor thesis at the same chair in 2012. From this time on I participated in the development of PixelGEM detectors at E18 as a technical student.

Besides the obtained experience in detector physics and hardware, I also wanted to have an insight into data analysis and the software side of an experiment. Therefore, I chose the master thesis with the analysis of elastic scattering at COMPASS.

I started with a development of a simple event selection based on the so-called “UserEvent” of the software PHAST. By analyzing a single COMPASS run for the first time I got familiar with the software. Since my programming skills were just evolving at this time, it took some effort to achieve my very first results.

But with more challenging task like the development of an event generator for the elastic scattering process and a Monte Carlo software chain to produce simulated events, my software skills improved swiftly.

After several unsuccessful tries to use the 64bit versions of each analysis program, I finally succeeded in establishing an analysis software chain, which was capable to handle real and generated event data.

A well-knowing of the various software parts like the event generator, the Monte Carlo simulation of COMPASS, the analysis software CORAL and PHAST was necessary to start finally a sound investigation of the elastic scattering process and to understand the obtained results.

I needed an analysis framework to handle the various amount of data and resulting files. Hence, I developed my own framework for this purpose. However, it was not capable to handle the increasing requirements for data handling

Karl Bicker provided me his analysis toolkit ANTOK, which is developed by several people. After I got familiar with the structure of the program I could participate in the further development of this software. Working together on this tool with more experienced people was a great benefit for me.

The constantly urge to understand the obtained results of my analysis resulted mostly in finding unwanted artifacts in the distributions of variables. Especially my focus on the RPD and the detailed understanding its software took some time, but the result was the discovery of possible improvements like the energy correction.

Also the cooperative work with the theorist Vincent Mathieu was sophisticated, due to my still evolving theoretical knowledge. Nevertheless, it was a perfect opportunity to further extend my theoretical awareness.

The obtained experience and knowledge of the past year culminates in this thesis.



# Acknowledgements

First of all I would like to thank Prof. Stefan Paul, who gave me the possibility to work on a such interesting and versatile master thesis. The experience to apply and extend my obtained knowledge of the past five years of studying physics was very fulfilling.

My sincerest thanks to Florian Haas, who accurately identified my strengths and weaknesses. He was able to bring me back on the right track, when I got lost in the complexity of my topic. Florian always emphasized the importance of my work and motivated me whenever he could. I am immensely thankful for his knowledge and support.

Many thanks go to Boris Grube. He had always time for me and helped me with his advice and ideas. Boris provided me many insights into the COMPASS analysis and improved my work with his vast experience. It was a great benefit to me.

I gratefully acknowledge the help of Alexander Austregesilo, Karl Bicker, Stefan Huber and Sebastian Uhl. All of them were eager to assist me whenever I got stuck. Without them I would not have obtained such a detailed knowledge in COMPASS analysis. Thank you very much!

My sincerest thanks go to Vincent Mathieu, who explained me the complex theory of Regge from the theorist side of view. It was very helpful.

Special thanks go to Sverre Dorheim. Discussing results and working with him in the lab was always inspiring.

I also want to thank Julia Bloemer, Andreas Hönle, Johannes Rauch Stephan Schmeing and Stephan Wallner who shared the office with me, for the great fun we had together.

Also thanks go out to everybody at E18 and COMPASS. Being part of a group with great knowledge and interesting research areas was very nice.

I am very grateful for the support of my all friends. They encouraged me all the time and endured my varying moods. Thanks a lot!



# Bibliography

- [1] H. Geiger, “The Scattering of the  $\alpha$ -Particles by Matter”, *Royal Society of London Proceedings Series A* 83 (Apr. 1910) 492–504.
- [2] E. Rutherford, “The Scattering of  $\alpha$  and  $\beta$  Particles by Matter and the Structure of the Atom”, *Philosophical Magazine* 21 (1911) 669–688.
- [3] N. Bohr, “On the Constitution of Atoms and Molecules”, *Philosophical Magazine* 26 (1913) 476–502.
- [4] E. Rutherford, “Collision of  $\alpha$  Particle with Light Atoms. IV. An Anomalous Effect in Nitrogen.”, *Philosophical Magazine* 37 (1919) 581–587.
- [5] J. Chadwick, “The Existence of a Neutron”, *Royal Society of London Proceedings Series A* 830 (May 1932) 692–708.
- [6] “Tentativo di una Teoria Dei Raggi  $\beta$ ”, *Il Nuovo Cimento* 11 (1934) 1–19.
- [7] W. Pauli, *Letter of Wolfgang Pauli*, 1930, URL: <http://microboone-docdb.fnal.gov/cgi-bin/RetrieveFile?docid=953;filename=pauli%20letter1930.pdf>.
- [8] C. Lattes et al., “Processes involving charged Mesons”, *Nature* 159 (1947) 694–697, doi: 10.1038/159694a0.
- [9] M. Gell-Mann, “A schematic Model of Baryons and Mesons”, *Physics Letter* 8 (1964) 214–215.
- [10] G. Zweig, “An SU3 Model for strong Interaction Symmetry and its Breaking”, *CERN Libraries 8182/TH-401* (1964).
- [11] F. Haas, “Two-Dimensional Partial-Wave Analysis of Exclusive 190 GeV  $\pi^-$  p Scattering into the  $\pi^- \pi^- \pi^+$  Final State at COMPASS (CERN)”, PhD thesis, Technische Universität München, 2014.
- [12] C. B. et al., “High-Energy Pion-Proton elastic Scattering and the Pion Form Factor”, *Phys. Rev. Lett.* 132B (1983) 191–194.
- [13] T. Regge, “Introduction to complex orbital momenta”, *Il Nuovo Cimento Series 10* Volume 14, Issue 5 (1959) 951–976.
- [14] P. L. Sandy Donnachie Günter Dosch and O. Nachtmann, *Pomeron Physics and QCD*, Cambridge University Press, 2002, ISBN: 0-521-67570-7.
- [15] V. Mathieu, “Regge Amplitudes for Two-to-Two Reactions”, *Proceedings of Science* (2013).
- [16] E. P. V. Barone, *High-Energy Particle Diffraction*, Springer, 2010, ISBN: 978-3-642-07567-4.
- [17] reproduced with permission from *Pomeron Physics and QCD* by Sandy Donnachie, Guenter Dosch, Peter Landshoff and Otto Nachtmann (Cambridge University Press, 2002), URL: <http://www.damtp.cam.ac.uk/user/pvl/QCD/>.
- [18] P. Abbon et al., “The COMPASS Setup for Physics with Hadron Beams” (2014), arXiv: 1410.1797 [physics.ins-det].

- [19] R. Brun, *ROOT - A Data Analysis Framework*, URL: <http://root.cern.ch/>.
- [20] D. Alde et al., “The slow proton position-sensitive time of flight detector of the GAMS NA12/2 experiment at CERN”,  
*Nucl. Instrum. Methods Phys. Res., A* 342.LAPP-EXP-93-10 (1993) 389–397. 16 p.
- [21] M. Berger et al., *Stopping-Power and Range Tables for Electrons, Protons, and Helium Ions*, 2011, URL: <http://www.nist.gov/pml/data/star/index.cfm>.
- [22] K. Judd, *Numerical Methods in Economics*, p. 225, MIT press, 1998, ISBN: 978-0-262-10071-7.
- [23] K. Bicker, *private communications*, 2014.
- [24] "CERN", *GEANT - Detector description and simulation tool*, CERN Program Library Long Writeup W5013, 1993,  
URL: [http://wwwasdoc.web.cern.ch/wwwasdoc/geant\\_html3/geantall.html](http://wwwasdoc.web.cern.ch/wwwasdoc/geant_html3/geantall.html).
- [25] K. Bicker, *Yet Another Beamfile for COMPASS*, Analysis Meeting, 2013,  
URL: [http://wwwcompass.cern.ch/compass/software/analysis/transparencies/2013/am\\_130711/bicker\\_Yet-Another-Beamfile-for-COMPASS\\_2013-07-11.pdf](http://wwwcompass.cern.ch/compass/software/analysis/transparencies/2013/am_130711/bicker_Yet-Another-Beamfile-for-COMPASS_2013-07-11.pdf).
- [26] J. Beringer et al., “Review of Particle Physics”, *Phys. Rev. D* 86 (2012) 010001.
- [27] V. Mathieu, *private communications*, Indiana University Research Fellow, 2014.
- [28] C. et al., *Physical Review D* 17 (1978) 1693, 1978.
- [29] S. et al., *Physics Letter B* 146 (1984) 116, 1984.
- [30] AKERLOF 1976 *PR D* 14, 2864, 1976.
- [31] AYRES 1977 *PR D* 15, 3105, 1977.
- [32] C. N. Y. T. Chou, “Model of Elastic High-Energy Scattering”,  
*Physical Review* Volume 170, Number 5 (1968) 1591–1596.
- [33] W. B. et al., *Phys. Rev. Lett.* 47 (1981) 1683.
- [34] J. Orear, *Prococeedings, 17th Rencontre de Moriond* 2 (1982) 359.
- [35] R. K. et al., *Preprint Fermilab-Pub-83/20-EXP* (1983).
- [36] C. N. Y. T. Chou,  
“Elastic hadron-hadron scattering at ultrahigh energies and existence of many dips”,  
*Physical Review D* Volume 19, Number 11 (1979) 3268–3272.

# List of Figures

1.1	Pomeron exchange between pion and proton . . . . .	9
1.2	Pomeron and Regge trajectories with their total cross-sections . . . . .	10
1.3	$\pi^-p$ scattering at data $200 \text{ GeV } c^{-1}$ . . . . .	10
2.1	General scattering process . . . . .	13
2.2	Elastic scattering process . . . . .	15
2.3	Definition of Fraunhofer's diffraction . . . . .	18
2.4	Single and double Pomeron contributions . . . . .	24
3.1	COMPASS layout for 2008 . . . . .	28
3.2	Target region for COMPASS 2008 layout . . . . .	29
3.3	Sketch of the DT0 . . . . .	29
4.1	Sketch with dimension and coordinates of the RPD . . . . .	32
4.2	Energy loss correlation between RPD rings of the recoiled proton . . . . .	32
4.3	Trigger scheme and coplanarity for RPD . . . . .	33
4.4	RPD hitmaps for ring A and ring B . . . . .	34
4.5	Geometrical acceptance of the RPD . . . . .	35
4.6	Uncorrected energy of the RPD compared with corrected energy . . . . .	36
4.7	Energy correction effect for RPD proton . . . . .	36
4.8	Proton range distribution . . . . .	37
4.9	RPD energy resolution . . . . .	38
4.10	Spectrometer and RPD energy comparison . . . . .	38
5.1	Applied cuts and their effect . . . . .	42
5.2	Beam properties . . . . .	42
5.3	Beam energy . . . . .	43
5.4	RPD ring B light guide cut . . . . .	44
5.5	Vertex distributions . . . . .	45
5.6	Momenta of scattered pion . . . . .	45
5.7	Scattering angles of the pion . . . . .	46
5.8	Uncorrected squared four-momentum $ t $ . . . . .	47
5.9	Overview of run numbers and events . . . . .	47
6.1	RPD hitmap comparison between simulation and real data . . . . .	51
7.1	Acceptance of the primary vertex $x $ . . . . .	54
7.2	Acceptance of the primary vertex $x $ . . . . .	54
7.3	Acceptance of primary vertex $z$ . . . . .	55
7.4	Acceptance of the squared four-momentum transfer $ t $ . . . . .	56
7.5	Resolutions of vertex $x$ - and $y$ -position . . . . .	57

7.7	Resolutions of scattered momenta in $x$ - and $y$ -direction . . . . .	57
7.6	Resolution of vertex $z$ -position . . . . .	58
7.8	Resolution of scattered momentum in $z$ -direction . . . . .	58
7.9	Resolution squared four-momentum transfer $ t $ . . . . .	59
8.1	Single exponential fit function for squared four-momentum transfer $ t $ . . . . .	64
8.2	Single exponential slope behavior . . . . .	65
8.3	Double exponential fit function for squared four-momentum transfer $ t $ . . . . .	66
8.4	Three-pion squared four-momentum transfer $ t $ fit. . . . .	67
8.5	Triple exponential fit function for squared four-momentum transfer $ t $ . . . . .	68
8.6	Pion and proton form factors . . . . .	69
8.7	Description based on Donnachie et al. . . . .	70
8.8	Quadratic term in single Pomeron trajectory . . . . .	71
8.9	Prediction based on a squared term in Pomeron trajectory . . . . .	72
8.10	Parametrization based on the Chou-Yang relation . . . . .	74
B.1	Theoretical geometrical acceptance of the RPD with 115 cm slabs of ring B . . . . .	81
B.2	Influence of RPD light guide cut . . . . .	82
B.3	Proton range distribution . . . . .	83
B.4	Influence of number of proton tracks cut on RPD improved energy correction . . . . .	84
B.5	Influence of number of proton tracks cut on RPD present energy correction . . . . .	84
C.1	Beam gradient projections . . . . .	85
C.2	Primary vertex projections . . . . .	86
C.3	Primary vertex $z$ for different number of outgoing tracks . . . . .	86
D.1	Influence of acceptance correction and theory . . . . .	87

# List of Tables

3.1	Main components of negative pion beam . . . . .	27
8.1	Fit results from single exponential fit . . . . .	64
8.2	Fit results from double exponential fit . . . . .	66
8.3	Fit results from triple exponential fit . . . . .	67
8.4	Fit results from Donnachie et al. description . . . . .	70
8.5	Fit results from quadratic Pomeron trajectory . . . . .	72
8.6	Fit results from Chou-Yang model assumption . . . . .	74